From Geometry Optimization to Time Dependent Molecular Structure Modeling: Method Developments, *ab initio* Theories and Applications

Wenkel Liang

A dissertation
submitted in partial fulfillment of the
requirements for the degree of

Doctor of Philosophy

University of Washington

2012

Reading Committee:

Xiaosong Li, Chair

David J. Masiello

Lutz Maibaum

Program Authorized to Offer Degree:
Chemistry

University of Washington

Abstract

From Geometry Optimization to Time Dependent Molecular Structure Modeling: Method Developments, *ab initio* Theories and Applications

Wenkel Liang

Chair of the Supervisory Committee:
Associate Professor Xiaosong Li
Department of Chemistry

This dissertation consists of two general parts: I. developments of optimization algorithms (both nuclear and electronic degrees of freedom) for time-independent molecules and II. novel methods, first-principle theories and applications in time dependent molecular structure modeling. In the first part, we discuss in specific two new algorithms for static geometry optimization, the eigenspace update (ESU) method in nonredundant internal coordinate that exhibits an enhanced performace with up to a factor of 3 savings in computational cost for large-sized molecular systems; the Car-Parrinello density matrix search (CP-DMS) method that enables direct minimization of the SCF energy as an effective alternative to conventional diagonalization approach. For the second part, we consider the time dependence and first presents two nonadiabatic dynamic studies that model laser controlled molecular photo-dissociation for qualitative understandings of intense laser-molecule interaction, using *ab initio* direct Ehrenfest dynamics scheme implemented with real-time time-dependent density functional theory (RT-TDDFT) approach developed in our group. Furthermore, we place our special interest on the nonadiabatic electronic dynamics in the ultrafast time scale, and presents 1) a novel technique that can not only obtain energies but also the

electron densities of doubly excited states within a single determinant framework, by combining methods of CP-DMS with RT-TDDFT; 2) a solvated first-principles electronic dynamics method by incorporating the polarizable continuum solvation model (PCM) to RT-TDDFT, which is found to be very effective in describing the dynamical solvation effect in the charge transfer process and yields a consistent absorption spectrum in comparison to the conventional linear response results in solution. 3) applications of the PCM-RT-TDDFT method to study the intramolecular charge-transfer (CT) dynamics in a C_{60} derivative. Such work provides insights into the characteristics of ultrafast dynamics in photoexcited fullerene derivatives, and aids in the rational design for pre-dissociative exciton in the intramolecular CT process in organic solar cells.

TABLE OF CONTENTS

LIST OF FIGURES

LIST OF TABLES

GLOSSARY

ADMP: Atom-centered Density Matrix Propagation

AM1: Austin Model 1

AO: Atomic Orbital

ASC: Apparent Surface Charge

B3LYP: Becke, 3-parameter, Lee-Yang-Parr

BHJ: Bulk Heterojunctions

BO: Born-Oppenheimer

CASSCF: Complete Active Space Self-Consistent Field

CI: Configuration Interaction

CIS: Configuration Interaction Singles

CP-DMS: Car-Parrinello Density Matrix Search

CSC: Continuous Surface Charge

CT: Charge-Transfer

DIIS: Direct Inversion in the Iterative Subspace

DMA: DiMethyl Aniline

DOS: density of states

ESU: EigenSpace Update

FMM: Fast Multipole Method

HOMO: Highest Occupied Molecular Orbital

LNV: Li-Nunes-Vanderbilt

LUMO: Lowest Unoccupied Molecular Orbital

MCH: MethyCyclohexane

MD: Molecular Dynamics

MM: Molecular Mechanics

MMUT: Modified Midpoint and Unitary Transformation

MO: Molecular Orbital

PBE: Perdew-Burke-Ernzerhof

PCM: Polarizable Continuum Model

PES: Potential Energy Surface

PNA: para-nitroaniline

QM: Quantum Mechanics

QN-DMS: Quasi-Newton Density Matrix Search

RFO: Rational Function Optimization

RMS: Root-Mean-Square

RT-TDDFT: real-time TDDFT

SAC-CI: Symmetry Adapted Cluster CI

SCF: Self-Consistent Field

SCRF: Self-Consistent Reaction Field

SVD: Single Value Decomposition

TDDFT: Time-Dependent Density Functional Theory

TDHF: Time-Dependent Hartree-Fock

TDKS: Time-Dependent Kohn-Sham

TDSCF: Time-Dependent Self-Consistent Field

TDSE: Time-Dependent Schrodinger Equation

TRM: Trust Radius Model

ACKNOWLEDGMENTS

I would like to thank all the Li group members (past and present) who have given me support throughout my graduate school years.

In particular, Xiaosong, my always supportive brilliant advisor and passionate pursuer for physical chemistry science.

Christine, my old colleague who guided me on the way and stands as the best example of academic grad student.

Katia, my other old colleague who offered a handful of advices and also sets as a versatile life example.

Feizhi, my constant lunch partner who offered insightful discussions with me on various topics not merely limited to science.

Joseph, my usual officemate and conference roomate who has been very helpful all the time especially on organizing theory events including my defense celebration.

Other computational and theoretical physical chemists: Craig, Bo, Yong, CMoss, Sean, David, Lutz and many others.

Also special thanks to my dear lovely wife Jia and my parents, god mother Wenli, aunt Michelle, for their constant support on my PhD endeavor, although it is not practically the well-paid "doctor".

DEDICATION

To my adorable wife, *Jia*.
Also to my dear parents, god mother *Wenli*, aunt *Michelle*.
Mian power!

Chapter 1
INTRODUCTION

The following document collects major achievements of my research while working towards my doctorate degree. My work at the University of Washington has covered many topics in the realm of computational physical chemistry, which involves primarily:

- Development of efficient parallel optimization methodology and algorithm for large-scale molecular geometry and electronic structure in quantum chemistry. [1–4]

- Development of novel theory and methodology for *ab initio* electronic dynamics and linear response theory.[5–8]

- Modeling and simulating molecular systems, from linear/non-linear optical properties, to reaction energetics, and to time-dependent laser controlled photochemistry. [9–14]

- Solvation effect with polarizable continuum model (PCM) methods and solvation shell response. [15, 16]

This introductory chapter provides a brief overview of the fields of geometry optimization for molecule and time-dependent molecular structure modeling. My development of novel methods and interesting applications are also highlighted. Chapter 2

introduces an efficient eigenspace update geometry optimization method in nonredundant internal coordinate. Chapter 3 presents a novel Car-Parrinello density matrix search (CP-DMS) method for direct minimization of the SCF energy as an effective alternative to conventional diagonalization approach. Chapter 4 describes the theory of *ab initio* direct Ehrenfest dynamics implemented with real-time time-dependent density functional theories (RT-TDDFT) approach, and discusses two studies using this method that model laser controlled photo-dissociation. Chapter 5 presents a novel technique that combines the CP-DMS method with RT-TDDFT to explore doubly excited states within a single determinant framework. Chapter 6, extends RT-TDDFT with solvation effect using polarizable continuum model (PCM) to give an effective first-principles solvated electronic dynamics approach. Finally, in Chapter 7, I apply the PCM-RT-TDDFT to study some dynamical aspects of excited state electron-hole separation in a fullerine derivative complex (C_{60}:DMA).

A brief appendix is included at the end of this thesis, in which I work through some of the details and derivations of the traditional Ehrenfest molecular dynamics approach.

1.1 Geometry Optimization for Stationary Molecule

Starting from the non-relativistic time-independent Schrödinger equation

$$\hat{H}\Psi(\mathbf{R},\mathbf{r}) = E\Psi(\mathbf{R},\mathbf{r}) \tag{1.1}$$

where $\mathbf{R}$ refers to nuclear positions and $\mathbf{r}$ electronic coordinates. The standard Hamiltonian contains kinetic and potential energy operators for all particles

$$\begin{aligned}\hat{H} &= \hat{T}_n + \hat{T}_e + \hat{V}_{ne} + \hat{V}_{ee} + \hat{V}_{nn} \\ &= -\sum_I \frac{\hbar^2}{2M_I}\nabla_I^2 - \sum_i \frac{\hbar^2}{2m_e}\nabla_i^2 + \sum_{i<j} \frac{e^2}{|\mathbf{r}_i - \mathbf{r}_j|} \\ &- \sum_{i,I} \frac{e^2 Z_I}{|\mathbf{r}_i - \mathbf{R}_I|} + \sum_{I<J} \frac{e^2 Z_I Z_J}{|\mathbf{R}_I - \mathbf{R}_J|}\end{aligned} \tag{1.2}$$

Because electrons are much ligher than nuclei, they have much faster motion than nuclei. One can approximately separate the electrons from nuclei. Such separation is well-known as the *Born-Oppenheimer* (BO) approximation. Under the BO approximation, the electronic wave function depends parametrically on the nuclear coordinates. On the other hand nuclei move on potential energy surfaces (PES) that are solutions to the electronic Schrödinger equation, which can be expressed as follows

$$\begin{aligned}\Psi(\mathbf{R},\mathbf{r}) &= \Psi_n(\mathbf{R})\Psi_e(\mathbf{R},\mathbf{r}) \\ \hat{H}_e &= \hat{T}_e + \hat{V}_{ne} + \hat{V}_{ee} + \hat{V}_{nn} \\ \hat{H}_e\Psi_e(\mathbf{R},\mathbf{r}) &= E_e(\mathbf{R})\Psi_e(\mathbf{R},\mathbf{r}) \\ (\hat{T}_n + E_e(\mathbf{R}))\Psi_n(\mathbf{R}) &= E_{tot}\Psi_n(\mathbf{R})\end{aligned} \tag{1.3}$$

Therefore, the nuclear and electron wave function can be optimized separately within the BO framework.

1.1.1 Nuclear Geometry Optimization

Nuclei of atoms are *de facto* heavy enough for quantum effects to be neglected, and therefore nuclei are often treated as classical particles. With the classical description, optimization of nuclear geometry of a molecule is equivalent to the search of the

minimum energy structure, or mathematically defined as:

$$\frac{\partial E_{tot}}{\partial \mathbf{R}} = 0, \quad \frac{\partial^2 E_{tot}}{\partial \mathbf{R}^2} > 0 \tag{1.4}$$

Quasi-Newton Approach The most widely used geometry optimization method is the so-called quasi-Newton approach, in which analytical first derivatives and approximate second derivatives are used to search for a lower energy point on the PES. In this method, a Newton-Raphson step, Δx, is taken on a local quadratic PES

$$\Delta \mathbf{x} = -\mathbf{H}^{-1}\mathbf{g} \tag{1.5}$$

where $\mathbf{g}$ is the gradient (first derivative) and $\mathbf{H}$ is the Hessian (second derivative). In practical implementations, the Newton-Raphson step is stabilized with a control technique such as the rational function optimization (RFO)[17, 18] and the trust radius model (TRM).[19–22] A numerical Hessian update scheme, such as BFGS,[23, 24] SR1,[25] and PSB,[20, 26] is employed to relace computationally expensive analytical evaluations of the second derivatives. To obtain an optimization step Δx, eq 1.5 can be solved with a direct inversion of the Hessian or RFO/TRM in the eigenvector space of the Hessian. However, inversion or diagonalization of a Hessian matrix incurs an $O(N^3)$ scaling, where N is the number of nuclear degrees of freedom. Such a cubic scaling can become a substantial bottleneck in the optimization of large molecules with semiempirical or linear scaling electronic structure methods. Alternatively, an iterative $O(N^2)$ approach can be carried out to search for the RFO solution in the reciprocal space of the Hessian.[27] However, iterative solutions are often subjected to numerical instabilities and a large scaling prefactor. In addition, such iterative approach does not offer direct computation of eigenvectors and eigenvalues that are important in vibrational analysis and transition state optimizations.

Internal Coordinate v.s. Cartesian Coordinate The choice of coordinate system is crucial for successful convergence of the geometry optimization algorithm. In most cases, geometry optimization in an appropriate set of internal coordinates can converge significantly faster than in standard Cartesian coordinates.[28–30] For example, bond distance, bond angle and dihedral angle are better representations than the traditional Cartesian coordinates for a molecular system with rich chemical information. However, a practical internal coordinate system for molecular geometry optimizations often contains redundancy. For large-scale systems, coordinate redundancy can become the speed-limiting factor arising from operating on excessively large matrices. In principle, redundancy can be removed by transformation to the nonredundant internal coordinate, leading to a much smaller coordinate space and less computationally expensive matrix inversion. However, obtaining the redundant-nonredundant vectors is another O(N^3) procedure where N is the number of nonredundant coordinates. This dilemma largely prevents a practical application of geometry optimization in nonredundant coordinate space.

A novel eigenspace update for large scale system method in nonredundant internal coordinate is introduced in Chapter 2 for geometry optimization of large scale system with enhanced overall performance.

1.1.2 Electronic Structure Optimization

Having a fixed nuclear geometry, the stationary electronic wave function can be obtained following variational principle and by minimizing total electronic energy with respect to internal variables such as spin orbitals or electron density. In practice, stable electronic wave function is usually solved iteratively using self-consistent-field (SCF) procedures. A number of linear scaling SCF methods have been developed to optimize wave functions for large-scale molecules within the single Slater determi-

nant/configuration framework, using Hartree-Fock (HF) and density functional theory (DFT) methods. At the large molecule limit, the most computationally expensive step was previously the evaluation of two-electron integrals and forming the Fock/Kohn-Sham matrix that formally scales as O(N^4). This step has been improved to almost linear scaling by means of the fast multipole method (FMM)[31, 32] and linear scaling exchange.[33–35]

In addition, with density matrix search (DMS) methods and sparse matrix manipulations, [36] the O(N^3) scaling diagonalization step for solving the Roothaan-Hall SCF equation can be avoided. The DMS methods, exemplified by the conjugate-gradient[37] and quasi-Newton (QN-)[36] DMS algorithms, offer an alternative to diagonalization through direct minimization of the energy with respect to the density matrix. With these advances, SCF based first principles methods have achieved linear scaling in the large molecule limit. Conceptually similar to the DMS method, the Car-Parrinello (CP)[38] and atom-centered density matrix propagation (ADMP)[39] approaches minimize the electronic energy along a dynamical force, treating electron density motion with a classical equation of motion and a properly tuned fictitious mass.[40–42]

In spite of the success in molecular dynamics, the advantage of being first order propagation methods, CP or ADMP based methods have not been quite successful in SCF wave function optimization due to slow convergence. Chapter 3 presents a novel Car-Parrinello density matrix search (CP-DMS) method to directly minimize the SCF energy as an effective alternative to diagonalization.

1.2 Time Dependent Electronic Structure

The non-relativistic time-dependent Schrödinger equation (TDSE) governs the general behavior of a quantum molecular system in both time and space

$$i\hbar\frac{\partial}{\partial t}\Psi(\mathbf{R},\mathbf{r};t) = \hat{H}\Psi(\mathbf{R},\mathbf{r};t) \tag{1.6}$$

If the Hamiltonian remains time-independent and contains the same set of operators as in eq 1.2, to approximately solve the TDSE nuclear and electronic degrees of freedom can be separated in a similar BO spirit. For example, the total wavefunction can be written in the form of a product ansatz with a phase factor[43]

$$\Psi(\mathbf{R},\mathbf{r};t) \approx \Psi_n(\mathbf{R},t)\Psi_e(\mathbf{r},t)exp\left[\frac{i}{\hbar}\int_{t_0}^{t} dt'\tilde{E}_e(t')\right] \tag{1.7}$$

where the nuclear and electronic wavefunctions are separately normalized to unity at every instant of time, and the phase factor is chosen as

$$\tilde{E}_e(t) = \langle\Psi_n(\mathbf{R},t)\Psi_e(\mathbf{r},t)|\,\hat{H}_e\,|\Psi_n(\mathbf{R},t)\Psi_e(\mathbf{r},t)\rangle \tag{1.8}$$

1.2.1 Ehrenfest Molecular Dynamics

By substituting the product ansatz in eq 1.7 into eq 1.6, and extracting the classical mechanics within the classical limit $\hbar \to 0$ for the nuclear wavefunction, one can obtain a coupled set of differential equations as (see Appendix A for detailed derivations)

$$\begin{aligned} M_I\ddot{\mathbf{R}}_I(t) &= -\nabla_I\,\langle\Psi_e|\,\hat{H}_e\,(\mathbf{r},\mathbf{R}_I(t))\,|\Psi_e\rangle \\ i\hbar\frac{\partial\Psi_e}{\partial t} &= \hat{H}_e\,(\mathbf{r},\mathbf{R}(t))\,\Psi_e \end{aligned} \tag{1.9}$$

Thereby, the nuclei are propagated by classical Newton's equation and the potential energy surface (PES) is constructed by solving the time-dependent electronic

Schrödinger equation "on-the-fly". Such approach is often referred to as the "Ehrenfest molecular dynamics", and it has been shown to include rigoriously nonadiabatic transitions between different electronic states within the framework of classical nuclear motion and the mean-field (TDSCF) approximation to the electronic structure.

With the electronic wavefunction represented by a single Slater determinant of one-electron molecular orbitals (MOs) ϕ_i, the time-dependent Schrödinger equation reduces to the time-dependen Hartree-Fock (TDHF) equation, or the time-dependent Kohn-Sham (TDKS) equation,

$$i\hbar\frac{\partial\phi_i}{\partial t} = \hat{K}(t)\phi_i \tag{1.10}$$

the MOs are represented as a linear combination of atomic orbital (AO) basis functions χ_μ as

$$\phi_i(t) = \sum_\mu c_{\mu,i}(t)\chi_\mu \tag{1.11}$$

where the time-dependent coefficients are complex numbers. The field-free Hamiltonian describes the molecular electronic system at a given time,

$$\hat{K}_0(t) = \hat{h}(t) + \hat{G}(t) \tag{1.12}$$

The one-electron operator $\hat{h}(t)$ (in atomic units $\hbar = m_e = e = 1$) includes the electron-nuclear attractive potential and electron kinetic energy operator,

$$\hat{h}(t) = -\sum_i \frac{1}{2}\nabla_i^2 - \sum_{i,I}\frac{Z_I}{|\mathbf{r}_i - \mathbf{R}_I|} \tag{1.13}$$

If the nuclei degrees of freedom are frozen, the one-electron operator becomes time-independent constant as $\hat{h}(t) = \hat{h}(t_0)$. The two-electron operator $\hat{G}[\rho(t)]$ gives the electron-electron interactive potential, and it is implicitly time-dependent because it depends on the instantaneous electron distribution at a give time. In the adiabtic

KS-DFT formalism, $\hat{G}[\rho(t)]$ includes the electron-electron Coulomb and exchange-correlation potentials

$$\hat{G}(t) = \int \frac{\rho(\mathbf{r}', t)}{|\mathbf{r} - \mathbf{r}'|} d\mathbf{r}' + V_{xc}[\rho](\mathbf{r}, t) \approx \int \frac{\rho(\mathbf{r}', t)}{|\mathbf{r} - \mathbf{r}'|} d\mathbf{r}' + V_{xc}[\rho_t](\mathbf{r}) \tag{1.14}$$

Because the exact form of $V_{xc}[\rho](\mathbf{r}, t)$ is unknown for general system, the adiabatic approximation is made within DFT that the exchange-correlation potential V_{xc} only depends on the instantaneous time-dependent density $\rho(\mathbf{r}, t)$ at a given time: $V_{xc}[\rho](\mathbf{r}, t) \approx V_{xc}[\rho_t](\mathbf{r})$

After some simple algebra, the TDHF/TDDFT equation of eq 1.10 can also be represented in the form of a single-particle Liouville equation in terms of the density

$$i\hbar \frac{\partial \rho}{\partial t} = \hat{K}\rho - \rho\hat{K} = \left[\hat{K}, \rho\right] \tag{1.15}$$

where ρ is the one-body density matrix in the MO basis

$$\rho(\mathbf{r}, \mathbf{r}', t) = \sum_i \phi_i(\mathbf{r}, t)\phi_i^*(\mathbf{r}', t) \tag{1.16}$$

Based on the matrix representation of the above Liouville equation, Chapter 4 presents two nonadiabatic dynamic studies that model laser controlled molecular photo-dissociation, using *ab initio* direct Ehrenfest dynamics scheme implemented with real-time time-dependent DFT (RT-TDDFT) approach.

1.2.2 Nonadiabatic Electronic Dynamics

In the ultrafast time scale where the nuclear degrees of freedom are mostly inactive, electronic dynamics proves to be quite useful in describing reactions in the strongly coherent regime and some nonadiabatic phenomenon. In this dissertation, several interesting applications will be discussed.

Doubly Excited State Resonant excitation within real-time TDHF and TDDFT gives rise to mixing with doubly excited reference states, yielding excitation energies and excited state dipoles.[44] In combination with a wave function optimization method based on a Car-Parrinello density matrix search (CP-DMS) with first-principles fictitious mass,[3] a novel technique that can obtain not only energies, but also the electron densities of doubly excited states within a single determinant framework is presented in Chapter 5.

Solvated Electronic Dynamics Solvation effects can change fundamental physical properties of the solute, drastically alter the outcome of chemical reactions, and either prevent or enhance the formation of certain macrostructures. In addition, solvents have been known to have a considerable impact on the stabilization of molecular electronic structures and dynamics, particularly states with strong permanent dipole moments, a characteristic of charge-transfer (CT) states,[45, 46] as well as chemical reaction rates due to the introduction of additional free energy of solvation. To better simulate the class of electronic dynamics taking place in the solution phase, the inclusion of solvent effects is always desirable and critically important for an accurate description.

A first-principles solvated electronic dynamics method is described in Chapter 6. Solvent electronic degrees of freedom are coupled to the time-dependent electronic density of a solute molecule by means of the implicit reaction field method, and the entire electronic system is propagated in time. This real-time time-dependent approach, incorporating the polarizable continuum solvation model (PCM), is shown to be very effective in describing the dynamical solvation effect in the charge transfer process and yields a consistent absorption spectrum in comparison to the conventional linear response results in solution.

Ultrafast Coherent Electron-Hole Separation Dynamics in a Fullerene Derivative The use of fullerene derivatives as electron donors in bulk heterojunctions is a promising development in the search for efficient energy conversion in hybrid solar cells. A long-lived photoexcited electron-hole pair will give rise to increased efficiency in photoenergy conversion. One way to prevent fast electron-hole recombination is to engineer fullerene derivatives that exhibit intrinsic electron-hole separation through accessible charge-transfer excited states.

In Chapter 7, the dynamics of photoexcited electron-hole pairs in a C_{60} derivative is studied using the real-time time-dependent density functional theory (RT-TDDFT) with inclusion of solvent effect by means of the implicit reaction field method. Although the charge-transfer excited state is not directly accessible from the ground state, intrinsic coherent electron-hole separation is observed following photoexcition as a result of direct coupling between excited states. Ultrafast charge-transfer dynamics is the dominant phenomenon in <60 fs after visible photoexcitation. This work provides insights into the characteristics of ultrafast dynamics in photoexcited fullerene derivatives, and aids in the rational design of efficient solar cells.

Chapter 2

EIGENSPACE UPDATE FOR MOLECULAR GEOMETRY OPTIMIZATION IN NONREDUNDANT INTERNAL COORDINATE

Following the discussions in the introductory chapter, this chapter presents an eigenspace update (ESU) method for molecular geometry optimization. This method takes advantage of previously computed eigenvectors for obtaining eigenspaces of the transformation **G** matrix and the Hessian maxtrix and exhibits an O(N^2) scaling. A select set of large molecules will be tested and compared with the conventional method of direct diagonalization in redundant space.

2.1 Eigenspace Update - An O(N^2) Algorithm for Molecular Geometry Optimization

Assume eigenvectors, $\mathbf{C}$, and eigenvalues, λ, of the Hessian exist at step i:

$$\mathbf{H}_i = \mathbf{C}_i \cdot \lambda_i \cdot \mathbf{C}_i^{\dagger} \tag{2.1}$$

A forward optimization step, $\Delta\mathbf{x}_i$, can be gained by means of RFO or TRM, using eq 1.5, resulting in a new geometry, $\mathbf{x}_{i+1}$; a new gradient, $\mathbf{g}_{i+1}$; and a new and updated Hessian, $\mathbf{H}_{i+1}$. In the current implementation, the Hessian is updated using a weighted combination of BFGS[23, 24] SR1,[25] and PSB,[20, 26] and SR1[25] with the square root of the Bofill[47] weighting factor (see refs [48] and [49] for the technical details). The new Hessian $\mathbf{H}_{i+1}$ can be projected into the previous eigenvector space $\mathbf{C}_i$ as

$$\Delta_{i+1} = \mathbf{C}_i^{\dagger} \cdot \mathbf{H}_{i+1} \cdot \mathbf{C}_i \tag{2.2}$$

The equation above can be considered as an intermediate diagonalization step. In principle, one can obtain the eigenvalues, λ_{i+1}, and eigenvectors, $\mathbf{C}_{i+1}$, of the Hessian by diagonalizing Δ_{i+1}:

$$\lambda_{i+1} = \mathbf{A}_{i+1}^{\dagger} \cdot \Delta_{i+1} \cdot \mathbf{A}_{i+1} \tag{2.3}$$

$$\mathbf{C}_{i+1} = \mathbf{C}_i \cdot \mathbf{A}_{i+1} \tag{2.4}$$

However, eqs 2.3 do not initially seem advantageous over the traditional approach of direct diagonalization of $\mathbf{H}_{i+1}$. From the molecular vibration standpoint, nonzero off-diagonal elements in eq 2.2 are related to vibrational couplings and anharmonicities. For any given normal mode, there exists a vibration which gives rise to the strongest coupling, or the largest off-diagonal element in Δ_{i+1}. Usually, in a nearly quadratic potential energy surface, changes in the Hessian matrix are small. If we only consider changes of the Hessian from the strongest couplings, Δ_{i+1} in eqs 2.3 and 2.4 can be replaced with a tridiagonal form, $\Delta_{3,i+1}$, where the only nonzero off-diagonal elements are the first diagonal below/above the main diagonal. Diagonalization of a tridiagonal matrix in eq 2.3 formally scales as $\mathrm{O}(N^2)$ when the *Divide and Conquer*[50] algorithm is employed. As a result, eqs 2.2 and 2.3 become an eigenvector and eigenvalue update scheme, which is much more efficient than direct diagonalization.

In later numerical tests, we use a LAPACK subroutine to obtain eigenvalues and eigenvectors of a tridiagonal matrix $\Delta_{3,i+1}$. The projected Hessian matrix Δ_{i+1} is reorganized by swapping rows/columns in every optimization step so that the largest off-diagonal element for any given mode is positioned in the first diagonal below/above the main diagonal. The reorganization starts from the first projection vector in $\mathbf{C}_i$. When the projected Hessian matrix is reorganized, the related projection eigenvectors Ci are also rearranged consistently according to the rows/columns being swapped in Δ_{i+1}. Note that this reorganization does not change the map between eigenvectors $\mathbf{C}$ and the geometric coordinates $\mathbf{x}$.

2.2 Transformation to Nonredundant Coordinate Space

Analytical gradients, $\mathbf{g}$, are usually computed in the Cartesian coordinate and require geometries, $\mathbf{x}$, represented in the same coordinate as well. The transformation from the Cartesian coordinate $\mathbf{x}$ to the redundant internal coordinate $\mathbf{q}$ can be done with a symmetric $\mathbf{G}$ matrix built from the Wilson texbfB matrix:[51]

$$\mathbf{B} = \frac{d\mathbf{q}}{d\mathbf{x}} \tag{2.5}$$

$$\mathbf{G} = \mathbf{B}\mathbf{B}^T \tag{2.6}$$

where $d\mathbf{q}$ and $d\mathbf{x}$ are infinitesimal displacements in internal and Cartesian coordinates, respectively. With the transformation matrices defined in eqs 2.5 and 2.6, the gradient and optimization step can be transformed between two representations (Cartesian and redundant internal):

$$\mathbf{f_q} = \mathbf{G}^{-}\mathbf{B}\mathbf{f_x} \tag{2.7}$$

$$\Delta\mathbf{x} = \mathbf{B}^T\mathbf{G}^{-}\Delta\mathbf{q} \tag{2.8}$$

where $\mathbf{f_x}$ and $\mathbf{f_q}$ are forces in the Cartesian and redundant internal coordinate, and the NewtonâĹŠRaphson step, $\Delta\mathbf{q}$, in the redundant internal coordinate is

$$\Delta\mathbf{q} = \mathbf{H}^{-1}\mathbf{f} \tag{2.9}$$

Note that in the quasi-Newton approach, the Hessian matrix can be updated in redundant internal coordinates without transformation back to the Cartesian coordinate.

For optimizations of large-scale systems, a smaller nonredundant coordinate space is preferred. The redundancy condition can be determined by single value decomposition (SVD) of the matrix $\mathbf{G}$:[30]

$$\mathbf{G} = (\mathbf{KL}) \begin{pmatrix} \mathbf{\Lambda} & 0 \\ \mathbf{0} & 0 \end{pmatrix} (\mathbf{KL})^T \,,\ \Lambda \neq 0 \tag{2.10}$$

In eq 2.10, $\mathbf{K}$ corresponds to the nonredundant coordinate space with nonzero eigenvalues Λ, and $\mathbf{L}$ consists of redundant eigenvectors of $\mathbf{G}$. However, obtaining the eigenspace of the $\mathbf{G}$ matrix is another $\mathrm{O}(N^3)$ procedure and speed-limiting step, and large molecules often have a large number of redundant coordinates. The eigenspace update concept introduced in section 2.1 can be used here to reduce the dimension of the $\mathbf{G}$ matrix. Assuming the linear dependence in the internal coordinate space remains the same from step to step, the full $\mathbf{G}$ matrix can then be reduced into the nonredundant coordinate space using the previous nonredundant vectors $\mathbf{K}$, followed by an SVD of the reduced and much smaller $\tilde{\mathbf{G}}$ matrix.

$$\tilde{\mathbf{G}} = \mathbf{K}_i^T \cdot \mathbf{G}_{i+1} \cdot \mathbf{K}_i \tag{2.11}$$

$$\tilde{\mathbf{G}} = \mathbf{U}_{i+1} \cdot \mathbf{\Lambda}_{i+1} \cdot \mathbf{U}_{i+1}^T \tag{2.12}$$

The nonredundant coordinate space at the $i+1$ step can be constructed accordingly:

$$\mathbf{K}_{i+1} = \mathbf{K}_i \cdot \mathbf{U}_{i+1} \tag{2.13}$$

The SVD of the full $\mathbf{G}$ matrix in redundant internal space is performed only once in the first step. Subsequent geometry optimization steps will take advantage of this eigenspace update scheme (eqs 2.11-2.13) to obtain the nonredundant coordinate space $\mathbf{K}_{i+1}$. As the reduced $\tilde{\mathbf{G}}$ matrix is significantly smaller than the original $\mathbf{G}$ matrix in redundant space, the SVD on $\tilde{\mathbf{G}}$ is no longer computationally dominant. As a result, obtaining the redundantâĹŠnonredundant transformation matrix $\mathbf{K}_{i+1}$ becomes a pseudo-$\mathrm{O}(N^2)$ approach.

With the eigenspace of the nonredundant internal coordinate, the NewtonâĹŠRaphson step in eq 2.9 can be transformed into the nonredundant internal coordinate space with the following equation:

$$\mathbf{K}^{-1}\Delta\mathbf{q} = \left(\mathbf{K}^T\mathbf{H}\mathbf{K}\right)^{-1}\mathbf{K}^T\mathbf{f} \tag{2.14}$$

If we define the Newton-Raphson step, Hessian, and force in the nonredundant internal coordinates as

$$\Delta\tilde{\mathbf{q}} = \mathbf{K}^{-1}\Delta\mathbf{q} \tag{2.15}$$

$$\tilde{\mathbf{H}} = \mathbf{K}^{T}\mathbf{H}\mathbf{K} \tag{2.16}$$

$$\tilde{\mathbf{f}} = \mathbf{K}^{T}\mathbf{f} \tag{2.17}$$

eq 2.14 becomes the familiar form of the Newton-Raphson step, but in the nonredundant internal coordinate space:

$$\Delta\tilde{\mathbf{q}} = \tilde{\mathbf{H}}^{-1}\tilde{\mathbf{f}} \tag{2.18}$$

The RFO correction can be applied to eq 2.18 with the Hessian eigenspace update scheme presented in the previous section. The displacement is then transformed back to redundant internal coordinate:

$$\Delta\mathbf{q} = \mathbf{K}\Delta\tilde{\mathbf{q}} \tag{2.19}$$

followed by another transformation to the Cartesian coordinate using the curvilinear eq 2.8 through an iterative approach.[30]

2.3 Computational Details

Optimizations are carried out using the AM1 Hamiltonian as implemented in the development version of the Gaussian program[52] with the addition of the geometry optimization algorithm using the eigenspace update (ESU) method in the nonredundant internal coordinate presented in sections 2.1 and 2.2. For all test cases, the geometry optimization is considered converged when the maximum component of the force vector is less than 4.5×10^4 au, the root-mean-square (RMS) force is less than 3×10^4 au, the maximum component of the geometry displacement is less than 1.8×10^3 au, and the RMS geometry displacement is less than 1.2×10^3 au. To

ensure a smooth convergence, the tridiagonal approximation of the reduced Hessian matrix is turned on when the regular RFO correction is smaller than one-tenth of the minimum Hessian eigenvalue. In the following discussion, we refer to a geometry step as the procedure including (1) forming the Wilson **B** matrix; (2) obtaining the nonredundant eigenspace (section 2.2), (3) Hessian update, and (4) diagonalization or eigenspace update (section 2.1); and (5) solving the RFO equation. For semiempirical and force field methods, the computational cost of the analytical gradient is not considered to be a computationally expensive step.

2.4 Benchmarks and Performance

In the ESU approach, the Hessian eigenspace is usually an approximation and requires a number of optimization steps to converge to the true value. Figure 2.1 shows the convergence of the Hessian eigenspace using the ESU method and direct diagonalization of the updated Hessian, compared to the true analytical Hessian. It is known that the Hessian update scheme is able to converge to the true Hessian within a few geometry steps. Built on the Hessian update scheme, the Hessian eigenspace update method (section 2.1) adds an additional degree of approximation. Therefore, the convergence behavior of the ESU approach is slower than the diagonalization-based method, but only by a few geometry steps. Nevertheless, the gain in computational speed owing to the $O(N^2)$ scaling and the nonredundancy is promising for large scale systems.

Table 2.1 lists relative computational costs for geometry optimizations using the ESU method for a select set of molecules compared to those obtained with full diagonalization in the redundant internal coordinate. The computational cost is evaluated using the total CPU time of geometry steps of the Hessian diagonalization-based RFO approach as the unit reference. For smaller molecules, such as hydrazobenzene, there

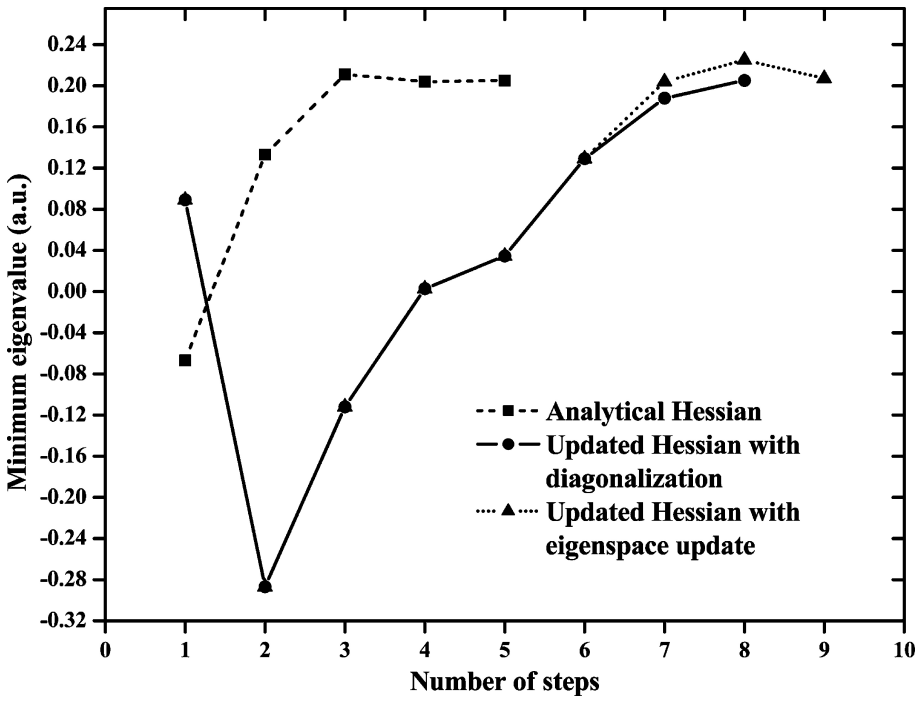

Figure 2.1: Comparison of minimum eigenvalues of the Hessian during optimization of a single water molecule, using analytical Hessian, updated Hessian with diagonalization, and Hessian eigenspace update approaches.

are no savings in the overall computational cost. Although the computational cost for geometry steps is reduced, the approximate nature of the Hessian eigenspace in ESU leads to several additional optimization steps compared to the diagonalization-based RFO approach. As a result, additional computational cost incurs, arising from additional SCF steps, and therefore the application of ESU for small molecules is not particularly advantageous.

Table 2.1: Comparison of Computational Costs for RFO Approach Using the Diagonalization in Redundant Space and Eigenspace Update Method

		diagonalization in redundant space			eigenspace update		
molecules (# of atoms)	energy (au)	geom[b]	SCF	steps[c]	geom[b]	SCF	steps[c]
hydrazobenzene (26)	0.129468	1.00	8.70	20	0.52	8.70	20
taxolâĂĽ(113)	âĹŠ0.666862	1.00	0.68	63	0.45	0.71	66
for-$(Ala)_{10}$-NH_2âĂĽ(106)	âĹŠ0.733344	1.00	0.82	100	0.66	0.97	115
for-$(Ala)_{20}$-NH_2âĂĽ(206)	âĹŠ1.424445	1.00	0.63	206	0.52	0.70	238
for-$(Ala)_{25}$-NH_2âĂĽ(259)	âĹŠ1.779332	1.00	0.48	82	0.38	0.50	87
crambinâĂĽ(642)	âĹŠ4.167923	1.00	0.27	389			
crambinâĂĽ(642)	âĹŠ4.169380				0.20	0.23	333

[a] The computational cost is evaluated using the total CPU time of geometry steps using full diagonalization in redundant internal coordinate as the unit reference.

[b] One geometry step includes forming the Wilson **B** matrix; obtaining the nonredundant eigenspace, Hessian update, diagonalization, or eigenspace update; and solving the RFO equation.

[c] Total number of geometry optimization steps.

On the other hand, as the molecular size increases, the cost for geometry steps becomes dominant in computational cost for semiempirical self-consistent field (SCF)

or force field energy calculations. In Table 2.1, we include test cases of large-scale molecules, such as taxol, alanine chains, and crambin. Because of excessive nuclear and electronic degrees of freedom, and numerous undesirable shallow potential wells on the PES, these molecules are often difficult and computationally expensive to optimize. As the nuclear degrees of freedom increase, the computational cost of the ESU-based method is noticeably less expensive than the conventional approach using full diagonalization in redundant coordinates. For the 25-alanine chain case, a 60% computational saving is observed. In this case, the total computational cost for SCF iterations in the ESU-based method is slightly (1%) more expensive than the conventional approach due to a slightly larger number of geometry steps. Therefore, such a large computational savings in the ESU-based method can be ascribed to the efficient eigenspace update algorithm in nonredundant internal coordinate space introduced herein. Although we cannot make a direct comparison for the largest test case, crambin, as the two methods converge to different minima,[53] a factor of 3 in computational cost is definitely noticeable.

To further understand the computational performance of the ESU approach, we plot in Figure 2.2 the computational cost of a single geometry step as a function of the number of atoms. It is clear that ESU is an O(N^2) method while the diagonalization-based approach exhibits an O(N^3) scaling. As the molecular sizes increase, the advantage of using an O(N^2) approach becomes highly appreciated. Figure 2.3 illustrate optimization processes of selected large-sized molecules: taxol, alanine-25, and crambin at the AM1 level of theory. It shows that the ESU method takes a similar optimization pathway as diagonalization in the redundant-space-based RFO approach but has the advantage of being much more efficient.

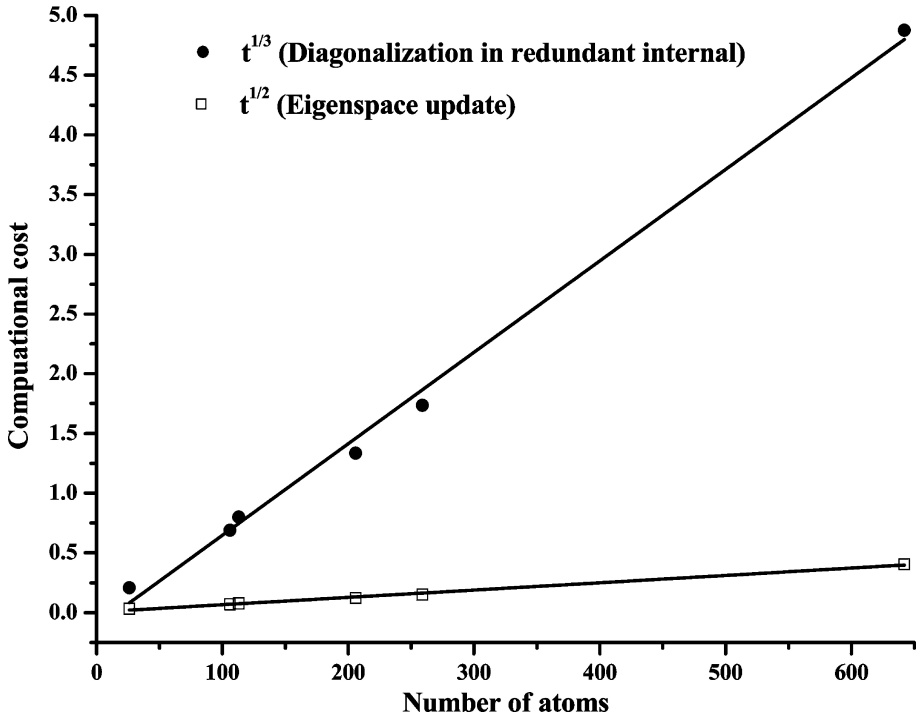

Figure 2.2: Comparison of computational costs using diagonalization in the redundant coordinate and eigenspace update. The computational cost of a single optimization step is plotted against the number of atoms.

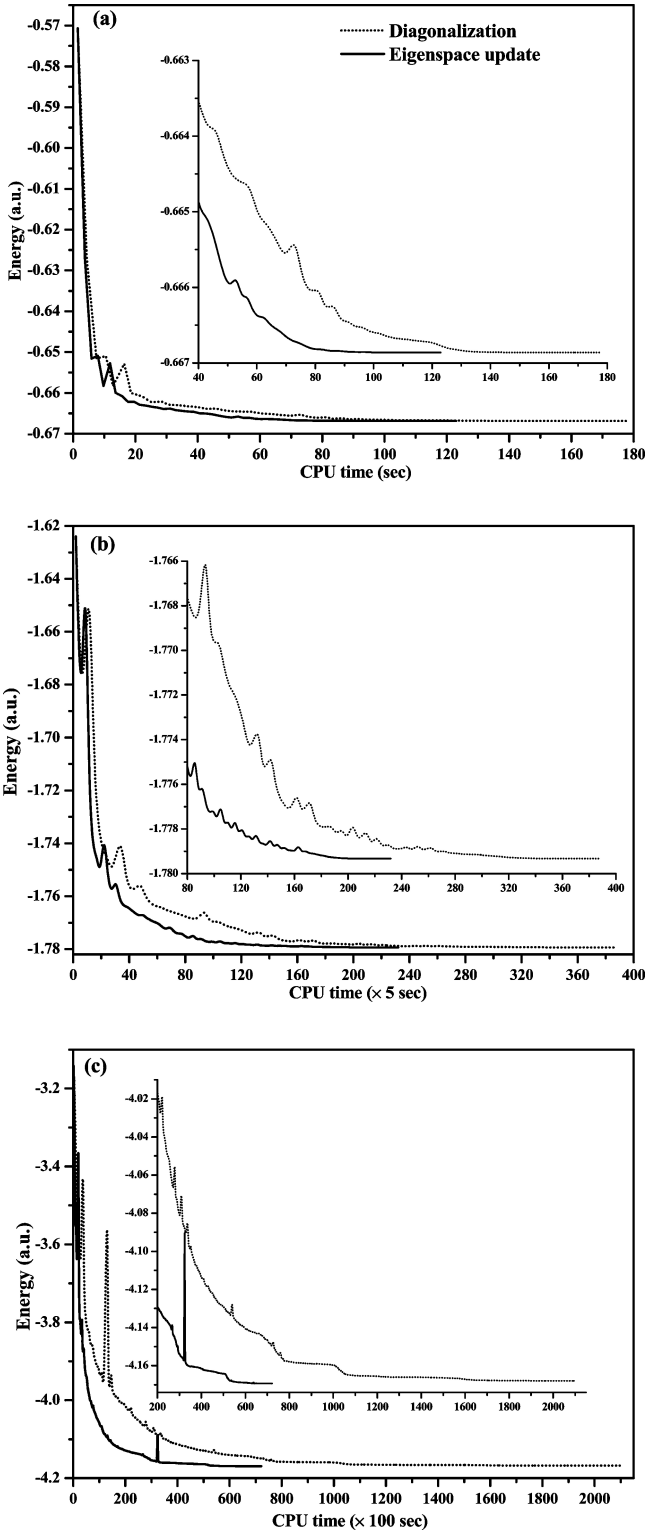

Figure 2.3: Comparison of optimizations using diagonalization in redundant space and eigenspace update methods for (a) taxol, (b) 25-alanine chain, and (c) crambin at the AM1 level of theory. See Table 2.1 regarding the evaluation of computational cost.

2.5 Conclusions and Future Prospects

This chapter presents a geometry optimization method using an eigenspace update approach. An encouraging efficiency for geometry optimization is observed, with up to a factor of 3 savings in computational cost for large-sized molecular systems like 25-alanine chain molecule. Meanwhile, the optimization pathways are similar to those using conventional diagonalization in the redundant-space-based RFO approach.

One possibly more promising implementation of the ESU method would be combination with direct inversion in the iterative subspace algorithm (DIIS), as exemplified by the energy-represented DIIS[49] and the simultaneous DIIS methods.[53]

Chapter 3

CAR-PARRINELLO DENSITY MATRIX SEARCH METHOD FOR ELECTRONIC WAVE FUNCTION OPTIMIZATION

This chapter introduces a first-principles fictitious mass scheme to weigh each individual density element differently and instantaneously. As an alternative to diagonalization in SCF, the Car-Parrinello scheme is implemented as a density matrix search method by dampening the electronic density velocity at each step to ensure a down-hill minimization.

The DMS algorithm presented later is formulated in an orthonormal basis. Transformations from an atomic orbital (AO) basis to an orthonormal basis can be done using the Löwdin[54] or Cholesky methods[55] (see refs [36, 37] for details). The Cholesky transformation is preferred in the context of linear scaling SCF because the computational cost of forming the sparse transformation matrices exhibits O(N) scaling with respect to the number of basis functions.

3.1 Dampened velocity CP-DMS

In an orthonormal basis, the extended Lagrangian for an electronic system can be written as [56]

$$L = \frac{1}{2}Tr(\mathbf{V}^T\mathbf{M}\mathbf{V}) + \frac{1}{2}mTr[\mathbf{W}\mathbf{W}] - E(\mathbf{R},\mathbf{P}) - Tr[\Lambda(\mathbf{P}\mathbf{P}-\mathbf{P})] \qquad (3.1)$$

where $\mathbf{M}$, $\mathbf{R}$, and $\mathbf{V}$ are the nuclear mass, position, and velocity, respectively. $\mathbf{P}$, $\mathbf{W}$, and m are the density matrix, density matrix velocity, and the uniform fictitious

electron mass, respectively. $\mathbf{\Lambda}$ is a Lagrangian constraint for the conservation of the number of electrons and idempotency of the density matrix. Equation 3.1 is the well-known CP Lagrangian equation in the orthonormal atomic basis.

Using the principle of stationary action, the Euler-Lagrange equation for the propagation of the density is given by

$$m\frac{d^2\mathbf{P}}{dt^2} = -\left[\left.\frac{\partial \mathbf{E}(\mathbf{R},\mathbf{P})}{\partial \mathbf{P}}\right|_{\mathbf{R}} + \mathbf{\Lambda P} + \mathbf{P\Lambda} - \mathbf{\Lambda}\right] \tag{3.2}$$

Equation 3.2 can be integrated using the velocity-Verlet algorithm

$$\mathbf{P}_i + 1 = \mathbf{P}_i + \mathbf{W}_i\Delta t - \frac{\Delta t^2}{2}m^{-1}\left[\left.\frac{\partial \mathbf{E}(\mathbf{R},\mathbf{P})}{\partial \mathbf{P}}\right|_{\mathbf{R}} + \mathbf{\Lambda}_i\mathbf{P}_i + \mathbf{P}_i\mathbf{\Lambda}_i - \mathbf{\Lambda}_i\right] \tag{3.3}$$

As in QN-DMS[36] and ADMP[39], the gradient term is a modified Li-Nunes-Vanderbilt (LNV) functional,[57]

$$\left.\frac{\partial \mathbf{E}(\mathbf{R},\mathbf{P})}{\partial \mathbf{P}}\right|_{\mathbf{R}} = 3\mathbf{FP} + 3\mathbf{PF} - 2\mathbf{FP}^2 - 2\mathbf{PFP} - 2\mathbf{P^2F} \tag{3.4}$$

Equations 3.1-3.4 have been successfully implemented as the ADMP method for molecular dynamics studies.[39, 56, 58–60] The underpinnings of the CP or ADMP approach are to maintain adiabaticity and energy conservation using the classical equation of motion for electrons, which can be integrated with many first order methods.

In the context of searching for a self-consistent minimum of the electronic wave function, the first term, the nuclear kinetic energy, in eq 3.1 becomes a constant, which can be conveniently set to zero. The idea of using eqs 3.1-3.4 for optimizations of electronic wave functions is to lower the potential energy term in the Lagrangian. In this paper, we use a dampened velocity method where the electronic translational kinetic energy [the second term in eq 3.1] is dampened at each integration step. This simple idea leads to a modified Verlet integration,

$$\mathbf{P}_{i+1} = \mathbf{P}_i - \frac{\Delta t^2}{2}m^{-1}\left[\left.\frac{\partial \mathbf{E}(\mathbf{R},\mathbf{P})}{\partial \mathbf{P}}\right|_{i,\mathbf{R}} + \mathbf{\Lambda}_i\mathbf{P}_i + \mathbf{P}_i\mathbf{\Lambda}_i - \mathbf{\Lambda}_i\right] \tag{3.5}$$

When m is a constant scalar, eq 3.5 shares a similar form as the steepest decent approach. As a first order approach, the computational cost of eq 3.5 is linear with respect to the number of elements. However, a first order based minimization scheme is generally slow, and not efficient for wave function optimization. In the next section, we introduce a first-principles fictitious electron mass method that exhibits a stable and fast SCF convergence.

3.2 First-principles fictitious electron mass

During the wave function optimization process, electrons experience a different potential at any given step. The key to improving gradient-based DMS is to allow the propagation scheme to adapt to the instantaneous potential. We herein derive a first-principles fictitious electron mass scheme that is independent of system of choice.

The frequency of a quantum mechanical electronic harmonic oscillator, $\omega = \sqrt{k/m}$, suggests that an appropriate form for the fictitious mass would be $m = k/\omega^2$, where k is the force constant and ω the frequency associated with each electronic element. The fundamental electronic element in the DMS scheme is the density matrix element $P_{\mu\nu}$ which leads to an associated fictitious mass of

$$m_{\mu\nu} = \frac{k_{\mu\nu}}{\omega_{\mu\nu}^2} \tag{3.6}$$

where μ and ν are indices for orthonormal atomic basis. Equation 3.6 is a good approximation for electrons near the bottom of the electronic potential well or close to the adiabatic surface. For an idempotent density matrix, $\partial E(\mathbf{R}, \mathbf{P})/\partial \mathbf{P}$ in eq 3.4 is equivalent to $(\mathbf{I} - \mathbf{P})[\mathbf{F}, \mathbf{P}]$. In a quadratic electronic potential, $\partial E(\mathbf{R}, \mathbf{P})/\partial P_{\mu\nu} = k_{\mu\nu}\Delta P_{\mu\nu}$. As a result, the fictitious electron mass scheme in eq 3.6 is related to the $[\mathbf{F}, \mathbf{P}]$ commutator, consistent with that found in ref [61]. As eq 3.6 is a second order approach with information about instantaneous curvature of the electronic potential, it, in principle, provides a better description of local electronic configuration. On the

other hand, because eq 3.6 is essentially a decoupled electronic oscillation model, it may have difficulties for highly coupled/correlated electronic systems. To support the method introduced here, we will present in section 3.5 (Benchmarks and Performance) some results for highly correlated systems.

The necessary force constants can be approximated from the diagonal elements of the Hessian matrix, which can be calculated directly from the density and Fock matrices[36, 37]

$$\begin{aligned} k_{\mu\nu} \approx H_{\mu\nu,\mu\nu} &= (3 - 2P_{\mu\mu})F_{\nu\nu} + (3 - 2P_{\nu\nu})F_{\mu\mu} \\ &-2(\mathbf{PF})_{\mu\mu} - 2(\mathbf{PF})_{\nu\nu} - 2(\mathbf{FP})_{\nu\nu} - 2(\mathbf{FP})_{\nu\nu} \end{aligned} \tag{3.7}$$

Note that eq 3.7 is a simple approximation to the rank-2 Hessian using some elements from the rank-4 Hessian tensor without computationally expensive two-electron integrals. Therefore, eq 3.7 does not impose any significant computational cost and storage requirements for approximate diagonal Hessian elements. The frequency for each density element is given by

$$\omega_{\mu\nu} = \frac{\varepsilon_{\mu\nu}}{\hbar} = \mathbf{F}_{\mu\nu}\mathbf{P}_{\nu\mu} \tag{3.8}$$

Equations 3.6-3.8 illustrate the first-principles fictitious electron mass scheme used in the CP-DMS scheme introduced in this paper. As a result, eq 3.5 becomes,

$$P^{*}_{i+1,\mu\nu} = P_{i,\mu\nu} - m^{-1}_{\mu\nu}\left[\frac{\partial \mathbf{E}(\mathbf{R},\mathbf{P})}{\partial \mathbf{P}}\bigg|_{i,\mathbf{R}}\right] \tag{3.9}$$

where density, gradient, and fictitious mass matrices are used as vectors. The Lagrangian constraint is dropped from eq 3.9, and will be enforced directly by an iterative procedure, discussed in the next section.

As in standard electronic structure theory, the frequency in eq 3.8 is using the atomic heat of formation as the zero point reference, which leads to a negative frequency for electrons. In order to effectively use this fictitious mass scheme, we introduce an arbitrary zero point frequency ω_0 so that all electron elements have positive

frequencies. We also introduce a cutoff frequency ω_{core} so that only active electron elements are taken into account in the first-principles fictitious mass scheme,

$$m_{\mu\nu} = \begin{cases} \omega_0 & if \quad \omega_{\mu\nu} \leq \omega_{core} \\ \frac{k_{\mu\nu}}{(\omega_0 + \omega_{\mu\nu} - \omega_{core})^2} & if \quad \omega_{\mu\nu} > \omega_{core} \end{cases} \tag{3.10}$$

3.3 Constraints and matrix sparsity

As an alternative to explicitly calculating the Lagrangian constraint, the conservation of the number of electrons and idempotency of the density matrix are maintained by a simple scaling followed by McWeeny purifications[62]

$$\begin{aligned} \mathbf{P}_{i+1} &= \mathbf{P}^*_{i+1} \cdot \frac{N_e}{Tr\left[\mathbf{P}^*_{i+1}\right]} \\ \tilde{\mathbf{P}}_{i+1} &= 3\mathbf{P}^2_{i+1} - 2\mathbf{P}^3_{i+1} \end{aligned} \tag{3.11}$$

To achieve linear scaling, sparse matrix techniques are used. The computational cost is reduced by storing and manipulating only the significant matrix elements. In each DMS, the Fock and density matrices are enforced to have the same sparsity form of $\mathbf{F}$+$\mathbf{P}$.

3.4 Computational Details

Test cases were carried out on an SGI Altix 450 workstation (Intel dual core-Itanium 1.6 GHz with 48 GB of RAM) using the development version of the GAUSSIAN series of programs[52] with the addition of the CP-DMS algorithm presented here. For the CP-DMS method, the wave function is considered converged when the $\partial E(\mathbf{R}, \mathbf{P})/\partial \mathbf{P}$ is less than 10^3 a.u., and the root-mean-square $\partial E(\mathbf{R}, \mathbf{P})/\partial \mathbf{P}$ is less than 10^4 a.u. From a number of tests, it was found that for any choices of ω_0 and ω_{core}, there exists an optimal time step Δt which gives rise to the best SCF convergence. In

the following test jobs, we use an effective zero point frequency of $\omega_0 = 5.0$ a.u., a cutoff of ω_{core}= âĹŠ5.0 a.u. for core and valence electrons, and a time step of $\Delta t = 0.16$ a.u. This set of parameters has been tested extensively and consistently and shows excellent computational speed and SCF convergence. The matrix sparsity cutoff used in the following tests is 10^6 a.u. For each test case, all methods considered here converge the electronic wave function to the same minimum with no more than 1×10^5 a.u. difference in the final energy. For all the test cases, we used a least-squares minimization scheme based SCF method with the direct inversion of iterative subspace approach (see ref [63] for details).

3.5 Benchmarks and Performance

We compare in Figure 3.1 wave function optimizations using CP-DMS with a uniform fictitious mass and the first-principles fictitious mass scheme introduced here (section 3.2). Both methods are able to converge the electronic wave function, suggesting that damping the velocity in CP dynamics is effective in leading electronic degrees of freedom to a lower energy minimum. However, the convergence of CP-DMS using a uniform fictitious mass is very slow, and this has been the main reason that a CP-based method has not been successful in SCF wave function optimization. In sharp contrast to results using a uniform fictitious mass, the CP-DMS using our new fictitious mass scheme shows a fast and smooth convergence. Figure 3.1 serves merely as a proof for the efficiency of the new fictitious mass scheme developed here. In the following discussion, we refer to CP-DMS using the first-principles fictitious mass scheme simply as CP-DMS.

Figure 3.2 plots the computational costs as a function of system size using both the CP-DMS and conventional diagonalization based approaches. The test molecules are L-alanine chains terminated by a D-alanine with a helical secondary structure,

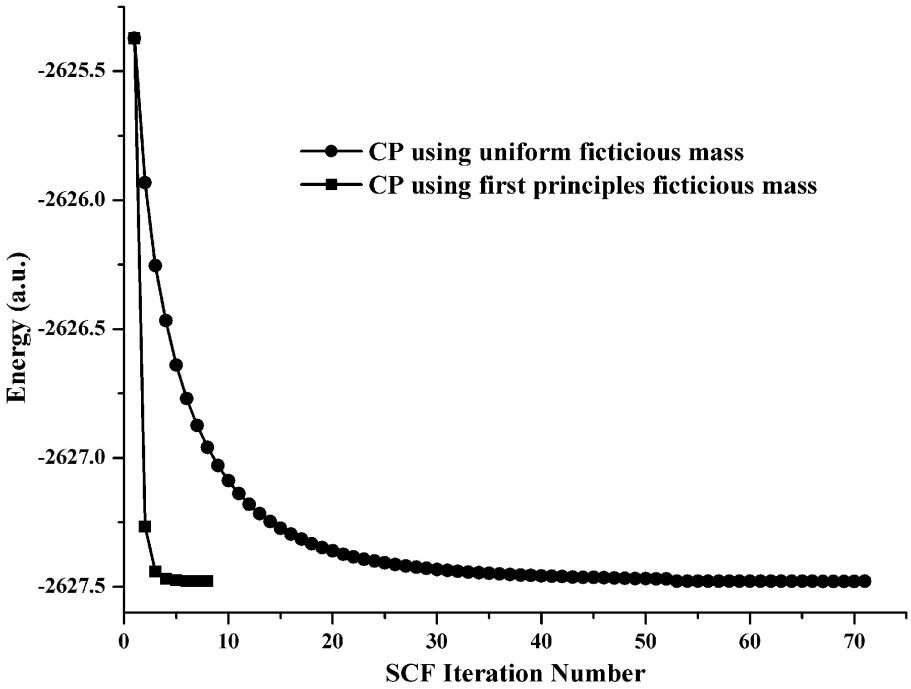

Figure 3.1: Comparison of SCF convergence using the Car-Parrinello method with dampened velocity for a uniform fictitious electron mass (m = 1 a.u.) and first-principles fictitious electron mass.

optimized at the AM1 level of theory. The 6-31G** Pople type basis set is used in this test to showcase the linear scaling of CP-DMS even for such a large basis set with polarization functions. As expected, the diagonalization scales as O(N^3), and it becomes computationally expensive at the large molecule limit. On the other hand, CP-DMS shows a linear scaling with respect to the system size for the alanine chain test cases. Although conventional diagonalization is still cheaper than CP-DMS in computational cost for systems with $<$ 10 000 basis functions, the linear scaling aspect of CP-DMS becomes significantly advantageous at the large molecule limit. Also note that diagonalization routines use fast LAPACK engines, while the sparse matrix manipulation has yet to be optimized. The CP-DMS method introduced here is formally an O(N^2) approach. The significant matrix sparsity of the large, linear molecule, as a result of many long-range integrals below the zero threshold, is the dominant factor that makes the CP-DMS algorithm exhibit linear scaling. In

addition, for each alanine test case, the number of SCF iterations using the CP-DMS method required to reach convergence is equal or comparable to the conventional method using diagonalizations. This, once again, shows that CP-DMS is not only a linear scaling method, but also a stable wave function optimizer with fast convergence.

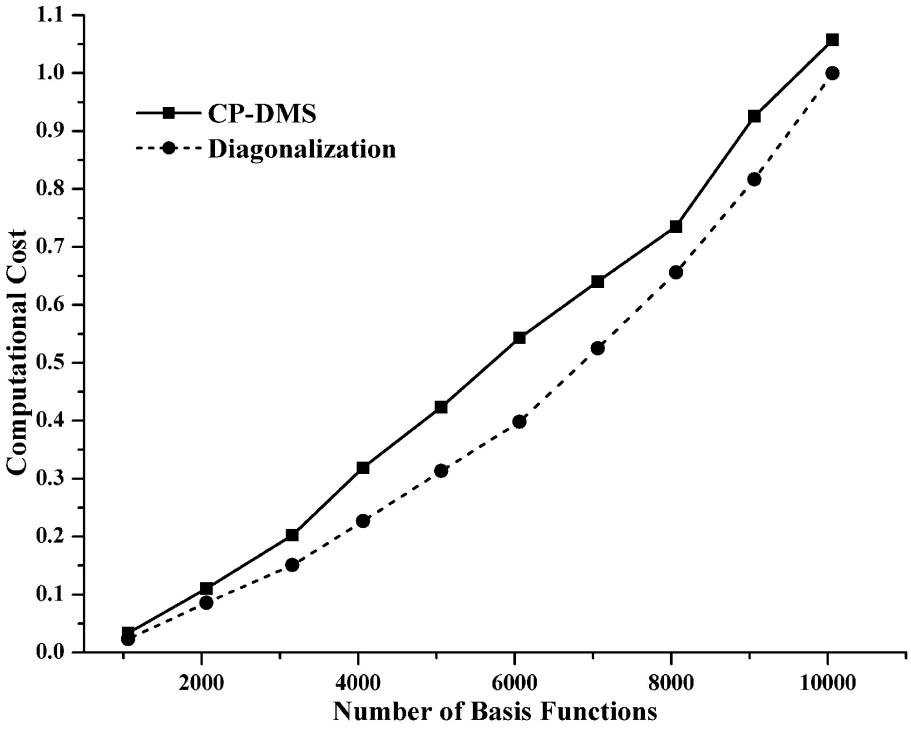

Figure 3.2: Comparison of the computational cost for a single SCF iteration using diagonalization and CP-DMS at the HF/6-31G** level of theory. Computational cost is expressed as a ratio of the CPU time of a single SCF iteration of the test case relative to that of the 100 alanine molecule.

While the above result shows that CP-DMS exhibits linear scaling for molecules with hydrocarbon backbones, wave function optimization methods for condensed matter have been an area that increasingly demands theoreticians' attention. Particularly, nanosized particles, such as ZnO and CdSe quantum dots, can be synthesized and characterized experimentally. Although computational research on nanoparticles seems to be computationally affordable at the limit of existing computational

resources, converging the wave function often becomes a very difficult task. Figure 3.3 shows a test case of a $Cd_{153}Se_{153}$ quantum dot, capped with pseudohydrogens (for the detailed capping scheme, see ref [64]), computed at the screened-exchange hybrid functional[65–67] HSE1PBE/LANL2MB+ (an additional set of S AO is added to the LANL2MB basis set) level of theory. Note that when core electrons are replaced with

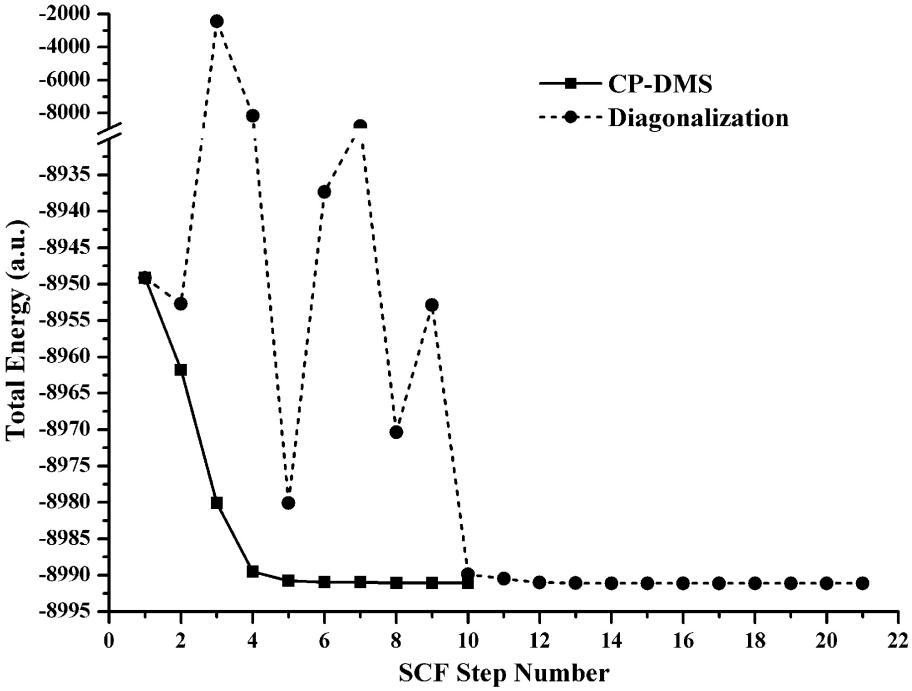

Figure 3.3: Comparison of SCF convergence using conventional diagonalization and CP-DMS for a $Cd_{153}Se_{153}$ quantum dot at the HSE1PBE/LANL2MB+ level of theory.

effective core potentials, they are no longer treated with AOs or as core electrons in the method developed. The conventional diagonalization undergoes drastic unproductive oscillations at the beginning of the wave function optimization, and takes 21 SCF iterations to reach self-consistency. Such a phenomenon is quite common in the Roothaan-Hall SCF approach using diagonalization when the curvature of the electronic degrees of freedom is very small or the electronic potential surface is very shallow, as in free electrons in conductors and semiconductors. In sharp contrast

to the performance of conventional SCF, CP-DMS converges the wave function in ten SCF iterations with smooth down-hill behavior. Derivations in section 3.2 indicate that the CP-DMS is essentially a simulated-annealing process with gradient corrections from the instantaneous electronic curvature/Hessian. In addition, the first-principles fictitious mass gives different weights to electrons with different energies. One can see from eq 3.6 that electrons with higher energies are associated with smaller masses, which leads to larger first order CP-DMS steps. As a result, active (high energy) electrons are converged faster than less active electrons, and the overall CP-DMS convergence scheme is progressive. Figure 3.4 plots the total computational cost as a function of the quantum dot size. For quantum dots considered here, the

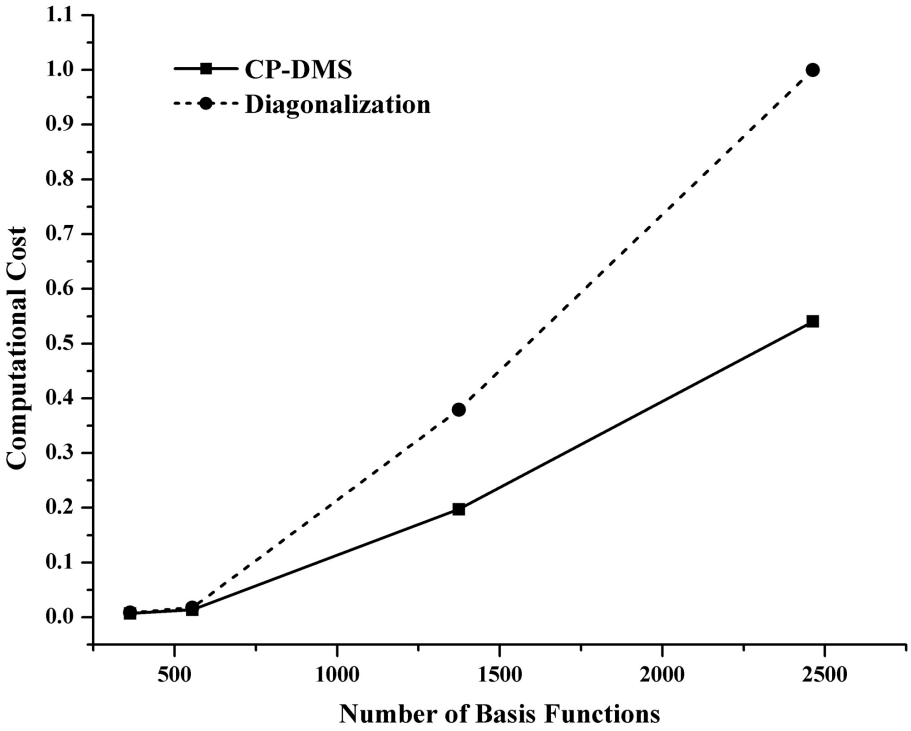

Figure 3.4: Comparison of the total computational cost of SCF wave function optimization using diagonalization and CP-DMS at the HSE1PBE/LANL2MB+ level of theory. Computational cost is expressed as a ratio of the total CPU time of the test case relative to that of a $Cd_{153}Se_{153}$ quantum dot.

number of integrals below the zero threshold is rather small due to their compact structure and diffuse valence electrons. Therefore, the CP-DMS exhibits an asymptotic quadratic scaling with respect to the system size. Because of its fast and smooth convergence, CP-DMS is consistently much less computationally expensive than the diagonalization based SCF method for all CdSe quantum dots tested here.

3.6 Conclusions and Future Prospects

We introduced a first-principles fictitious mass scheme derived from the electronic harmonic frequency. Force constants are evaluated as approximate diagonal elements of the Hessian matrix, and therefore the computational cost and memory storage requirements are trivial. Each individual electronic density element has a unique instantaneous fictitious mass in every SCF iteration. Not only is this new fictitious mass scheme independent of system of interest, it also leads to a much fast energy minimization toward a stationary state. The CP scheme described above is implemented as a DMS (CP-DMS) as an alternative to the O(N3) scaling diagonalization step in the SCF routine. The overall performance of CP-DMS can be summarized as:

- The new fictitious mass scheme leads to a much faster convergence of the electron wave function compared to the conventional uniform electron fictitious mass scheme in CP.

- For molecules with a hydrocarbon backbone, such as the alanine helical chains, CP-DMS exhibits a linear scaling with respect to the size of the system.

- For compact three-dimensional structures, such as CdSe quantum dots, wave function optimizations are often difficult tasks for conventional diagonalization based SCF.

Our tests show that CP-DMS is able to converge the wave function very smoothly, benefiting from the new fictitious mass scheme. As a result, the CP-DMS wave functional optimization shows a factor of 2-4 speed-up compared to diagonalization based SCF. The success of the frequency-dependent fictitious mass in wave function optimization bodes well for its future implementation in CPMD or ADMP. It will likely lead to much better energy conservation and larger step sizes in molecular dynamics simulations.

Chapter 4

TIME-DEPENDENT DENSITY FUNCTIONAL THEORY CALCULATIONS OF EHRENFEST DYNAMICS OF LASER CONTROLLED DISSOCIATIONS

Advanced laser techniques, such as ultrashort laser pulses, high-intensity electric fields, pulse shaping, and multiwave mixing, are able to provide increasing control of molecular electronic and vibrational excitation of target states.[68, 69] Although these advances offer possibilities to use tailored electromagnetic fields to control the outcome of a chemical reaction via a desired pathway, [70–74] the underpinnings of many laser control mechanisms still remain unclear. The difficulty lies in the complexity of the laser-molecule interaction. For example, just a few of the phenomena necessary to account for mechanism include the time-dependent Stark shift of the potential energy surfaces (PESs), possible multiphoton processes when intense laser fields are used, and nonadiabatic excitation of electronic states. Simple PES modeling is not sufficient, and nonadiabatic electron dynamics are necessary. Such complexity motivates the use of time-domain approaches to understand some aspects laser-molecule interactions and their effects on the outcome of molecular reactions. It is for this purpose that we developed *ab initio* Ehrenfest dynamics with TDHF[75] and TDDFT[76] as a computationally inexpensive alternative to full time-dependent Schrodinger equation (TDSE) approach.

This chapter first details the theory of *ab initio* direct Ehrenfest dynamics implemented with real-time time-dependent density functional theories (RT-TDDFT) approach. Next, two theoretical investigations will be presented on the laser-controlled

photo-dissociations of $C_2H_2^{2+}$ and NO^+ molecules.

Acetylene dication has attracted great interest in both experiments[77–79] and theoretical calculations,[80–83] due to its importance as a prototype of proton migration, and also because it is one of the smallest stable polyatomic dications. On the similar ground, the study of NO/NO^+ has been an intense area of research for both experiment[84, 85] and theoretical calculation[86–88] due to the physical and chemical processes occurring in the upper atmosphere and pollution problems. The goal of study on $C_2H_2^{2+}$ is to understand some aspects of laser control mechanism, while the purpose of the NO^+ study is to further explore the role of pulse length in the control mechanism.

4.1 ab initio Direct Ehrenfest Dynamics

Based on discussions of the single-particle Liouville equation in Chapter 1, the matrix form of TDHF/TDDFT equation in an orthonormal MO basis can be written as

$$i\frac{d\mathbf{P}}{dt} = \mathbf{KP} - \mathbf{PK} \tag{4.1}$$

where $\mathbf{P}$ and $\mathbf{K}$ are the density and Fock/Kohn-Sham matrices with matrix elements $\mathbf{P}_{\mu\nu} = \sum_i c_{\mu,i} c^{\dagger}_{\nu,i}$.

In practice, the *ab initio* direct Ehrenfest dynamics is implemented with a triple-split operator scheme with three different integrators: a modified midpoint and unitary transformation (MMUT) TDHF/TDDFT, a nuclear position coupled midpoint Fock/Kohn-Sham integrator and nuclear velocity-Verlet.[89] All energies, gradients, and properties are generated directly as needed, or "on the fly". The electronic degrees of freedom are propagated with a modified midpoint and unitary transformation method (MMUT).[90] The unitary transformation matrix is a time-evolution operator constructed from the eigenvectors $\mathbf{C}(t_k)$ and eigenvalues $\varepsilon(t_k)$ of the Fock/Kohn-Sham

matrix

$$\varepsilon(t_k) = \mathbf{C}^{\dagger}(t_k) \cdot \mathbf{K}(t_k) \cdot \mathbf{C}(t_k) \tag{4.2}$$

$$\begin{aligned} \mathbf{U}(t_k) &= exp\left[i \cdot \Delta t_e \cdot \mathbf{K}(t_k)\right] \\ &= \mathbf{C}(t_k) \cdot exp\left[i \cdot \Delta t_e \cdot \varepsilon(t_k)\right] \cdot C^{\dagger}(t_k) \end{aligned} \tag{4.3}$$

where Δt_e is the time step for the MMUT integrator. The density matrix is then propagated from time t_{k-1} to t_{k+1} with a fixed nuclear position

$$\mathbf{P}(t_{k+1}) = \mathbf{U}(t_k) \cdot \mathbf{P}(t_{k-1}) \cdot \mathbf{U}^{\dagger}(t_k) \tag{4.4}$$

By computing the Kohn-Sham matrix at the midpoint of the step, the MMUT method accounts for linear changes in the density matrix during the time step. Because the electronic wave function changes much faster than the nuclear motion, the nuclear position coupled midpoint Fock/Kohn-Sham propagator updates integrals required in the Fock/Kohn-Sham matrix with the second kind of time step Δt_{Ne}, which encompasses $m\Delta t_e$ iterations. The integrals are recomputed at the midpoint of every Δt_{Ne} time step, $t' + (\Delta t_{Ne})/2$, and are used in the Fock/Kohn-Sham matrix $\mathbf{K}$ for the m MMUT steps between t' and $t' + \Delta t_{Ne}$

$$\mathbf{K}(t) = \mathbf{h}\left[x\left(t' + \frac{\Delta t_{Ne}}{2}\right)\right] + \mathbf{G}_{xe}\left[\left(t' + \frac{\Delta t_{Ne}}{2}\right), \mathbf{P}(t)\right] \tag{4.5}$$

where $\mathbf{h}$ and $\mathbf{G}_{xe}$ are one and two electron matrices, respectively. The nuclear position is updated for $n\Delta t_{Ne}$ time steps before the gradient is recalculated, which occurs in the third time step $\Delta t_N = n\Delta t_{Ne}$. Velocity Verlet is used to propagate the nuclear coordinates

$$p(t_{k+1/2}) = p(t_k) - \frac{1}{2} g(t_k) \cdot \Delta t_N \tag{4.6}$$

$$x(t_{k+1}) = x(t_k) + \frac{p(t_{k+1/2})}{M} \cdot \Delta t_N \tag{4.7}$$

$$p(t_{k+1}) = p(t_{k+1/2}) - \frac{1}{2} g(t_{k+1}) \cdot \Delta t_N \tag{4.8}$$

where p is the momenta, and g is the energy gradient. The quantum mechanical gradient, for non-commuting Fock/Kohn-Sham and density matrices, $[\mathbf{K}, \mathbf{P}] \neq 0$, is generally different than that for Born-Oppenheimer dynamics.[75]

The time-dependent Kohn-Sham Hamiltonian includes the electron-field coupling term within the electric-dipole approximation,

$$\mathbf{K}(t) = \mathbf{K}_0(t) + \mathbf{d} \cdot e(t) \tag{4.9}$$

where K_0 is the field-free Fock/Kohn-Sham matrix, and $d_{\mu\nu} = \langle \chi_\mu | \, r \, | \chi_\nu \rangle$ is the dipole integral in the AO basis. We use a linearly polarized and spatially homogeneous external field of frequency ω and maximum field strength E_{max},

$$e(t) \approx E_{max} sin(\omega \cdot t) \tag{4.10}$$

As a result of eq 4.9, at any given time during the simulation, the total energy of the system including the electron-field coupling can be written as,

$$E(t) = Tr\left[\mathbf{P}(t) \cdot \left(\mathbf{K}(t) - \frac{1}{2}\mathbf{G}(t)\right)\right] = E_{mol}(t) + \mu(t) \cdot e(t) \tag{4.11}$$

where we define E_{mol} as the field-free energy of the molecule, and μ is the instantaneous dipole. In the current implementation of the TDDFT Ehrenfest dynamics, atom-centered basis functions are used in the MO expansion. As a result, electronic ionizations cannot be modeled directly. On the other hand, the focus of this work is to illustrate the crucial role of laser pulse length in the photo-absorption processes during the course of dissociative reaction.

4.2 Boltzmann Ensemble of Initial Conditions

Initial conditions were chosen to simulate a Boltzmann ensemble of harmonic oscillators at room temperature (298 K); For a specific vibrational mode with a given Boltzmann-sampled vibrational energy, the initial phase was chosen randomly and

classically. The total angular momentum was set to zero. Since the actual potential energy surface is not strictly harmonic, the initial vibrational coordinates and momenta generated by this procedure were scaled to correct for the anharmonicity.[91]

$C_2H_2^{2+}$ molecule A Boltzmann ensemble of acetylene dication molecules is simulated at room temperature (298 K). This ensemble assumes a broad geometric distribution of vibrational phases of the initial ground state ($^3\Sigma_g^-$) species from which the strong laser field interactions take place. A similar approach has been implemented for studies of Coulomb explosion of the acetylene dication.[83] A total of 50 initial conditions and trajectories were integrated for each set of applied field parameters. The C-H bonds are within about $\pm 0.15\mathring{A}$ of the equilibrium bond length of $1.14\mathring{A}$. Because the C-C bond is stronger, the distribution is not as broad, with 95% within $\pm 0.07\mathring{A}$ of the equilibrium of $1.35\mathring{A}$. Even though the minimum energy geometry of $C_2H_2^{2+}$ is linear, vibrational Boltzmann sampling of the bending modes allows deviation from exact linearity. The initial distribution of the H-C-C angle appears that 90% of the runs are within $\pm 25^\circ$ of the linear structure. In our simulations, fields are applied parallel and perpendicular to the axis described by the optimized linear structure, and this distribution indicates that most of the $C_2H_2^{2+}$ starting conditions give a structure that is close to linear.

NO^+ molecule Similar approach is applied to NO^+ molecule. A total of 50 trajectories were integrated for each set of field parameters. Initial conditions were chosen for the NO+ molecule to simulate a Boltzmann ensemble of harmonic oscillators at room temperature (298 K). The room temperature Boltzmann distribution of the initial N-O bond lengths shows that the initial N-O bond lengths are within about $\pm 0.08\mathring{A}$ of the equilibrium bond length of $1.08\mathring{A}$.

4.3 Computational Details

The modified development version of the GAUSSIAN(32) series of programs was used to carry out all computations in the present investigation. The BLYP functional with the 6-31++G(d,p) basis set is used for calculations of ground state properties and excited states within the linear response framework[92, 93] and is implemented with the Ehrenfest dynamics approach as described in section 4.1 for laser-controlled electron-molecule dynamics. In the Ehrenfest dynamics, a step size of t_N= 0.10 fs is used for the velocity Verlet, with $t_{Ne} = 0.01$ fs for the midpoint Kohn-Sham integrator, and $t_e = 0.001$ fs for the MMUT step. Tests showed that these time steps conserve the energy of the system (after field removal) to within 10^{-4} Hartree and represent a reasonable combination of accuracy and computational cost.

4.4 Results and Discussion: $C_2H_2^{2+}$ Simulation

The ground state of the acetylene dication has a triplet configuration ($^3\Sigma_g^-$) with two unpaired electrons each occupying one π_μ bonding orbital. Within our calculations, the molecular axis is along the z axis, and the two π bonds are aligned along the x and y axes. The ground-state optimized C-C bond length is $1.35\mathring{A}$, and the C-H bond length is $1.14\mathring{A}$. We use a constant envelope 20 fs laser pulse, with $E_{max} = 0.08$ au (which corresponds to a field intensity of $2 \times 10^{14} W/cm^2$). After the first 20 fs when the laser field is on, the molecular reaction continues until t = 150 fs. At the end of the simulation, the C-H and C-C bonds are considered broken if their length exceeds $3\mathring{A}$. We divide our nonadiabatic Ehrenfest molecular dynamics results into five dissociation pathways:

(1) no bonds are broken

(2) single-proton dissociation

(3) dissociation of both C-H bonds

(4) dissociation of all bonds

(5) proton dissociation with C-C dissociation

An additional pathway, with the C-C bond breaking with no C-H dissociation, is possible but was never observed in our simulations of the triplet state. Although a large torsional energy could break the C-C bond, the Boltzmann sampling shows that this mechanism is very unlikely at room temperature. This pathway is thought to occur through an excited singlet surface through a bent transition state.[81] Although vibrational sampling of the bending mode breaks the strict linear symmetry of the optimized structure, the results of our simulations can be broadly divided into two different categories: laser application perpendicular to the molecular axis and laser application along the molecular axis. Although this division is made for the ease of interpreting our theoretical results, intense laser pulses can be used to produce alignment of even nonpolar molecules, with the molecule aligning with its most polarizable axis along the laser polarization direction.[94–97] Within our scheme, this technique could be used to provide greater control of the molecular dissociation.

E-Field Perpendicular to the Molecular Axis When a 20 fs laser pulse was applied in the xy plane (perpendicular to the molecular z axis, with $E_{max} = 0.057$ au along both the x and y axes), no bonds were broken within the experimentally relevant range of photon energies 1.5 eV = 800 nm (titanium-sapphire laser) to 8.3 eV = 157 nm (an ArF excimer laser, the high-energy range of current laser technology). We increased the photon energy and found that no bonds broke until we reached an extremely high photon energy of 13.6 eV = 91.2 nm. This high-energy field frequency did not lend itself to controlled dissociation, however, as there were many dissociation pathways accessed, but none of them dominant. With the 13.6 eV photon energy xy field, the distribution of the five dissociation pathways is shown in Figure 4.1. The

percentages range from 10% (pathway 5: dissociation of a single C-H bond with C-C dissociation) to 30% (pathway 3: dissociation of both C-H bonds). Thus, when the laser field is aligned perpendicular to the molecular axis, the probability of controlling molecular dissociation of $C_2H_2^{2+}$ is rather small.

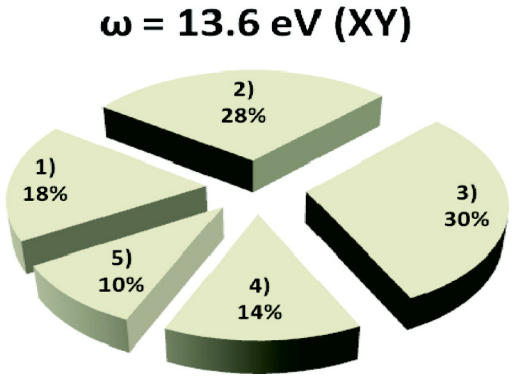

Figure 4.1: Percentages of various dissociation pathways with an xy laser field with a frequency of $\omega = 13.6$ eV.

We next analyze the corresponding xy-allowed excited states. Figures 4.2a and 4.2b show the PESs for the four lowest energy xy-dipole-allowed electronic transitions as functions of C-H and C-C distances, respectively, as well as the PES of the ground state. For the PESs in Figure 4.2a, the C-H bonds were symmetrically stretched. The vertical lines indicate the maximum and minimum starting bond lengths in the Boltzmann ensemble. The two lowest lying excited states in Figures 4.2a and 4.2b correspond to excitation from the C-H bonding ÏČg orbital to the C-C bonding ÏĂu orbital, which should weaken the C-H bond and meanwhile strengthen the C-C bond. The lowest energy excited state should be accessible with a field frequency ω of 5 eV = 248 nm when the field is aligned in the xy plane. Although it seems that this excitation provides a desirable control scheme for selective bond breakage since it weakens the C-H bond while strengthening the C-C bond, these $\sigma \rightarrow \pi$ transitions are only weakly allowed in the xy plane (oscillator strength f < 0.004), even at stretched bond lengths. The second highest xy-allowed excited state is also very weakly allowed.

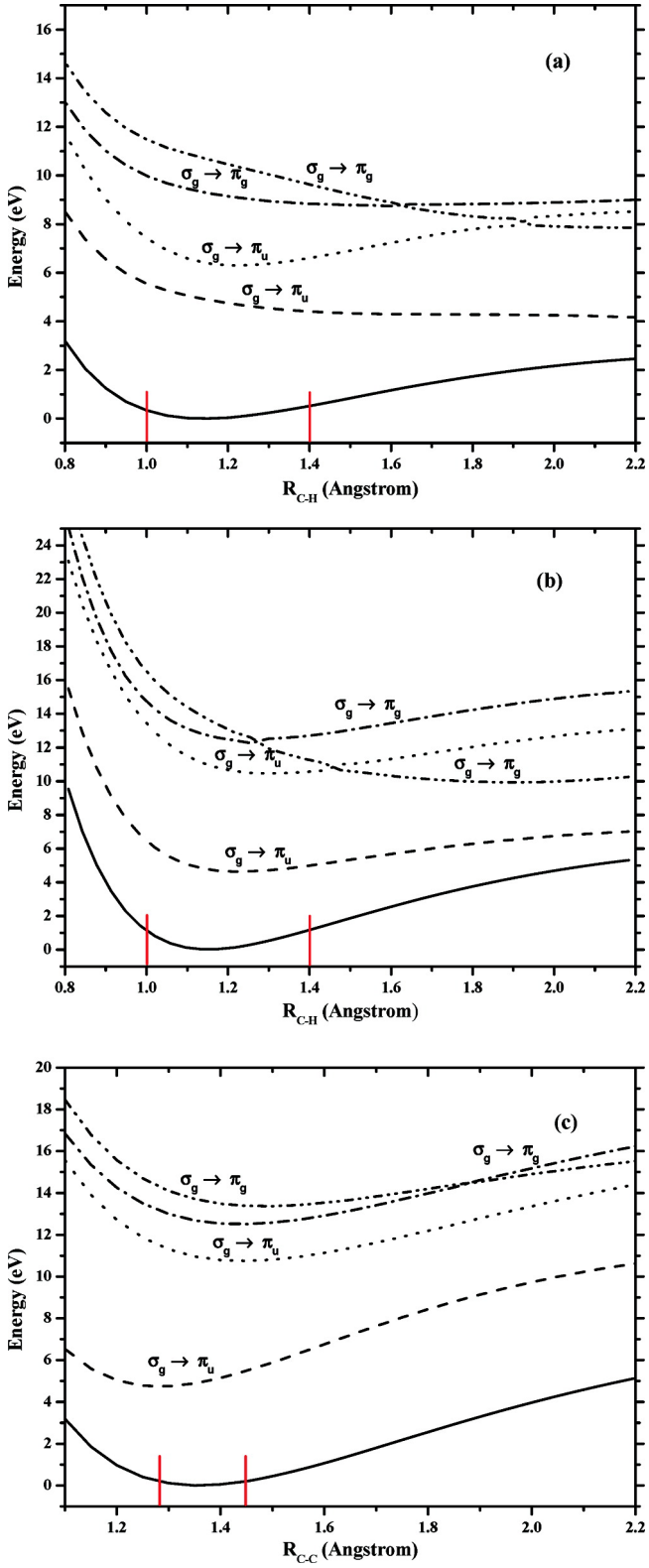

Figure 4.2: Potential energy surfaces for $C_2H_2^{2+}$. Red lines indicate the range of bond lengths within the room temperature Boltzmann distribution: (a) xy- allowed states for the asymmetric C-H stretch; one C-H bond is stretched while the other is optimized, (b) xy-allowed states for the symmetric C-H stretch; both C-H bonds have the same length, and (c) xy-allowed states for the C-C stretch.

The two higher energy excitations in Figures 4.2a and 4.2b correspond to excitations from the C-H bonding σ_g orbital to the C-C antibonding π_g orbital, which weakens both the C-H and C-C bonds. While transitions to these states are not highly allowed, the oscillator strength of the fourth excited state, at 14 eV, is a bit larger than the other xy states; it ranges between f = 0.2 and 0.03, indicating that population of this state is likely responsible for the dissociations observed with the 13.6 eV field. In addition to this state having a non-minimal oscillator strength, it is also seen to be repulsive along both the C-C and C-H bond coordinates, allowing for direct dissociation. We thus see that while the first of the xy transitions is in the experimental photon energy range, the very small oscillator strength of this state keeps it from being available to $C_2H_2^{2+}$ upon excitation with an applied laser field. Population of a higher lying state, at an energy well beyond the reach of today's experimental laser technology, is theoretically possible due to a larger oscillator strength. It appears to be this repulsive state that causes the various dissociations seen in Figure 4.1.

E-Field Parallel to the Molecular Axis When the laser field is aligned along the molecular z axis, there is a wide range of dissociation patterns observed. Figure 4.3 shows the distribution of the various five pathways for four different photon energies. In all tested laser fields, the C-H dissociation channels (pathways 2 and 3) are the most probable reaction pathways. At the lowest photon energy, 9.5 eV, single C-H dissociation, pathway 2, is the dominant dissociation channel. When the photon energy increases, the probability of double C-H bond dissociation, pathway 3, also increases. The Ehrenfest trajectories at the lower photon energies (<12 eV) do not undergo C-C dissociation. When the photon energy is above 12 eV, the C-C dissociation channel is open; however, these higher photon energies also lead to C-H dissociation. Therefore, a simple frequency control scheme as explored here on the triplet surface is not able to break the C-C bond while maintaining the C-H bonds,

but at a frequency of 9.5 eV, we are, in fact, able to selectively break only one of the C-H bonds since pathway 2 dominates over pathway 3. At higher frequencies, the double C-H dissociation of pathway 3 dominates. Examination of the energy profiles during the dynamics indicates that trajectories with a 10 eV or greater increase in the potential energy when the field is on are likely to experience dissociation. As the dynamics continue, some of this large potential energy is transferred to the kinetic energy of the $C_2H_2^{2+}$ fragments.

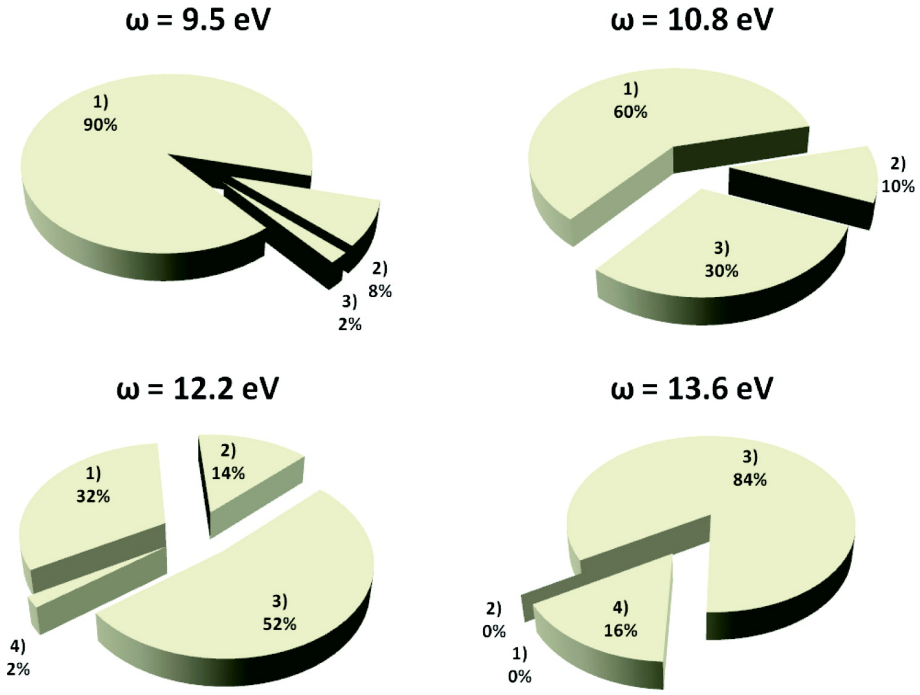

Figure 4.3: Percentages of various dissociation pathways with a z laser field. The five different pathways are given in Figure 4.1 and in the text.

With double C-H dissociation, we find that the charge profile of the fragments varies with laser frequency. Since Ehrenfest dynamics propagates the nuclear motion on an average potential energy surface, the final partial charge indicates probabilities of dissociation on various surfaces. At higher frequencies, we find that each hydrogen has a larger positive charge, with the C_2 fragment holding onto the positive charge

more with the lower 10.8 eV frequency. This means that higher frequency laser fields are more likely to lead to double-proton dissociation, while lower frequency laser fields are more likely to lead to single-proton dissociation, followed by dissociation of neutral hydrogen.

As with the perpendicular xy laser field, we rationalize these dissociation patterns through analysis of the electronic excitations. Figures 4.4a-c are the PESs for z-allowed transitions for symmetric and asymmetric C-H bond breakage and C-C bond breakage. The lowest energy excited state is z-dipole-allowed; the oscillator strength f ranges from 0.2 to 0.4 within the initial Boltzmann geometries (marked with a vertical line). This lowest energy state corresponds to excitation from the C-C π_μ bonding orbital to the C-C π_g^* antibonding orbital, which should lead to C-C bond weakening followed by a possible dissociation. Along the C-H coordinate this first excited state has a shallow potential well, while along the C-C coordinate the PES is very flat. The second and third excited-state PESs in Figures 4.4a-c correspond to excitation from the C-H bonding σ_g orbital to the C-H antibonding σ_μ^* orbital. This kind of excitation will result in a zero C-H bond order and is observed to have a repulsive PES along both the C-H and C-C bond coordinates. While the second excited state has a small oscillator strength (f = 0.02-0.04), the third excited state is highly allowed: f ranges between 0.6 and 1.1 within the initial Boltzmann geometries.

Figure 4.4 suggests that within the thermally sampled distances, photon energies of 8-11 eV can excite $C_2H_2^{2+}$ to the first excited state, which should weaken the C-C bond. However, the lower energy field frequencies at 9.5 and 10.8 eV do not cause any dissociation of the C-C bond within the Ehrenfest dynamics; only C-H dissociation is observed. This is likely due to the small potential well of the first excited state, which makes the PES not entirely repulsive, thus not allowing for immediate dissociation of the C-C bond.

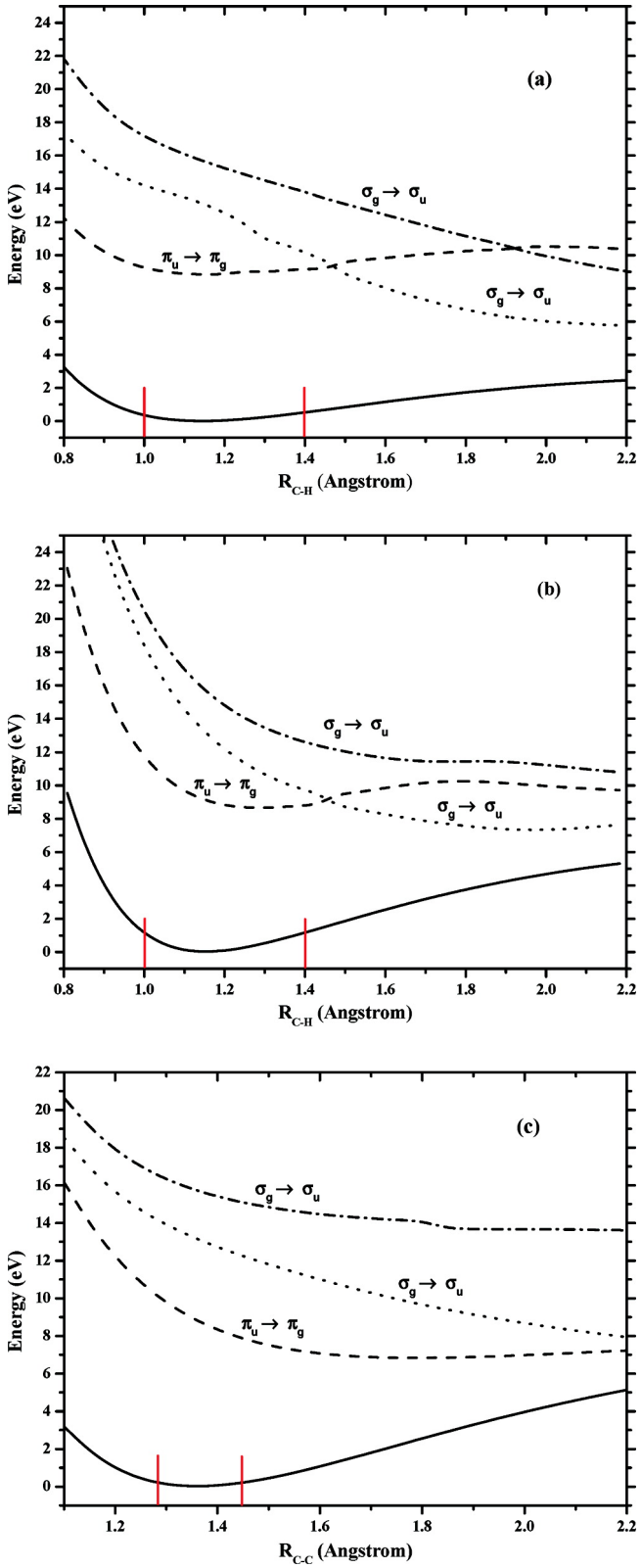

Figure 4.4: Potential energy surfaces for $C_2H_2^{2+}$. Red lines indicate the range of bond lengths within the room temperature Boltzmann distribution: (a) z-allowed states for the asymmetric C-H stretch; one C-H bond is stretched while the other is optimized, (b) z-allowed states for the symmetric C-H stretch; both C-H bonds have the same length, and (c) z-allowed states for the C-C stretch.

While we can rationalize the observance of the C-H dissociation at low photon frequencies of 9.5 and 10.8 eV by realizing that the second excited state becomes energetically available at these photon frequencies at highly stretched C-H distances (see Figure 4.4a and 4.4b), this rationale was surprising initially, considering the relatively small oscillator strength of this state compared to the first excited state. However, the oscillator strength of the second excited state is still greater than the fourth xy-allowed state that caused dissociation with the 13.6 eV field in the xy direction. It appears that in addition to requiring a non-minimal oscillator strength (f>0.01), dissociation dynamics also prefers the shape of the PES to be repulsive, so that direct dissociation can occur. Thus, at these lower energy frequencies, it is the repulsive nature of PES that determines the dynamics, rather than the magnitude of the oscillator strength.

An additional question in understanding the Ehrenfest dynamics results is why single C-H bond breakage (pathway 2) dominates double C-H bond breakage (pathway 3) at the lowest photon energy. Close scrutiny of the symmetric and asymmetric C-H PESs shows that the second excited state, which we have shown is responsible for the dissociation dynamics at these lower energies, dips to slightly lower energies for the antisymmetric stretching of the C-H bond, compared to the symmetric stretching. We see that this selectivity for single C-H dissociation is suppressed by increasing the photon energy. This result agrees well with our phase analysis of initial conditions in which asymmetric stretch is slightly more probable than the symmetric stretch.

Going to even higher photon energies at 12.2 and 13.6 eV shows that favoring of single C-H bond breakage (pathway 2) over double C-H bond breakage (pathway 3) decreases as the system acquires more energy. Overall, a greater percentage of C-H dissociation is observed, which is likely due to $C_2H_2^{2+}$ now having enough energy to access the highly allowed and repulsive third excited state. In addition, some complete

dissociation is seen, including the C-C bond. This indicates that the extra energy of the field allows the system to overcome the potential barrier seen in the PES of the first excited state, allowing for complete, direct dissociation of all bonds.

4.5 Results and Discussion: NO^+ Simulation

In order to study the role of pulse length in the laser control mechanism, a linearly polarized and spatially homogeneous light pulse was applied for interaction time periods, ranging from 20 to 100 fs. The light polarization, within the dipole approximation (eq 4.10), is aligned with the molecular axis. After the laser field is turned off, the simulation continues until t = 150 fs. At the end of the simulation, the N-O bond is considered broken if the distance between atoms exceeds $3\mathring{A}$.

In the previous section, we have shown that the probability of laser control of molecular reaction strongly depends on the oscillator strength of the electronic transition. For polarizations perpendicular to the NO^+ molecular axis, the lower lying electronic transitions are only weakly allowed (oscillator strength f < 0.02) and the PESs are attractive in nature. Therefore, in this study we only focus on situations where the laser polarization is aligned with the molecular axis. Figures 4.5a shows several PESs for lowest dipole-allowed electronic transitions along the molecular axis, obtained with linear response TDDFT. Figure 4.5b shows the same set of PESs computed with a static electric field of E = 0.05 au within the perturbative linear response theory. Although the electronic system in such an electronic field is beyond the perturbative regime, the PES obtained still can provide some insights into the control mechanism. The lowest energy excited state corresponds to the $\pi \rightarrow \pi^*$ electronic transition. Although the PES of this excited state is slightly attractive, the oscillator strength of the excitation is very large (f$\sim$0.7), making it a good candidate as the target doorway state, which provides possibilities to access higher lying excited states

via sequential photon absorption process. As shown in Figure 4.5a, within the Boltzmann sampled bond lengths, this doorway state is accessible with a resonant photon frequency of $\omega = 0.60$ au (16.3 eV), and, therefore, we choose this frequency of light in the following simulations. Because Figure 4.5b indicates that application of a static external field of E = 0.05 au significantly changes the characteristics of the PES, real-time electronic-molecular dynamics is needed to provide a better understanding of laser control.

Figure 4.6 schematically shows snapshots of the time-dependent charge density distribution taken from one representative laser-controlled dissociative reaction. Time-dependent charge density is defined as, $\Delta\rho(t) = \rho(t) - \rho_0(t)$, where $\rho(t)$ and $\rho_0(t)$ are TDDFT and ground state electron densities at time t. Blue and yellow coded surfaces represent electron populating and depopulating regions, respectively, as compared to the ground state configuration. At t = 0, the electron wave function starts in the ground state. As the field is turned on, electrons are driven into the excited state while the bonding orbital gradually loses electron populations. At t = 50 fs, most of the electrons in the bonding orbital are excited to high-lying molecular orbitals, and the molecule starts to dissociate during the period of 50-75 fs. At t = 100 fs, the N and O atoms are already well separated, with the oxygen atom gaining electrons during the dissociative process.

Since the TDDFT Ehrenfest dynamics is a mean-field theory, atomic and molecular properties represent average values even at the asymptotic dissociation limit. Nevertheless, a qualitative understanding of the laser-controlled dissociative charge state can be obtained from analyzing the charge distribution at the end of the dynamics. For example, if the nitrogen atom formed at the point of dissociation has a majority of the positive charge, we then assign the dynamics to the: $O + N^+$ channel. The same approach can be applied to the $O^+ + N$ channel. Figure 4.7 shows prob-

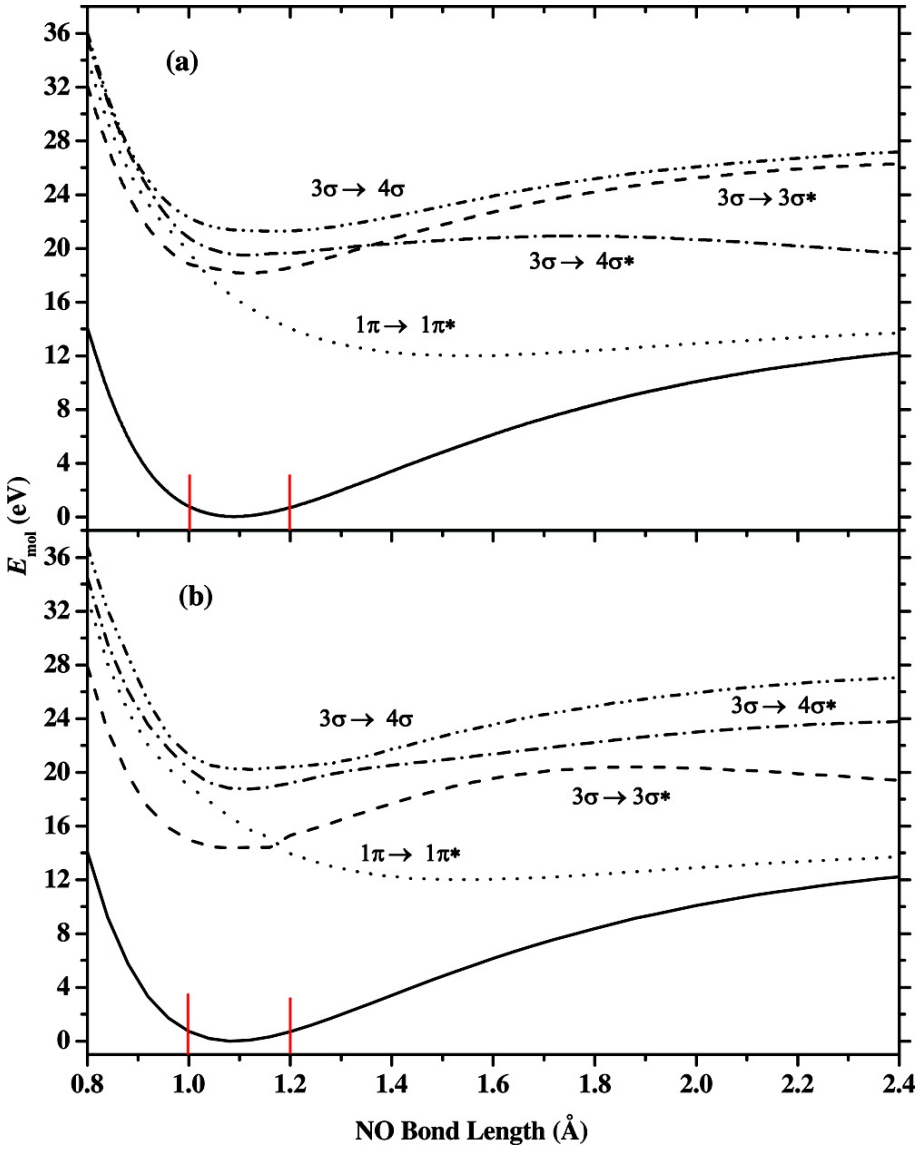

Figure 4.5: Lowest electric-dipole allowed transitions: (a) field-free PES and (b) field-dressed PES with a static electric field of E = 0.05 au applied along the molecular axis. Red lines indicate the range of bond lengths within the room temperature Boltzmann distribution. The $\pi \rightarrow \pi^*$ transition has an oscillator strength of 0.7.

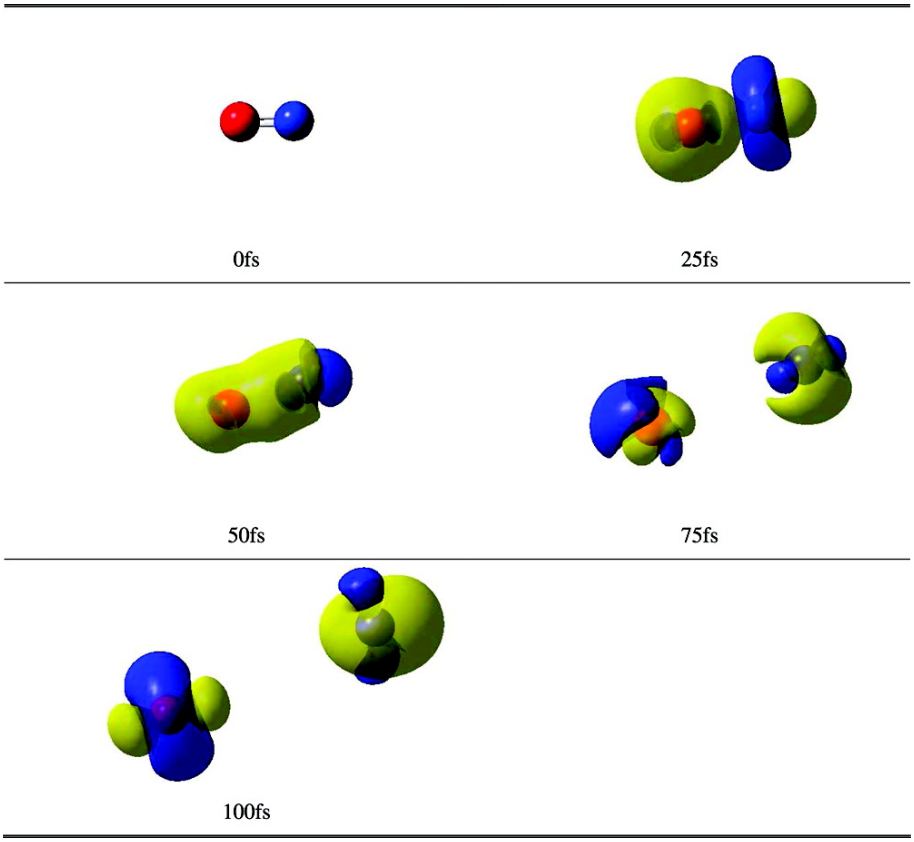

Figure 4.6: Snapshots of charge density distribution at t = 0, 25, 50, 75, and 100 fs. Blue and yellow coded areas represent negative and positive charge distributions, respectively. Relative charge distributions at the end of the trajectories are used to identify dissociative reaction channels.

abilities of nondissociative and dissociative reactions on different dissociative charge states as a function of excitation laser pulse length. The laser field is aligned along the molecular axis with $E_max = 0.05$ au ($\sim 9 \times 10^{13} W/cm^2$), $\omega = 0.6$ au. Five different pulse lengths are investigated with respect to the laser control mechanism. With short laser pulses (<40 fs), nondissociative reactions account for >98% of the product. For dissociation reactions, the probabilities for $N^+ + O$ and $N + O^+$ channels are dependent on pulse length. As the pulse length increases, the probability of observing dissociative reactions of NO^+ also increases, from 0% with a 20 fs pulse to 52% with a 100 fs pulse. The probability for forming the $O + N^+$ channel is approximately twice as likely as the $O^+ + N$ channel for dissociative reactions at all pulse durations. Although this observation presents an interesting target for the control of desired dissociation products with tailored pulse length, the mechanism of this effect remains to be clarified. Figure 4.8 shows time-dependent total energies of the reaction sys-

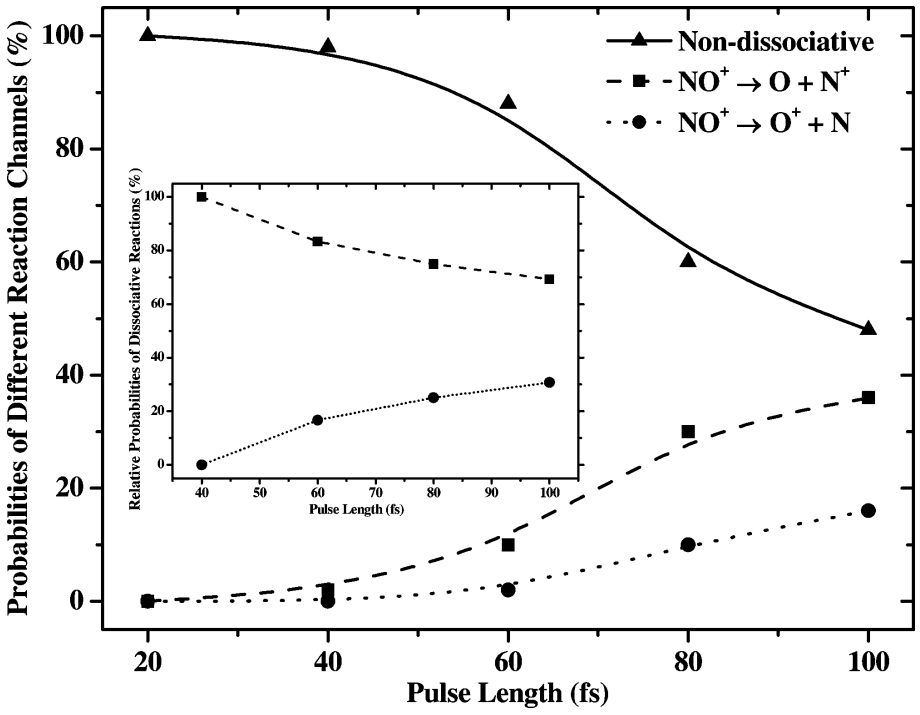

Figure 4.7: Probabilities of dissociative charge states of NO^+ as a function of applied pulse length.

tem itself from three representative electron-molecule Ehrenfest dynamics simulations with a 60 fs pulse. The total energy, calculated using eq 4.11, includes âĂIJon-the-flyâĂİ molecular kinetic energy, the electronic energy using the instantaneous electron density, and the electron-field coupling within the dipole approximation. The large stepwise jumps in energy clearly indicate electronic excitations upon absorption of resonant photons. The vibrational time period of NO^+ is 14.3 fs, suggesting that the time-delay between excitations is modulated by molecular vibrations as the resonant excitation has to coincide with the time-dependent potential energy gap. If the initial vibrational condition does not give rise to resonant absorption, it will take some period of time before the molecule vibrates to a certain position that can lead to resonant absorption. The smaller amplitude oscillations during the time evolution are important characteristics of adiabatic electron dynamics on a given dressed potential surface. These oscillations are faster than the fundamental molecular vibration, but slower than the external driving field. Simple Rabi oscillation model can be used to understand this phenomenon. From linear response TDDFT calculations, the transition dipole moment for excitation from the ground state to the doorway excited state is 0.61 au. With laser field parameters used in this work, the fundamental Rabi frequency is calculated to be 0.05 au (2.9 fs in time period). This frequency agrees with those smaller oscillations in Figure 4.8. As the dynamics moves away from the resonant region after a large stepwise jump, the Rabi oscillation amplitude slightly decreases as expected.

By identifying the number of jumps in the energy time-evolution during the simulation, multiple photoabsorption processes can be analyzed. As a result, the observed excitations can be thought of as sequential multiple single-photon processes as plotted in Figure 4.9. Within a 20 fs pulse, the molecule can only undergo 1.4 vibrational cycles ($\nu = 2328.3 cm^{-1}$), therefore the resonant one and two single-photon processes

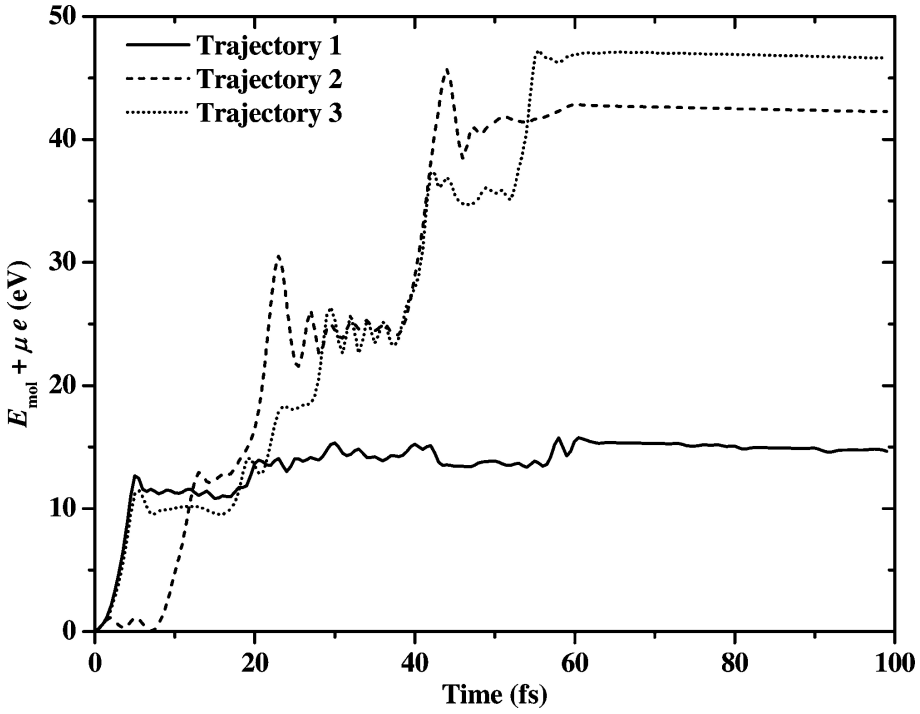

Figure 4.8: Total energy of the molecule (E_{mol}) plus the electric-dipole coupling ($\mu \cdot e$) as a function of reaction time for three select trajectories with a 60 fs laser pulse, $\omega = 0.60$ au, $E_{max} = 0.05$ au ($\sim 9 \times 10^{13} W/cm^2$).

dominate. However, as indicated in Figure 4.5b, the Stark-shifted or strong-field dressed lower lying PESs are mostly attractive potentials. Our simulations also suggest that the probability of observing dissociation with a 20 fs pulse is rather small for the NO^+ molecule. As the laser pulse length increases, the molecule is able to undergo more vibrational cycles and undergo multiple resonant excitations. There thus exists an optimal pulse length associated with the maximum probability of a certain multiple single-photon process. For example, the probability of absorption of two photons is highest with a 40 fs pulse, whereas the three photon process dominates with a 60-80 fs pulse. This relationship between multiple single-photon processes and laser pulse length can be used to explain the observed laser control pattern in Figure 4.7. As indicated from the molecular orbital (MO) density of states (DOS) plot in Figure 4.10, most lower-lying (from -15 to 0 eV) empty MOs show more positive

charge built-up on N than on O, indicating a higher probability to access the $N^+ + O$ channel for lower energy excited states. On the other hand, there are a significant number of MOs that correspond to the $N + O^+$ dissociation channel among higher energy (>0 eV) empty MOs. As the pulse length increases, probabilities of multiple single-photon processes increase and the probability of accessing higher energy PESs also increases. As a result, the likelihood of the dissociative products coming from the $N + O^+$ channel increases with longer pulse lengths. This analysis provides an important control mechanism for the fundamental photoabsorption processes with a controlled laser pulse length. Because the method used in this work is constrained

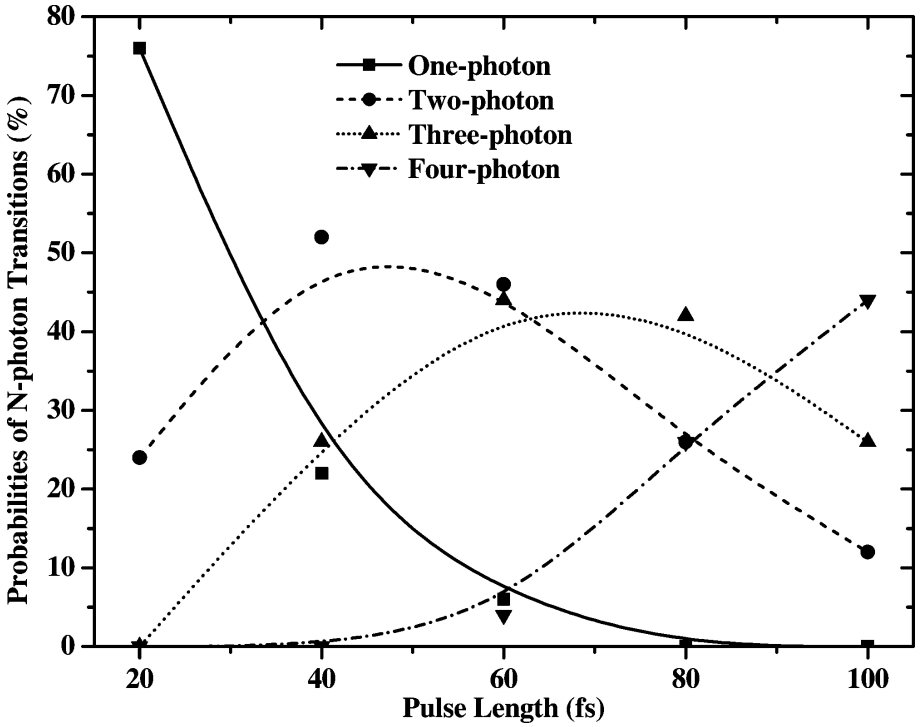

Figure 4.9: Probabilities of sequential multiple photon absorption processes as a function of laser pulse length.

within a single Slater determinant, proper symmetry-adapted singlet excited states cannot be obtained during the dynamics. Excitations observed in this work correspond to simultaneous spin-up and spin-down two-electron transitions.[44] As a result,

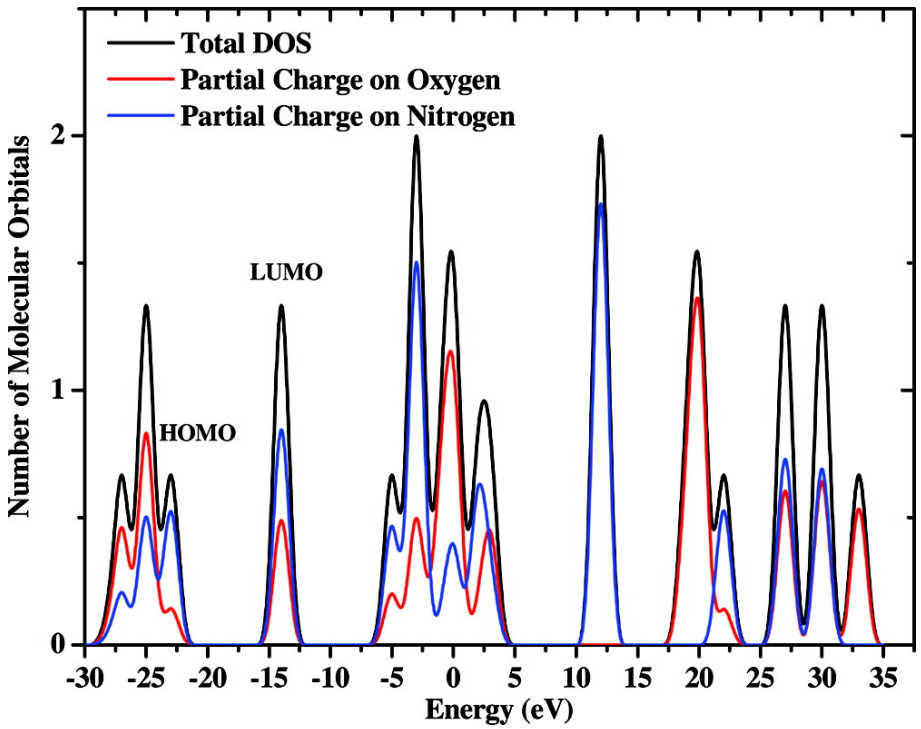

Figure 4.10: Density of state plot of molecular orbitals of the ground state NO^+. Partial charges on N and O are plotted as colored lines. In the lower energy regime (-15 to 0 eV), most MOs are related to the $N^+ + O$ channel, whereas higher energy (>0 eV) MOs see higher probability to access the $N + O^+$ dissociation channel.

the multiple single-photon processes as discussed above apply simultaneously to both spin-up and spin-down electrons and are below the double ionization potential. With the external field used in this paper, the Keldysh parameter[98] is calculated to be 27, suggesting possible multiphoton ionization. However, even with the 100 fs pulse, we did observe energies that were close to or above the double ionization potential of NO^+. This work introduces a mechanism of using laser pulse length to control photoabsorption probabilities. Although the intensity of the field is important for simultaneous multiphoton absorption processes, theoretical observations herein show that sequential single-photon processes can be controlled with tailored pulse length.

Chapter 5

OBTAINING HARTREE-FOCK AND DENSITY FUNCTIONAL THEORY DOUBLY EXCITED STATES WITH CAR-PARRINELLO DENSITY MATRIX SEARCH

The accurate calculation of doubly excited states presents a great theoretical challenge. The standard, very common single configuration excited state linear response methodologies, such as configuration interaction singles (CIS), time dependent Hartree-Fock (TDHF), and the commonly used adiabatic functional approximations in time-dependent density functional theory (TDDFT), are only capable of modeling singly excited states.[99–102] Multiconfigurational methods that use multiple determinants to create doubly excited state wave functions are often too expensive to use on systems of practical interest, such as quantum dots or molecules with extended conjugated π-systems. For example, the doubly excited 2^1A_g state of linear polyenes has been an area of theoretical and experimental study since the early 1970s;[103–110] this state is thought to play a key role in the photophysics of transferring energy from carotenoids to chlorophylls in photosynthesis.[111] While linear response single determinant TDHF and TDDFT methods have been used to study excitations in this and many other extended conjugated systems,[107] much work shows that these methods neglect double and higher excitations.[99–102]

On the other hand, extensions of linear response TDHF/TDDFT to quadratic response theory show that doubly excited states occur incorrectly at sums of the energies of singly excited states.[112] Recent developments in other research groups also show that energies for doubly excited states can be greatly improved with a

dressed/frequency-dependent TDDFT treatment that includes doubly excited determinants. [113, 114] However, there must be a priori knowledge of the energies of the doubly excited states, and electronic wave functions or density distributions cannot be obtained easily with this method. Thus, most calculations of doubly excited states[44, 109] instead use multireference configuration interaction (CI) methods, such as complete active space self-consistent field (CASSCF) or symmetry adapted cluster-CI (SAC-CI).[115, 116] Because precise knowledge of excited states is of crucial importance in determining mechanisms of many photochemical processes, a computational inexpensive method for calculation of doubly excited states is needed.

Our previous work showed that while doubly excited states are absent in linear response TDHF and adiabatic approximation TDDFT methods, resonant excitation within real-time TDHF and TDDFT gives rise to mixing with doubly excited reference states, and can be used to obtain the doubly excited state electron density, yielding energies and other properties.[44] However, this method requires an extensive numerical search for the resonant perturbation frequency, and a stationary state of the Hamiltonian is not guaranteed. In our recent work, we presented a wave function optimization method based on a Car-Parrinello density matrix search (CP-DMS) with first-principles fictitious mass,[3] which shows very fast and smooth convergence behavior. In this paper, we combine these two developments into a novel technique that can obtain not only energies, but also the electron densities of doubly excited states within a single determinant framework. Having the electronic density, in addition to the energy, is of great importance in obtaining insights into the character of a doubly excited state, as it is necessary in order to calculate properties such as dipole moments. We use the real-time TDHF/TDDFT unitary transformation technique to excite the system to an approximate guess of the doubly excited state electron density. We then use our CP-DMS method to converge the density to the nearest closed-shell

stationary state. In this chapter, we first describe our new method and then apply it to two and multielectron molecules: H_2, HeH^+, LiH, ethylene, and butadiene. The method converges to the desired doubly excited state in all test cases.

5.1 Dampened velocity Car-Parrinello density matrix search (CP-DMS)

The details of the CP-DMS method have been discussed in Chapter 3.1 previously, and we only provide a brief review here. The DMS algorithm is formulated in an orthonormal basis. Transformations from an atomic orbital (AO) basis to an orthonormal basis can be done using the Löwdin[54] or Cholesky[55] methods. In an orthonormal basis, the extended Lagrangian[56] for an electronic system gives rise to the Euler-Lagrange equation(eq 3.2,3.3) for the propagation of the density using the principle of stationary action, integrated with the velocity-Verlet algorithm. In the context of searching for a self-consistent stationary point of the electronic wave function, we use a dampened velocity method where the electronic translational kinetic energy is dampened at each integration step,

$$\mathbf{P}_{i+1} = \mathbf{P}_i - \frac{\Delta t^2}{2} m^{-1} \left[\left. \frac{\partial \mathbf{E}(\mathbf{R}, \mathbf{P})}{\partial \mathbf{P}} \right|_{i,\mathbf{R}} + \mathbf{\Lambda}_i \mathbf{P}_i + \mathbf{P}_i \mathbf{\Lambda}_i - \mathbf{\Lambda}_i \right] \tag{5.1}$$

When m is a constant scalar, eq 5.1 has a form similar to the steepest decent approach. In eq 5.1, we used a complete dampening scheme, in which the density matrix velocity is set to zero, to ensure fast convergence.

5.2 Local quantum harmonic oscillators

In most CP or atom-centered density matrix propagation applications, equations 3.2,3.3,5.1 describe the equation of motion of the overall electronic system. However, as shown previously,[3] a uniform effective mass scheme for the whole electronic system does not fully take into account the inhomogeneity of electron density distribution,

and therefore, converges the electronic wave function to a stationary point much slower than conventional SCF approaches. In our current and previous works, we introduce the concept of a local equation of motion for a finite electron density, $\delta\rho(r)$. The dampened velocity CP-DMS method described above is used to propagate $\delta\rho(r)$ with a "tuned" effective mass. As the potential that any given electron density, $\delta\rho(r)$, experiences is quadratic with respect to electron density, the overall electronic system can then be thought as a collection of local harmonic oscillators, or the local drude model. In the AO basis, we define the local electronic density as the density matrix element, $P_{\mu\nu}$, where μ, ν are indices for the orthonormal atomic basis. As a result, eq 5.1 becomes

$$P^*_{i+1,\mu\nu} = P_{i,\mu\nu} - m^{-1}_{\mu\nu}\left[\left.\frac{\partial \mathbf{E}(\mathbf{R},\mathbf{P})}{\partial \mathbf{P}}\right|_{i,\mathbf{R}}\right] \tag{5.2}$$

The Lagrangian constraint is dropped from eq 5.2, and will be enforced directly by an iterative procedure. The gradient term is a modified Li-Nunes-Vanderbilt functional,[57]

$$\left.\frac{\partial \mathbf{E}(\mathbf{R},\mathbf{P})}{\partial \mathbf{P}}\right|_{\mathbf{R}} = 3\mathbf{FP} + 3\mathbf{PF} - 2\mathbf{FP}^2 - 2\mathbf{PFP} - 2\mathbf{P^2F} \tag{5.3}$$

The solution of the quantum mechanical harmonic oscillator can be used to obtain the local effective mass for the local harmonic oscillator oscillating at $P\mu\nu$,

$$m_{\mu\nu} = \frac{k_{\mu\nu}}{\omega^2_{\mu\nu}} \tag{5.4}$$

where k is the force constant and ω is the fundamental frequency associated with local electronic element. The necessary force constants can be approximated from the diagonal elements of the Hessian matrix, which can be calculated directly from the density and Fock/Kohn-Sham matrices,[36, 37]

$$\begin{aligned} k_{\mu\nu} \approx H_{\mu\nu,\mu\nu} &= (3 - 2P_{\mu\mu})F_{\nu\nu} + (3 - 2P_{\nu\nu})F_{\mu\mu} \\ &-2(\mathbf{PF})_{\mu\mu} - 2(\mathbf{PF})_{\nu\nu} - 2(\mathbf{FP})_{\nu\nu} - 2(\mathbf{FP})_{\nu\nu} \end{aligned} \tag{5.5}$$

Note that equation above is a simple approximation to the rank-2 Hessian using some elements from the rank-4 Hessian tensor without computationally expensive two-electron integrals. The fundamental frequency for each density element is given by

$$\omega_{\mu\nu} = \frac{\varepsilon_{\mu\nu}}{\hbar} = \mathbf{F}_{\mu\nu}\mathbf{P}_{\nu\mu} \tag{5.6}$$

This local harmonic oscillator model gives rise to a local effective mass scheme that takes into account the inhomogeneity of the electron distribution.

5.3 Lagrangian constraint and zero point reference

As an alternative to explicitly calculating the Lagrangian constraint, the conservation of the number of electrons and idempotency of the density matrix are maintained by a simple scaling followed by McWeeny purifications (eq 3.11)[62]

As in standard electronic structure theory, the frequency in eq 5.6 is using the atomic heat of formation as the zero point reference, which leads to a negative frequency for electrons. In order to effectively use this fictitious mass scheme, we introduce an arbitrary zero point frequency ω_0 so that all electron elements have positive frequencies. We also introduce a cutoff frequency ω_{core} so that only active electron elements are taken into account in the first principles fictitious mass scheme,

$$m_{\mu\nu} = \begin{cases} \omega_0 & if \quad \omega_{\mu\nu} \leq \omega_{core} \\ \frac{k_{\mu\nu}}{(\omega_0+\omega_{\mu\nu}-\omega_{core})^2} & if \quad \omega_{\mu\nu} > \omega_{core} \end{cases} \tag{5.7}$$

5.4 Unitary transformation real-time TDHF/TDDFT to propagate the electron density

To prepare appropriate initial guesses of electron density distributions for excited states, we use a high intensity field with real-time TDHF/TDDFT approach.[44] A modified midpoint unitary transformation propagator,[59] constructed from the

eigenvectors $\mathbf{C}(t_k)$ and eigenvalues $\varepsilon(t_k)$ of the Fock/Kohn-Sham matrix, is used to evolve the time-dependent density,

$$\begin{aligned}
\mathbf{P}(t_{k+1}) &= \mathbf{U}(t_k) \cdot \mathbf{P}(t_{k-1}) \cdot \mathbf{U}^{\dagger}(t_k) \\
\varepsilon(t_k) &= \mathbf{C}^{\dagger}(t_k) \cdot \mathbf{K}(t_k) \cdot \mathbf{C}(t_k) \\
\mathbf{U}(t_k) &= \mathbf{C}(t_k) \cdot exp\left[i \cdot \Delta t_e \cdot \varepsilon(t_k)\right] \cdot C^{\dagger}(t_k)
\end{aligned} \tag{5.8}$$

where Δt_e is the time step for the integrator. In the current work, we use a linearly polarized and spatially homogeneous external field of frequency ω and maximum field strength E_{max},

$$e(t) \approx E_{max} sin(\omega \cdot t) \tag{5.9}$$

The instantaneous electron-field interaction is introduced into the Hamiltonian through the electric-dipole approximation,

$$\mathbf{K}(t) = \mathbf{K}_0(t) + \mathbf{d} \cdot e(t) \tag{5.10}$$

where $\mathbf{K}_0$ is the field-free Fock/Kohn-Sham matrix, and $d_{\mu\nu} = \langle \chi_\mu | \, r \, | \chi_\nu \rangle$ is the dipole integral in the AO basis.

In this work our Hamiltonians for propagation are either the HF Hamiltonian or standard ground state DFT functionals within the adiabatic approximation. The same Hamiltonian is used to calculate the energy based on the CP-DMS converged density, using the ground state equilibrium geometry. To be clear, we are not using the DFT functional to calculate the excited Kohn-Sham states, but instead to propagate and then to calculate the energy for a given electronic density. Developing new DFT functionals for excited state propagation and energies is beyond the scope of this work, but were the exact functional known that related the density to the true energy of the system (either ground or excited), convergence would lead to the true density of the doubly excited state, and the true energy of the system could be calculated.

5.5 Numerical Tests and Discussion

Calculations were carried out using the development version of the GAUSSIAN series of programs (ref 35) with the addition of the real-time TDHF/TDDFT and CP-DMS algorithms presented here. In the following, we use an effective zero point frequency of ω_0 = 5.0 a.u., and a cutoff of ω_{core} = -5.0 a.u. for core and valence electrons. This set of parameters has been tested extensively and consistently shows excellent computational speed and SCF convergence.[3] Using CP-DMS//TDHF or CP-DMS//TDDFT, we implement the following procedure to obtain the doubly excited states: (1) to generate an approximate doubly excited state, a linearly polarized continuous wave light pulse is applied as a perturbation to the molecular system initially in its ground state equilibrium geometry, driving electrons into potential wells of higher excited states using the unitary transformation propagator (eqs 5.8-5.10); (2) when the external field is turned off, the CP-DMS approach (Sec. 5.1) is then applied to converge the wave function to the nearest closed-shell single determinant stationary state; and (3) the energy of the excited state is obtained using the converged electron density and adiabatic ground state exchange-correlation kernel. For all test cases, final electronic wave functions are converged with the root-mean-square (rms) gradient (eq 5.3) less than 5×10^{-4} a.u. It is important to note that the true excited state energy requires an exact exchange-correlation kernel for excited states. However, searching for such functionals is beyond the scope of this chapter, and the excited state energies obtained are only approximations within the framework of the adiabatic ground state kernel. Excitation energies obtained correspond to vertical excitations from the ground state equilibrium geometries. he frequency and maximum amplitude of the field are ω = 0.1-1.0 a.u., and E_{max} = 0.10-0.50 a.u. Different sets of field parameters are chosen for different systems to generate a strong perturbation to drive electrons to excited states.

Figure 5.1 shows the CP-DMS//TDHF results for H2, modeled with the minimal STO-3G basis to limit the number of excited states to S1 (singly excited) and S2 (doubly excited) for a clear understanding of the behavior of the method introduced here. We remove the field at two different times, at t = 13.4 and t = 19.1 a.u. The shorter length pulse does not perturb the electron density far enough away from the ground state, and the CP-DMS method converges the density back to the original ground state, as seen by the population of the antibonding σ^* orbital (Figure 5.1a) returning to the initial zero value. The longer pulse length continues to drive the electron density, and CP-DMS converges this electron density into the doubly excited S_2 state which, in this case, corresponds to double occupation of the antibonding σ^* orbital. Figure 5.1b shows that with the external field turned on, the rms gradient (eq 5.3) increases from less than 10^{-12} a.u. when the system is in the initial ground state to a maximum of 0.29 a.u. when 0.72 electrons occupy the σ bonding orbital. If the external field continues to drive the electronic density into σ^*, the rms gradient (eq 5.3) starts to decrease as electrons are driven into the electronic potential well of the S_2 state. For electron densities in this region, CP-DMS is able to converge the wave function to the S_2 state of the electronic system. Figure 5.1c shows the energy as the system returns to the initial ground state, and as it is converged to the S_2 state. At the convergence of the S_2 state, the $S_0 \rightarrow S_2$ energy gap is calculated to be 1.596 a.u. at the HF level, in agreement with that obtained with real-time dynamics.[44]

As we showed in earlier work,[117] simultaneous two-electron excitation can be achieved by tuning the external field to resonance. The electron density of the S_2 state can then be obtained as the density that yields the smallest amplitude of residual dipole oscillation. The advantage of combining CP-DMS//TDHF with the previous real-time dynamics method is that CP-DMS does not require a precise resonant field to be applicable. It is also not necessary to examine the amplitude of the oscillation of

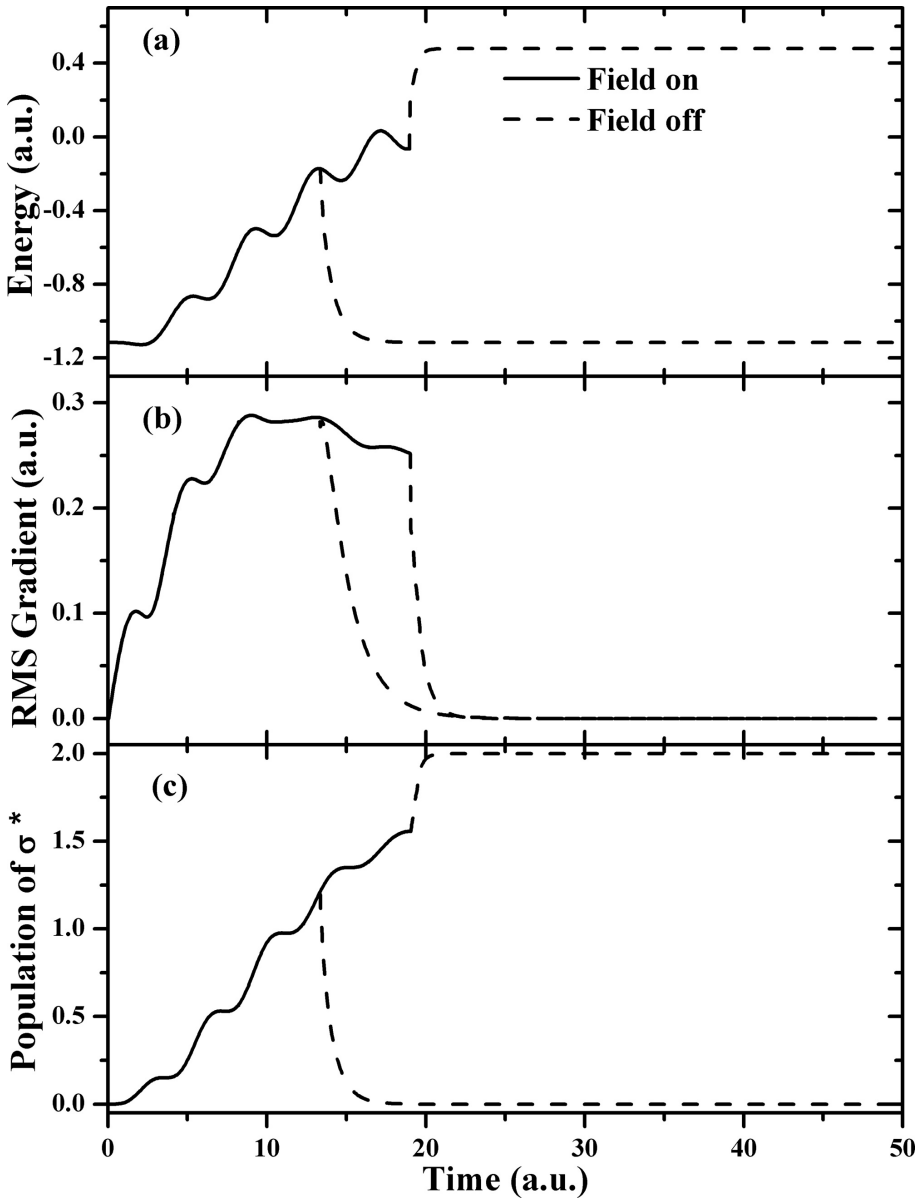

Figure 5.1: (a) Energy and (b) rms gradient of energy with respect to the density (eq 5.3), and (c) population of σ^* orbital (in atomic units) during the time-evolution of electrons in H_2 calculated with CP-DMS//TDHF/STO-3G. $\omega = 0.75$ a.u., $E_{max} = 0.2$ a.u.

the residual dipole at a variety of electron densities. We simply converge the density to the nearest stationary state once we have a reasonable guess to the doubly excited state electron density.

Table 5.1: Excitation energies (in atomic units) of doubly excited electronic states computed with CP-DMS//TDHF/STO-3G. Relevant full CI results are shown for comparison.

			LiH		
Method	H_2	HeH^+	$\sigma \rightarrow p_x, p_y$	$\sigma \rightarrow p_z$	$\sigma \rightarrow \sigma^*$
HF	1.596	2.157	0.668	0.871	1.091
B3LYP	1.520	2.151	0.645	0.812	1.017
PBE	1.492	2.141	0.637	0.807	0.992
Full CI	1.637	2.166	0.670	0.900	1.141

We show in Table 5.1 the H_2 minimal basis doubly excited state energy gaps for HF, B3LYP, and Perdew-Burke-Ernzerhof (PBE) methods using CP-DMS after the real-time propagation. We also give the full CI results for comparison. As noted in ref [44], these energies are not twice the singly excited state energies as is predicted from quadratic response theory. The HF results are in better agreement with the CI results because the CI wave function is dominated by a single HF configuration. The standard DFT functionals drastically underestimate the energy of the S_2 state, mainly due to the fact that the adiabatic exchange-correlation kernels are tuned to produce ground state electronic densities and energies.

Also given in Table 5.1 are the doubly excited state energy gaps for minimal basis HeH^+ and LiH. HeH^+ is a broken symmetry analog of H_2, also with two orbitals and two electrons, and only one possible doubly excited state. The four-electron LiH is more complicated because double electron excitations can occur either into the empty σ^* orbital, or into the empty p orbitals on Li. By tuning the field polarization, we are able to selectively excite electrons into doubly excited states of interest. In the

case of LiH, when the field is perpendicular to the molecular axis, excitations into the degenerate p_x/p_y orbitals can be obtained as indicated in Figure 5.2a. On the other hand, a parallel field with respect to the molecular axis gives rise to excitations into the σ^* antibonding orbital and the s-p_z hybridized empty orbital (Figure 5.2b and c). For two-electron two-orbital systems, such as H_2 and HeH^+ with a minimal basis, the necessary length of laser pulse for exciting electrons into the potential well of the doubly excited state can be chosen by simply monitoring the population in the antibonding orbital. When multiple (>2) orbitals and multiple (>2) electrons are involved in the laser induced excitation process, choosing the laser pulse length for the desired double excitation becomes more difficult. In the current work, we chose to stop the laser field when we observed a "cleanâĂİ double excitation, one in which only the target orbitals showed significant population change. For example, in Figure 5.2c, even though the σ and σ^* orbitals show a near population inversion at t$\sim$10 a.u., other molecular orbitals are also involved in the excitation. Therefore, electron density at this moment does not give rise to the desired $\sigma \rightarrow \sigma^*$ double excitation. A clean $\sigma \rightarrow \sigma^*$ transition is observed at t$\sim$37 a.u., and the electron density is used to obtain the doubly excited state. As Table 5.1 shows, the HF energy gaps for LiH again are much closer to the CI energy gaps than those obtained with B3LYP and PBE. As the σ^* electron is more correlated with other electrons in the system than the localized p electron, the lack of correlation in HF likely leads to more significant error in the $\sigma \rightarrow \sigma^*$ transition, compared to the full CI results.

While for symmetric H_2, the HF and DFT doubly excited states have both electrons in σ^*, this is generally not the case for other systems. For example, for minimal basis HeH^+, the final population of σ^* is 1.928e (HF), 1.897e (B3LYP), and 1.883e (PBE), and for LiH, the final population of the p_x/p_y orbital in the first of the doubly excited states is 1.923e (HF), 1.485e (B3LYP), and 1.529e (PBE).

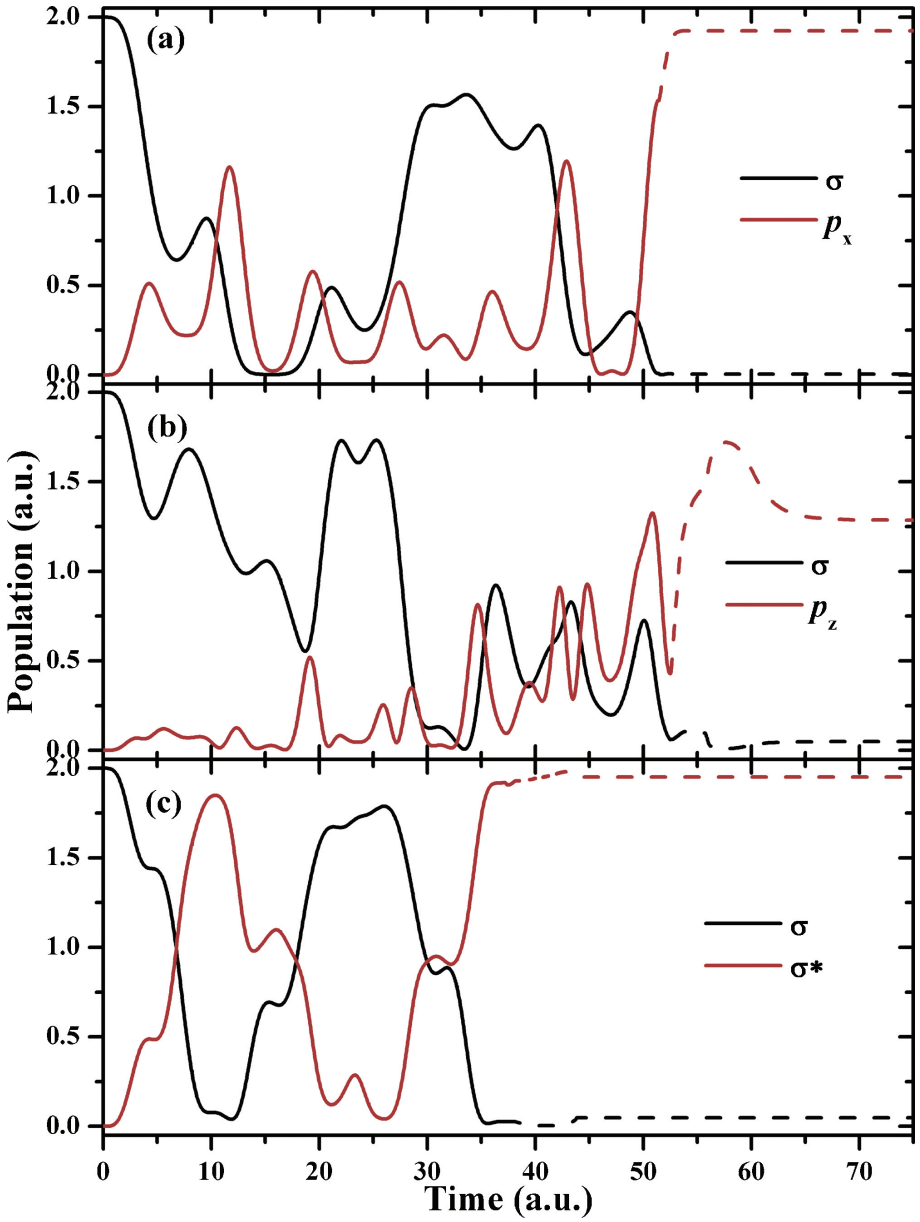

Figure 5.2: Electron orbital populations for LiH using CP-DMS//TDHF/STO-3G: (a) laser field aligned perpendicular to the molecular axis, $\omega = 0.4$ a.u., $E_{max} = 0.3$ a.u., (b) laser field aligned parallel to the molecular axis, $\omega = 0.4$ a.u., $E_{max} = 0.5$ a.u., and (c) laser field aligned parallel to the molecular axis, $\omega = 0.6$ a.u., $E_{max} = 0.4$ a.u. Solid line indicates field on, and dashed line indicates field off.

To further demonstrate the robustness of this promising approach for obtaining doubly excited states, we also examined the $\pi \rightarrow \pi^*$ double excitation of ethylene and butadiene, shown in Table 5.2, using a variety of basis sets. Although the relative

Table 5.2: Excitation energy (in atomic units) and corresponding π^* final electron populations for $1^1A_g \rightarrow 2^1A_g$ transition of ethylene and butadiene.

Molecule	Method	$\Delta E(1^1A_g 2^1A_g)$	π^* population
Ethylene	CASSCF(12,12)/STO-3G	0.670	
	SAC-CI/STO-3G	0.589	
	CP-DMS//TDHF/STO-3G	0.656	2.000
	CP-DMS//TDHF/3-21G	0.566	1.996
	CP-DMS//TDHF/6-31G*	0.516	1.891
	CP-DMS//TDHF/6-31G**	0.509	1.855
	CP-DMS//TDHF/6-31+G**	0.505	0.904
Butadiene	CASSCF(4,4)/STO-3G	0.309	
	SAC-CI/STO-3G	0.323	
	CP-DMS//TDHF/STO-3G	0.425	1.334
	CP-DMS//TDHF/6-31G*	0.327	1.291
	CP-DMS//TDHF/6-31+G**	0.308	0.810

position of the doubly excited 2^1A_g state of all-trans polyenes has been an interesting topic and the subject of much research,[110] it is not the focus of this study. For both ethylene and butadiene, the CP-DMS method is able to find the doubly excited 2^1A_g state, which has dominantly doubly occupied π^* character. This is shown for butadiene in Figure 5.3, using the STO-3G and 6-31G* basis sets. However, adding diffuse functions to the basis set leads to complicated mixings of $\pi \rightarrow \pi^*$ with other transitions, and a $\pi \rightarrow \pi^*$ doubly excited state for the 6-31+G** basis was not found. We could not easily perform full CI calculations on ethylene and butadiene, and in-

stead used truncated multiconfigurational methods with a minimal basis. Therefore, for comparison with the CP-DMS results, included in Table 5.2 are energies for a (12,12) CASSCF calculation of ethylene, correlating all noncore electrons and orbitals, a (4,4) CASSCF calculation of butadiene, correlating the π system, and also calculations using the SAC-CI general-R method, which includes excitations through sextuples within the valence space. The double excitation energies obtained using the CP-DMS//TDHF method are again in very good agreement with the multiconfigurational methods.

In addition to obtaining doubly excited state energies and properties, an interesting point that we can address with this work is the character of the closed shell single Slater determinant excited states, that is, whether they are minima, maxima, or saddle points in the potential energy landscape. The determination is made by evaluating the electronic Hessian, which reflects the characteristics of the local electronic potential energy landscape. A minimum or a maximum would yield all positive or negative values, respectively, while a saddle point would give both positive and negative values. For the special case of H_2 using the minimal basis, all elements in the Hessian matrix for the two-electron excited state are negative, indicating the doubly excited state is a maximum in the electronic potential energy landscape for this system. There is a single positive Hessian value for HeH^+ on the diagonal element for the hydrogen atom. This indicates that additional charge build up on hydrogen would cause an increase in the overall energy of the system, whereas other charge distributions would decrease the energy. For the other doubly excited states studied herein, which are generally the low-lying doubly excited states, the Hessian matrix always has multiple negative values, with the number of negative values varying from one to ten, and the number of positive values greatly outweighing the negative. For ethene, the larger basis sets yield doubly excited state Hessians with fewer negative values than the smaller basis,

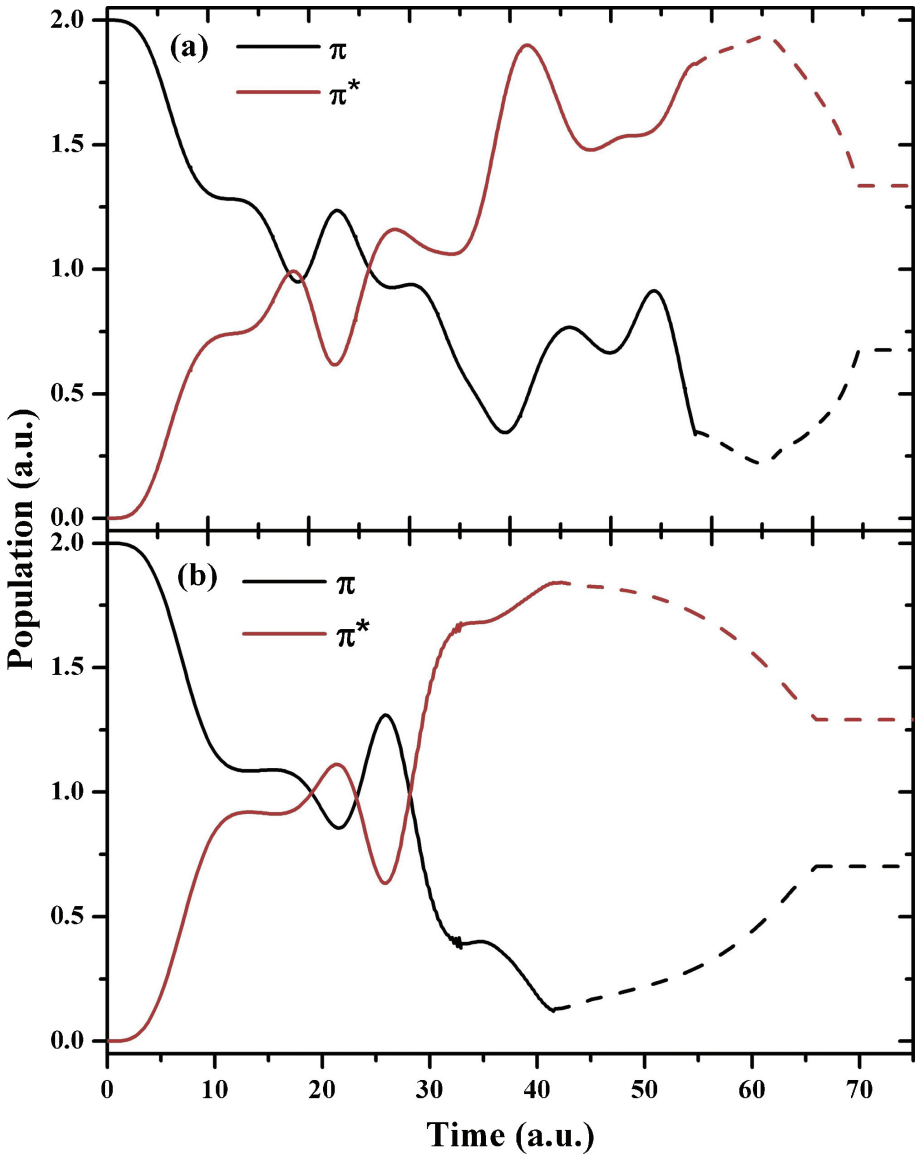

Figure 5.3: Electron orbital populations for butadiene using CP-DMS//TDHF with (a) STO-3G, $\omega = 0.2$ a.u., $E_{max} = 0.1$ a.u. and (b) 6-31G*, $\omega = 0.17$ a.u., $E_{max} = 0.1$ a.u.

but for butadiene we find that the larger basis set gives more negative values. Thus, there does not appear to be a systematic dependence on the size of the basis set for the lower lying doubly excited states studied here. Because the general case includes both negative and positive Hessian values, the doubly excited states within a single Slater determinant are saddle points on the potential energy landscape.

Chapter 6

ULTRAFAST SOLVATED ELECTRONIC DYNAMICS USING TIME-DEPENDENT DENSITY FUNCTIONAL THEORY AND POLARIZABLE CONTINUUM MODEL

The most direct way to describe the composite solute-solvent system is to explicitly include solvent molecules and evaluate the state of the system by means of molecular mechanics (MM),[118, 119] quantum mechanics (QM), or a combination thereof.[120–122]

In such cases, the time dependence of the solvent polarization is obtained explicitly from the simulated trajectories in solute-solvent molecular dynamics (MD). A less computationally demanding and more flexible approach uses the implicit solvation model. In this model the polarization is determined by the dielectric function of the solvent, described as a continuous medium in which a cavity hosts the solute. Continuum models developed to treat the time-dependent solvation response can be generally categorized into two main classes. The first introduces a separation of the solvent polarization into a dynamical contribution described by the optical dielectric constant, associated with the solute's electronic motion, and an inertial or orientational contribution, related to its nuclear motion and the bulk dielectric permittivity.[123–126] The response of the solvent is described in terms of these two contributions, and typically the dynamical component is assumed to equilibrate instantaneously to the final state in the presence of the inertial part of the polarization, while the orientational component of the polarization remains in equilibrium with the charge density of the initial state. On the other hand models of the second class

implicitly consider dynamical and inertial effects in a single response,[127–130] as the transition is represented as a step-like change in the solute charge density, and the solvent response is modeled by introducing the complex dielectric permittivity as a function of the frequency.

In order to include solvent effects within solute ultrafast electronic dynamics the method presented herein employs a polarizable continuum model and is developed according to the following strategy: the solvent electronic response is treated as a dynamical quantity, whose change comes instantaneously as a result of motion in the electronic degrees of freedom of the solute molecule. We incorporate a continuum representation of the solvent within the polarizable continuum model (PCM)[131, 132] to the real-time time-dependent density functional theory (RT-TDDFT) approach,[90] following the principle that the solvent effect is added as solvent reaction field to the total system Hamiltonian,

$$\hat{H}(t) = \hat{H}_0(t) + \hat{V}_{PCM}(t) \tag{6.1}$$

where $\mathbf{H}_0$ represents the solute Hamiltonian and $\mathbf{V}_{PCM}$ is the solvent reaction potential. The PCM method allows a realistic representation of the cavity in which the solute is embedded as well as a quantum mechanical description of the solute and proves to be an excellent tool in describing the effects of solvation on molecular phenomena and the resultant properties.

In this chapter, we introduce solvent effects into first-principles electronic dynamics by inclusion of the PCM method within RT-TDDFT electronic dynamics simulations. Our primary interest is on the description of the solvent effect on temporal evolution after sudden changes in the solute charge distribution. We first describe the theoretical methodologies used to propagate the solvated electronic structure of a molecular system. Next, we apply our scheme to the optically active organic molecule *para*-nitroaniline (pNA) and present the results for discussion.

6.1 Propagation of the Nonperturbative TDDFT Equation

We propagate the electronic degrees of freedom with a modified midpoint and unitary transformation method (MMUT), while enforcing a stationary nuclear configuration (see ref [90] for detailed machinery and algorithm), according to the TDDFT equation in an orthonormal basis (using atomic units)

$$i\frac{d\mathbf{P}'}{dt} = \mathbf{K}'\mathbf{P}' - \mathbf{P}'\mathbf{K}' \tag{6.2}$$

where **P**' and **K**' are density and Kohn-Sham matrices. Transformations from an atomic orbital (AO) basis (**P** and **K**) to an orthonormal basis (**P**' and **K**') can be achieved using the Löwdin[54] or Cholesky[55] methods. The time-dependent Kohn-Sham matrix **K** corresponds to the effective Hamiltonian in eq 6.1, and its form will be discussed in Section 6.2. Because the PCM reaction potential is included in the description of the effective Hamiltonian, the TDDFT equation (eq 6.2) gives rise to the solvated electronic dynamics driven by the interplay between the solvent and solute. Note that the PCM reaction potential is implicitly time-dependent as a result of the time-dependent electron density **P** of the solute, as discussed in Section 6.2. The unitary transformation matrix is a time-evolution operator constructed from the eigenvectors $\mathbf{C}(t_k)$ and eigenvalues $\varepsilon(t_k)$ of the Fock/Kohn-Sham matrix,

$$\varepsilon(t_k) = \mathbf{C}^{\dagger}(t_k) \cdot \mathbf{K}'(t_k) \cdot \mathbf{C}(t_k) \tag{6.3}$$

$$\mathbf{U}(t_k) = \mathbf{C}(t_k) \cdot exp\left[i \cdot 2\Delta t_e \cdot \varepsilon(t_k)\right] \cdot C^{\dagger}(t_k) \tag{6.4}$$

where Δt_e is the time step for the MMUT integrator. The density matrix is then propagated from time t_{k1} to t_{k+1} with a fixed nuclear position

$$\mathbf{P}'(t_{k+1}) = \mathbf{U}(t_k) \cdot \mathbf{P}'(t_{k-1}) \cdot \mathbf{U}^{\dagger}(t_k) \tag{6.5}$$

Equations 6.3-6.5 are used to propagate the electron density in the space of all atomic orbitals with time-reversibility. We have demonstrated in our previous publications

that this nonperturbative TDDFT approach is capable of describing both electronic dynamics in the strongly coherent regime and nonadiabatic phenomenon.[9, 76, 133–135]

6.2 PCM Formalism with RT-TDDFT

The PCM model approximates the solvent as a continuous dielectric medium with an embedded cavity that hosts the solute. The solute-solvent interaction is obtained by solving the Poisson equation with the appropriate boundary conditions and expressed as a quantum mechanical self-consistent reaction field (SCRF). Such a reaction field can be represented by an apparent surface charge (ASC) density placed on the surface of the cavity. The ASC density can be determined using a variety of methods depending on which model of the PCM family is being implemented. Practical applications of all PCM methods also require a discrete representation of the ASC density over the solute-solvent interface. The integral equation formalism PCM (IEF-PCM)[136–139] and the continuous surface charge (CSC) formalism[140] are used in this work, but the implementation to RT-TDDFT can be generalized to any discrete charge formalism. In the CSC method, the ASC density is defined over all space and represented in a basis of spherical Gaussian functions ϕ with the polarization charges q as the expansion coefficients.

$$\sigma(\mathbf{r}) = \sum_i \frac{q_i}{a_i} \phi_i(\mathbf{r}; \mathbf{s}_i, \zeta_i)) \tag{6.6}$$

where a_i is the area of the i-th surface elements, q_i is the corresponding expansion coefficients of the ASC (i.e. the polarization charges), and $\mathbf{s}_i$ is the representative point of the i-th surface element. If the electronic wave function of the solute is expanded in a set of atomic orbital (AO) basis χ, the electrostatic potential V_i acting

on the solvent, with a Gaussian ansatz for ϕ_i, can be expressed as (in atomic units),

$$V_i(t) = \sum_A \int \frac{Z_A \phi_i(\mathbf{r})}{|\mathbf{r} - \mathbf{R}_A|} d^3\mathbf{r} - \sum_{\mu\nu} P_{\mu\nu}(t) \int \int \frac{\phi_i(\mathbf{r}) \chi_\mu(\mathbf{r}') \chi_\nu(\mathbf{r}')}{|\mathbf{r} - \mathbf{r}'|} d^3\mathbf{r} d^3\mathbf{r}' \tag{6.7}$$

where Z_A and $\mathbf{R}_A$ are nuclear charge and position and $\mathbf{P}$ is the electronic density matrix (see ref [140] for detailed derivations) of the solute. As indicated in eq 6.7, for fixed nuclear coordinates, the time-dependence of the electrostatic potential comes from the time-dependent electronic degrees of freedom, propagated by the RT-TDDFT method introduced in the previous section.

In the current implementation, we model the solvent electronic response to the ultrafast time-dependent electrostatic potential induced by the solute electronic dynamics. The solvent electronic response is ultrafast and instantaneous; that is, the solvent electronic distribution is always in equilibrium with respect to $\mathbf{V}(t)$, while the orientational component of the polarization remains in equilibrium with the charge density of the initial state of the solute. Note that nuclear and molecular orientational response, which takes place on a much longer time scale than the characteristic time for appreciable motion in the solvent electronic degrees of freedom, requires additional components in the continuum model to explicitly account for such phenomena, and is not considered in this work. Current implementation focuses on the ultrafast electronic response of the solvent. With the time-dependent electrostatic potential defined in eq 6.7, solvent dynamical electronic response can be simulated within any of the continuum models. As a result, the equilibrium state of solvent polarization charges can be obtained by solving the discretized PCM model self-consistently[141, 142] with the given solute electrostatic potential $\mathbf{V}$ at time t and the solvent optical dielectric permittivity.

On the other hand, the PCM modeled solvent drives the electronic density of the solute via the solute-solvent coupled Kohn-Sham operator and an effective solvent

reaction potential $\mathbf{V}^{PCM}$

$$\mathbf{K} = \mathbf{h} + \mathbf{G}[\mathbf{P}] + \alpha \cdot E_{xc}[\mathbf{P}] + \mathbf{V}^{PCM} \tag{6.8}$$

$$V_{\mu\nu}^{PCM} = \sum_i \int \int \frac{q_i \phi_i(\mathbf{r}) \chi_m u(\mathbf{r}') \chi_n v(\mathbf{r}')}{|\mathbf{r} - \mathbf{r}'|} d^3\mathbf{r} d^3\mathbf{r}' \tag{6.9}$$

where $\mathbf{h}$ is the core-Hamiltonian matrix and $\mathbf{G}$ is the two-electron integral matrix including the Coulomb term and exchange term in the case of Hartree-Fock. E_{xc} is the DFT exchange-correlation contribution to the Hamiltonian with $\alpha = 0$ for Hartree-Fock and $\alpha = 1$ for DFT. For hybrid functionals Exc take on fractional DFT exchange and correlation parts along with fractional Hartree-Fock exchange. Equation 6.8 includes the PCM reaction potential optimized with a given solute electronic density. It is this reaction potential that in turn drives the electronic dynamics of the solute.

6.3 Time-Dependent Electric Polarization

In order to investigate the interplays between solvent and solute electronic dynamics, modeled by PCM and RT-TDDFT, respectively, the time-evolution of solvent and solute polarizations will be analyzed. The time-dependent electronic polarization of the composite system can be evaluated as

$$\mathbf{D}(t) = \int \mathbf{r} \rho(\mathbf{r}, t) d^3 \tag{6.10}$$

where $\rho(\mathbf{r}, t)$ is the total charge density and D(t) describes the polarization response to all orders. Similar to the static polarization expansion, the extension of the time-dependent polarization response can be expressed as[143]

$$\mathbf{D}_i(t) = D_i^0 + D_{ij}^{(1)}(t)\mathbf{E}_j + D_{ijk}^{(2)}(t)\mathbf{E}_j\mathbf{E}_k + \cdots 2 \tag{6.11}$$

$$D_{ij}^{(1)}(t) = \int dt_1 \alpha_{ij}(t - t_1) F_j(t_1) \tag{6.12}$$

$$D_{ijk}^{(2)}(t) = \int dt_1 \int dt_2 \beta_{ijk}(t - t_1, t - t_2) F_j(t_1) F_k(t_2) \tag{6.13}$$

Here $i, j, k \equiv x, y, z$ denote the Cartesian axes, and summations are implicit for repeated indices. $F(t)$ is the temporal envelope of the electric field $\mathbf{E}$, and $\alpha(t)$ and $\beta(t)$ are the time-dependent polarizability and the first hyperpolarizability, respectively. By applying the convolution theorem to eq 6.12, we can obtain the usual frequency-dependent polarization, whose first order term is related to the linear absorption spectrum,

$$D_{ij}^{(1)}(\omega) = \alpha_{ij}^{(1)}(\omega) F(\omega) \tag{6.14}$$

The imaginary part of the frequency dependent polarizability $\alpha(\omega)$ directly relates to the transition dipole strength $S(\omega)$ or absorption cross section $\sigma(\omega)$[144]

$$Tr\left[Im\alpha(\omega)\right] = \frac{\pi}{2\omega} S(\omega) \propto \frac{\sigma(\omega)}{\omega} \tag{6.15}$$

where $Tr[\ldots 2]$ denotes the trace.

6.4 Numerical Tests on pNA

Calculations were carried out on a Dell PowerEdge R610 Server (dual quad-core 2.4 GHz Intel Xeon with 16GB of RAM), using the development version of the GAUSSIAN series of programs(35) with the addition of the PCM solvated real-time TDDFT (PCM-RT-TDDFT) approach presented here. The total energy conservation of the system is maintained within 0.5 kcal/mol. The following describes the computational setup to model the ultrafast solvent and solute electronic response:

- The initial solute ground state geometry and wave function are fully optimized with or without an external static field.

- The initial solvent PCM polarization charge distribution is resolved self-consistently using the solvent bulk dielectric constant (ε= 2.271 for benzene), which in principle addresses solvent nuclear and electronic relaxations.

- The ultrafast electronic dynamics starts at t = 0 and is initiated by photoexcitation or removal of the external static field. Solute electronic density and solvent PCM reaction potential are propagated according to the scheme described above. Because we are modeling the interplays of solvent and solute electronic degrees of freedom, the solvent optical dielectric permittivity ε_∞ (ε_∞= 2.253 for benzene) is used in the PCM model.

- The ultrafast time-resolved polarizations are analyzed using the method presented in Section 6.3.

Excited State Charge Transfer Dynamics The charge transfer dynamics in a pNA molecule (Figure 6.1) is employed as a test, and dynamical phenomena are compared in vacuo and benzene solution. The small pNA molecule is one of the first organic electro-optic molecules, and it is also known to have a large hyperpolarizability induced by the HOMO→LUMO intramolecular donor-acceptor charge-transfer (CT) process.[145–147] The hybrid density functional B3LYP[148, 149] with the 6-31G(d) basis set is applied to both optimizations of chromophore structures and electronic dynamics simulations. The initial electronic CT state of the pNA molecule at t = 0 is prepared by means of a Koopmans' excitation, manifested through swapping the occupation of HOMO and LUMO orbitals of the ground state both in vacuo and in benzene solution. The charge transfer dynamics are simulated in both environments for 48 fs.

Figure 6.2a shows the oscillation of the x-component of the time-dependent dipole moment $\mu_x(t)$ of pNA. Apparent dipole enhancement is observed for pNA in benzene over the vacuum case, and the electronic CT state also appears to be more stable in benzene than in vacuo. The amplitude of dipole oscillation is decreased in solution, while the average of μ_x is increased, implying a charge separation that is both larger

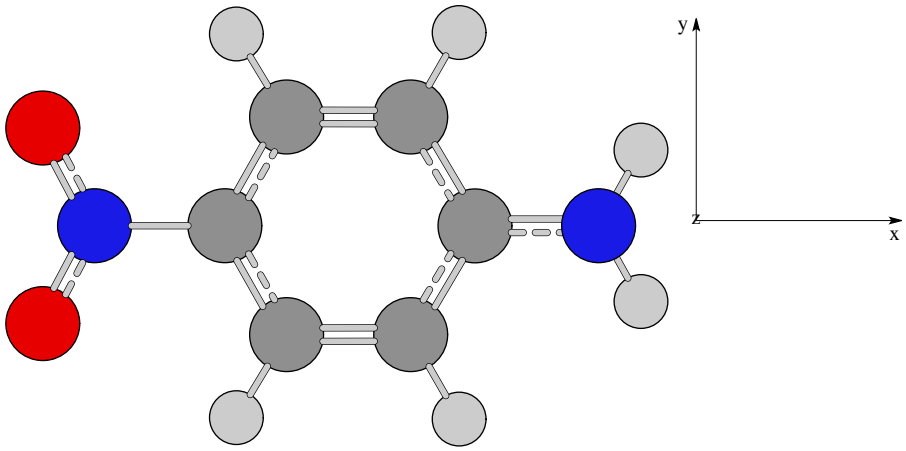

Figure 6.1: Molecular structure of *p*-nitroaniline (pNA), with Cartesian axes. Carbon atoms are shown as dark gray circles, hydrogen as light gray, nitrogen as blue, and oxygen as red.

in magnitude and more stable. Further, this indicates a more significant population in the CT state, which comes about as a result of solvent reorganization, or a downward shift in energy of the CT state. As a result, the energy separation of the ground and excited electronic states is decreased. This is borne out in the Fourier transform (Figure 6.2b) of the time-evolution of dipole in Figure 6.2a. All peaks in benzene solution are red-shifted, due to the stabilization of the CT state. The relative amplitudes in benzene solution are also significantly altered, as the HOMO→LUMO transition in solution leads to an electronic density with a much larger CT character but a smaller transition dipole moment to the ground state. These observations are consistent with experiments.

Absorption Spectrum from Ground State To further prove the validity of our PCM-RT-TDDFT method, we chose to compare the optical absorption spectrum of the pNA molecule obtained using the conventional linear-response TDDFT (LR-TDDFT)[92, 150] and RT-TDDFT approach both in vacuo and in benzene solution. The initial electronic density of the pNA molecule at $t < 0$ is prepared by optimizing

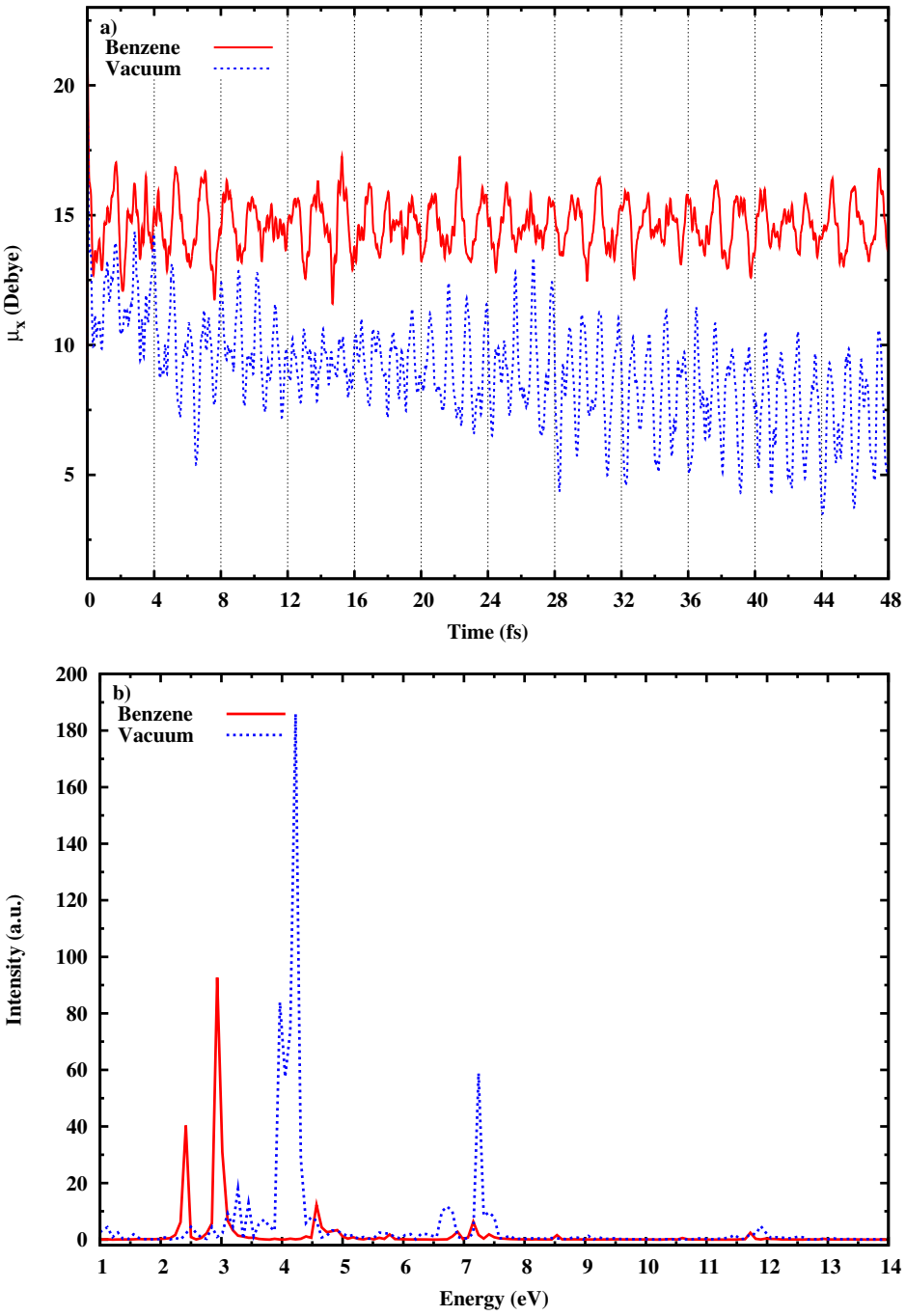

Figure 6.2: (a) Dipole moment oscillation along the x axis for pNA in vacuo (dotted blue line) and benzene (solid red line), following a HOMO→LUMO Koopmans' excitation, and (b) the Fourier transform of these patterns.

the ground state electronic structure in the presence of a small perturbative static electric field $E_0 = 0.001$ au both in vacuo and in solution. The dipole moment of ground state pNA along the molecular axis is slightly higher in benzene (8.3 D) than that in vacuo (7.1 D). The static electric field is able to initialize a small mixing of the ground state with excited states. Such mixing will give rise to a time-dependent dipole oscillation upon removal of the static field. The time-evolution of the dipole can then be used to resolve the ground state absorption spectrum.

At time t = 0, the external field is turned off and the entire electronic system, including solvent, is propagated in real time according to the method introduced in this article. Figure 6.3 illustrates the time-evolution of the polarization in thex-direction for pNA in vacuo and in benzene solution. Figure 6.4a shows the absorption spectrum of the pNA molecule calculated using the formulation presented in Section 6.3 and results in Figure 6.3. Red-shifting of nearly every peak in benzene solution is observed compared to those in vacuo. Large shifts occur for peaks with strong charge-transfer characters located at 4 eV and 7 eV. The vertical absorption spectra obtained using the real-time TDDFT technique is compared to those computed by the linear response TDDFT with PCM[126] (Figure 6.4b). Both techniques use the optical dielectric permittivity of the solvent to address the ultrafast solvent electronic response. While linear response technique is able to compute state-resolved spectra, the advantage of real-time TDDFT lies in the rich dynamical information of solvent-solute inter-responses. Nevertheless, the absorption peak positions and relative intensities are in excellent agreement for the two methods both in vacuo and in solution, reinforcing the accuracy and efficacy of the approach introduced herein.

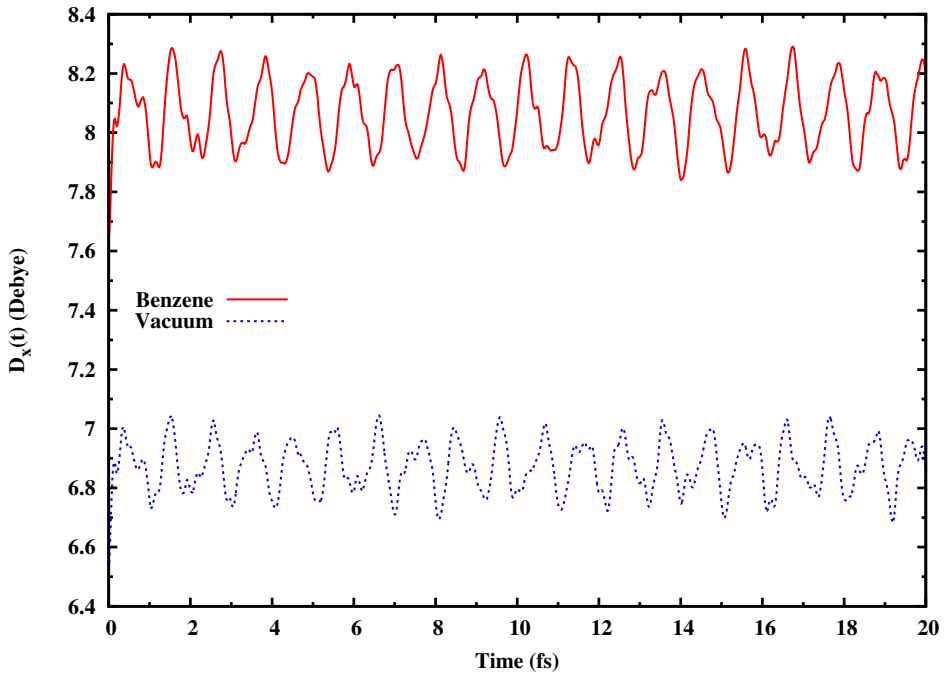

Figure 6.3: Time evolution of the polarization along the x-axis for pNA in vacuo (dotted blue line) and benzene solution (solid red line).

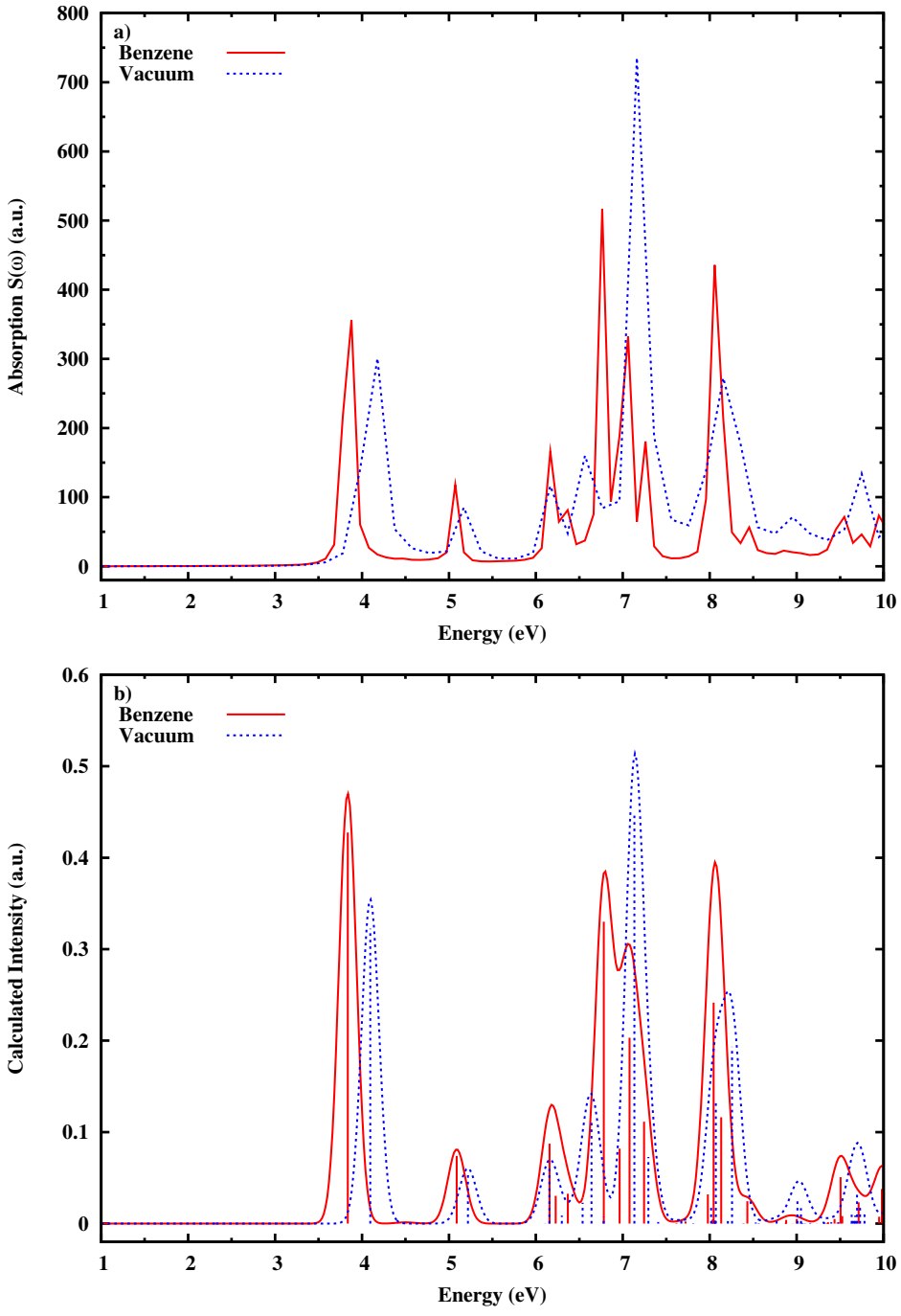

Figure 6.4: Absorption spectrum for pNA obtained using (a) real-time TDDFT method and (b) linear response TDDFT both in vacuo (dotted blue lines) and in benzene (solid red lines). Linear response TDDFT peaks are dressed with Gaussian functions and a broadening parameter of 0.10 eV.

Chapter 7

ULTRAFAST COHERENT ELECTRON-HOLE SEPARATION DYNAMICS IN A FULLERENE DERIVATIVE

The use of fullerene derivatives as electron acceptors in bulk heterojunctions (BHJ) is a promising development in the search for efficient energy conversion in hybrid solar cells.[151, 152] These interesting materials exhibit photoabsorption in the visible range with the additional benefit of having the ability to optimize the molecular packing with a judicious selection of functional groups and coblended polymers.[153] The first step in generating current in a BHJ solar cell that employs these complexes is the creation of a sufficiently long-lived exciton within the donor phase of the active layer. When these photo-generated excitons travel to phase boundaries, the potential gradient at the interface can lead to either hole or electron transfer from the organic phase to the charge carrier phase that is coupled to an electrode. Using appropriate molecular entities in the electron donor and acceptor phases can currently lead to efficiencies greater than 7%.[154]

The migration of an electron to a phase boundary can occur through fullerene-to-fullerene electron transfer or through spatial translation of the coulomb-bound Frenkel exciton. This process must occur on a time scale shorter than that of electron-hole recombination. One way to prevent fast electron-hole recombination is to engineer fullerene derivatives that exhibit intrinsic electron-hole separation through accessible charge-transfer excited states. However, direct excitation to charge transfer excited states is either completely forbidden or only weakly allowed according to the pho-

toabsorption spectra of fullerene derivatives. The solvent-dependent fluorescence decay of C_{60}:DMA (DMA = N,N-diethylamine) suggests the existence of a lower lying ligand-to-fullerene intramolecular electron transfer state that gives rise to a long-lived electron-hole pair.[155, 156] A recent time-dependent density functional theory (TDDFT) study of the absorption cross section of complex supramolecular triads consisting of carotenoid-diaryl-porphyrin-C_{60} also revealed an efficient charge separation pathway following photo-excitation.[157–159] The strong electron-withdrawing fullerenes should make sequestering of an electron either through intra- or intermolecular charge transfer a readily accomplished task. The authors of ref [157] also noted that not all of the effects leading to the charge separation in the final state are fully understood. To aid in a better understanding of the interplay between the photoexcited electron-hole pair and the charge-separated state, we present in this chapter some dynamical aspects of excited state electron-hole separation in a C_{60}:DMA complex (see Figure 7.1) using PCM solvated real-time nonadiabatic nonperturbative TDDFT (PCM-RT-TDDFT) electronic dynamics, as described in the previous chapter.

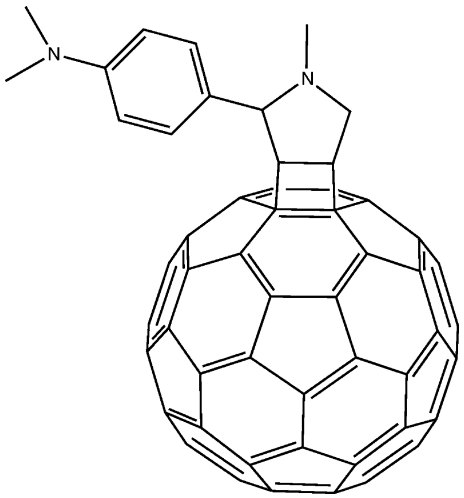

Figure 7.1: 2D representation of C_{60}:DMA.

The exploitation of intramolecular charge transfer in a BHJ active layer has the

advantage of needing only a single molecular species in the electron donor phase, compared to the binary phases utilized in concert with intermolecular transfer from an electronically excited polymer to a fullerene, as is employed in a majority of experimental studies and practical implementations.

7.1 Computational Details

Excited state electronic dynamics beyond the perturbative regime models a coherent electronic wave function in the time-domain. Important dynamics and kinetic information can be obtained through analysis of the coherence between excited states.[134] All calculations, including geometry optimization, absorption spectra, and electronic dynamics were performed using the B3LYP hybrid functional with the all electron basis 6-31G(d) using the development version of the Gaussian suite of programs[52] with the addition of PCM solvated real-time TDDFT dynamics. The computational scheme of excited electronic dynamics is as follows:

- The electronic density that corresponds to an excited state of interest is prepared by promoting an electron from a selected occupied to an unoccupied molecular orbital. This step creates an electron density that is not stationary but represents a coherent wave packet composed of the ground state and excited states of interest.

- The coherent state is propagated using PCM-RT-TDDFT electronic dynamics in both vacuo and methycyclohexane (MCH) solution (ε=2.024). The reason to choose MCH as a representative nonpolar solvent is because of its strong fluorescence quantum yield reported in experimental study,[155, 156] which could potentially enhance the intramolecular charge transfer process.

- The total electron density is projected on the ground state molecular orbital

space and analyzed.

Computational time was significantly reduced using a dynamical active space screening for the electron density, based on incremental Fock/Kohn-Sham builds in the time domain wherein only the contribution to the two-electron integral of portions of the electron density that are perturbed above a predetermined threshold are recalculated at each time step.[5]

The structure of C_{60}:DMA has been previously studied using the semiempirical AM1 theory.[155] In both previous and current studies, the phenyl ring of the aniline is orthogonal to the pyrole that is covalently bonded to the fullerene (Figure 7.1). The relative rotation of these groups leads to a decrease in the overlap of their respective π bonding orbitals, which can affect intramolecular charge transfer rates in a detrimental manner. Figure 7.2 shows the absorption spectrum of C_{60}:DMA computed using the linear response TDDFT in the frequency domain.[93, 101, 160, 161] The strongest absorption in the UV range corresponds to excitations within the DMA ligand, where the relatively small absorption in the visible (inset of Figure 7.2) is a result of photoexcitations of C_{60}. Electron-hole pairs in these states are of strong binding energy because they are localized on the fullerene with a relatively low dielectric constant. In principle, such excited states are relatively short-lived and inefficient electron or hole donor states. On the other hand, the presence of a covalently bound ligand does introduce several lower energy charge-transfer or electron-hole separated states at 1.7-1.8 eV. However, these charge-transfer states are not electric-dipole allowed from the ground state and therefore have zero oscillator strengths. One hypothesis regarding intramolecular charge transfer between ligand and fullerene is that the photoexcited C_{60} or DMA states can couple to the charge-transfer states through a coherent charge-transfer mechanism between excited states. To test this hypothesis, we consider two excitation schemes wherein either a fullerene-fullerene or ligand-

ligand electronic transition is imposed. The former probes the visible region of the absorption spectrum of C_{60}:DMA, while the latter induces molecular transitions in the UV. PCM-RT-TDDFT technique is used to follow the electron density immediately after the photoexcitation.

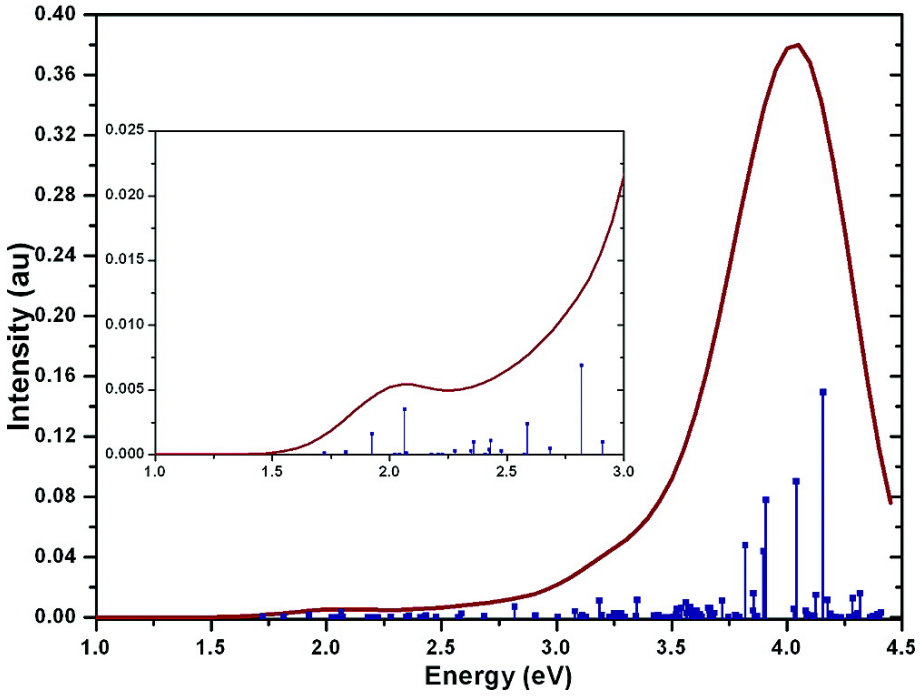

Figure 7.2: Absorption spectrum of C_{60}:DMA. Excitations with nonzero oscillator strength were induced on either the fullerene (visible, inset) or the ligand (UV).

The initial excited state that can be thought of as resulting from photo-excitation by visible light in C_{60}:DMA is prepared by promoting an electron from the second highest occupied molecular orbital (HOMO-1) to the lowest unoccupied molecular orbital (LUMO) to form a photogenerated electron-hole pair. This transition corresponds to the absorption peak at about 1.8 eV in Figure 7.2. These MOs correspond to photogenerated electron and hole localized on C_{60} and an electron localized on the DMA ligand (see MO plots in Figure 7.3). Figure 7.4 shows the time evolution of the orbital occupation numbers for the ground state HOMO-1, LUMO, and HOMO

in vacuo and MCH solution, computed by projecting the instantaneous electronic density onto the initial ground state molecular orbital space. An electron density prepared in this scheme does not correspond to an eigenstate of the Fock/Kohn-Sham matrix, but can be described as a nonequilibrium superposition of eigenstates, which gives rise to the ensuing charge transfer.

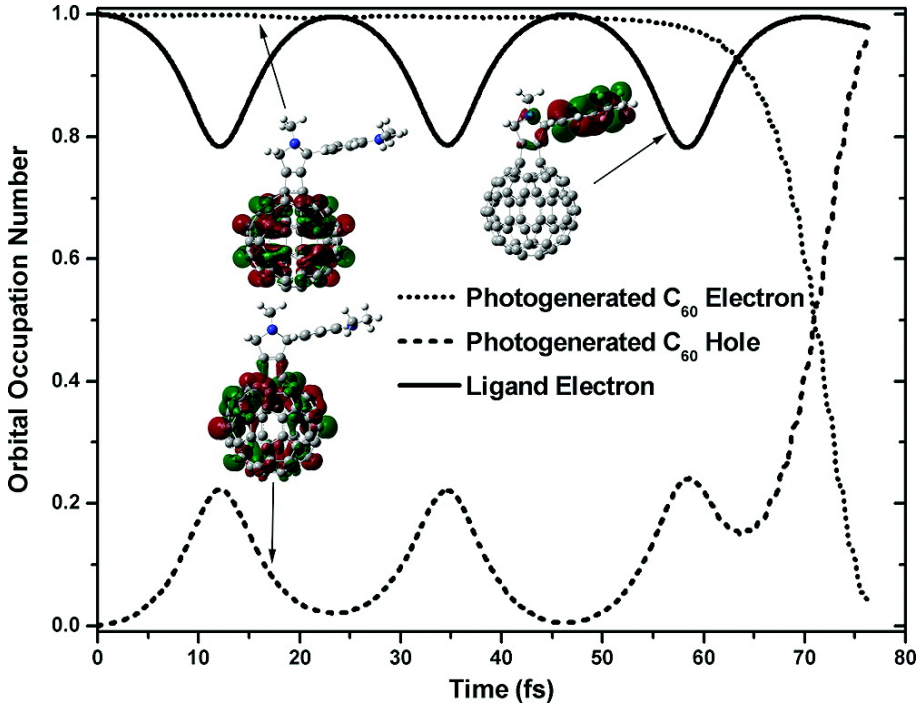

Figure 7.3: Time evolution of the photogenerated electron (LUMO, dotted line) and hole (HOMO-1, dashed line) localized on C_{60}, and an electron localized on the DMA ligand (HOMO, solid line) following a fullerene-localized excitation in vacuo.

7.2 Analysis and Discussion

In Figure 7.4, the electron-hole pair dynamics shows an approximately 22% electron transfer from the ligand (HOMO) to the photogenerated hole in the fullerene (HOMO-1) occurring within the first 12 fs in vacuo, and the transfer percentage seems to be promoted up to 36% in MCH solution within the first 19 fs, as the nonequilibrium

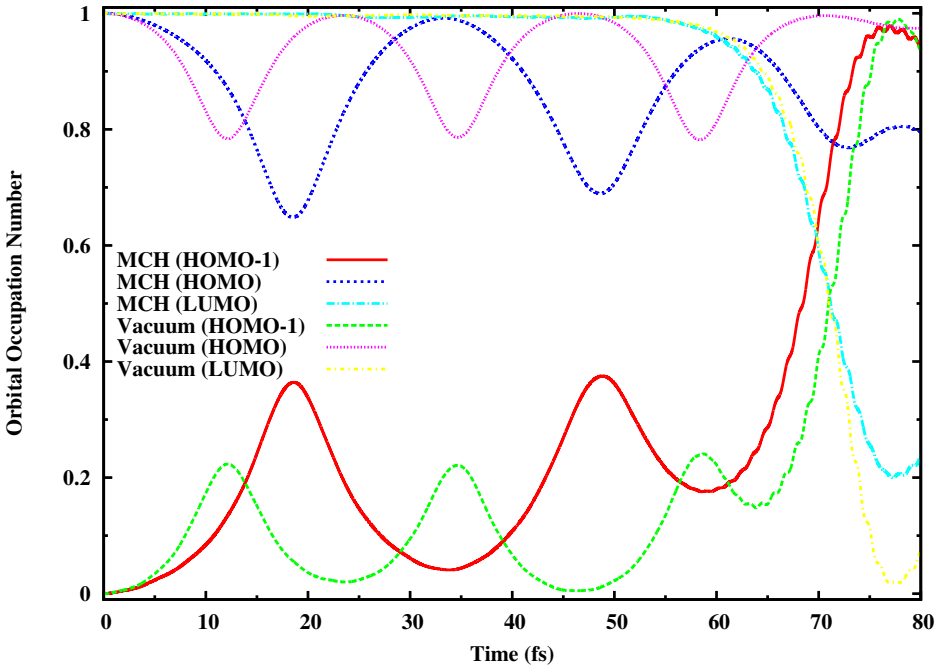

Figure 7.4: Time evolution of the photogenerated electron (LUMO)and hole (HOMO-1) localized on C_{60}, and an electron localized on the DMA ligand (HOMO) following a fullerene-localized excitation.

electron density begins to evolve. In contrast, the photogenerated electron (LUMO) loses no appreciable population while the charge transfer state is being accessed initially. This phenomenon suggests that the transition from photoexcited C_{60} to the charge-transfer state is much stronger than the electron-hole recombination at short times. As the electron density being propagated represents a coherent superposition state, the charge-transfer event does not result in an irreversible transfer of a single electron from the ligand to the fullerene, but results in coherent electronic wavepacket motion, with charge oscillating between the donor and acceptor.

In vacuo

- Analysis of the time-dependent dipole moment of the molecule (Figure 7.5) indicates coherent electronic wavepacket motion with a period of 23 fs, which

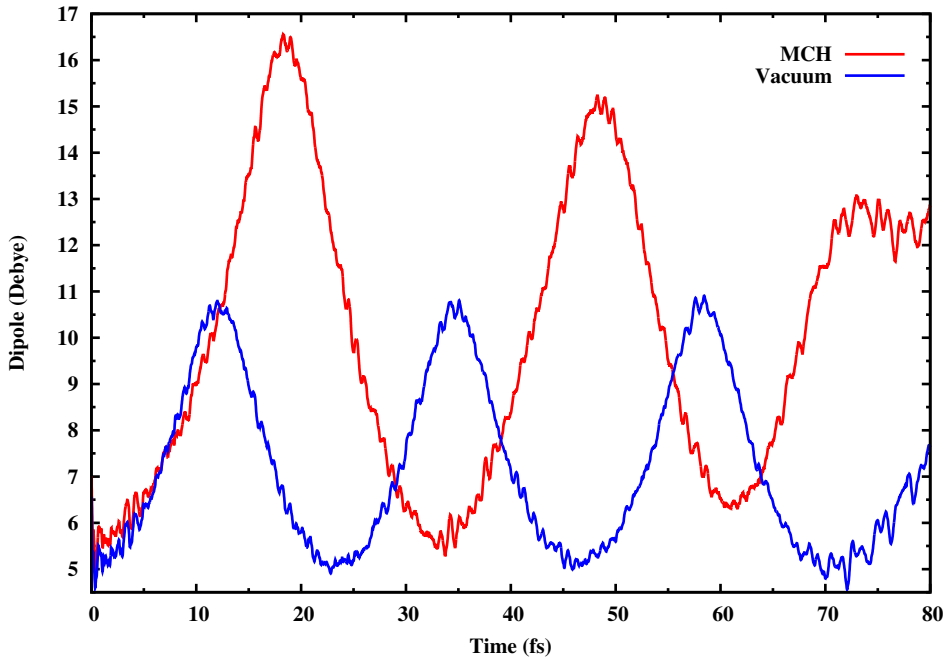

Figure 7.5: Time evolution of the photogenerated electron (LUMO, dotted line) and hole (HOMO-1, dashed line) localized on C_{60}, and an electron localized on the DMA ligand (HOMO, solid line) following a fullerene-localized excitation.

correlates to a frequency consistent with the energy gap of 0.18 eV between the initial state and the charge-transfer state.

- The dipole moment of C_{60}:DMA increases by a factor of 2.5, from 4.33 to 10.79 Debye, in 11.5 fs, also suggesting a strong charge-transfer event.

- This oscillation amplitude persists until the initial photoexcited electron (LUMO) begins to lose population at 50 fs as the initial electron-hole pair recombination starts to compete with the charge-transfer event.

- Since the ligand-to-fullerene charge transfer is in direct competition with electron-hole recombination, a lower limit on the time scale for charge transfer is dictated by recombination; in the present case, this event occurs at approximately 70-75

fs.

In MCH solution

- The coherent electronic wavepacket period starts to be ∼34 fs at beginning, and rather than maintaining a steady propagation the period dramatically decreases down to 25 fs in the follw-up cycle, suggesting a trend for chirping. The average period of 29 fs corresponds to a frequency consistent with the energy gap of 0.14 eV between the initial state and the second lowest charge-transfer state, suggesting apparent alternation of charge-transfer pathway. Such phenomenon is somewhat unexpected and very difficult to obtain with conventional static calculations.

- The dipole moment of C_{60}:DMA increases by a factor of 3.6, from 4.64 to 16.55 Debye, in 18.3 fs, slower compared to vaccum but with a stronger charge-transfer event.

- This oscillation amplitude also persists for 50 fs before the initial electron-hole pair recombination emerges to compete with the charge-transfer event.

- The a lower limit on the time scale for charge transfer is still dictated by recombination and at a even faster pace that takes place at approximately 65-70 fs.

Note that we do not include nuclear motion which can open a relaxation pathway for the otherwise coherent electron density. When nuclear-motion induced decoherence exists, the ultrafast electron-hole pair separation dynamics observed above can become irreversible, leading to long-lived charge separation excited state. Upon careful selection of an appropriate ligand donor that possesses the desired photophysics,

it may be possible to create a covalently bound bridging region that is amenable to a more complete exergonic charge transfer than is presently seen.

BIBLIOGRAPHY

[1] W. Liang, H. Wang, J. Hung, X. Li, and M. J. Frisch, J. Chem. Theory Comput. **6**, 2034 (2010).

[2] W. Liang, C. T. Chapman, M. J. Frisch, and X. Li, J. Chem. Theory Comput. **6**, 3352 (2010).

[3] X. Li, C. L. Moss, W. Liang, and Y. Feng, J. Chem. Phys. **130**, 234115 (2009).

[4] W. Liang, C. M. Isborn, and X. Li, J. Chem. Phys. **131**, 204101 (2009).

[5] W. Liang, C. T. Chapman, and X. Li, J. Chem. Phys. **134**, 184102 (2011).

[6] W. Liang, S. A. Fischer, M. J. Frisch, and X. Li, J. Chem. Theory Comput. **7**, 3540 (2011).

[7] F. Ding, W. Liang, C. T. Chapman, C. M. Isborn, and X. Li, J. Chem. Phys. **135**, 164101 (2011).

[8] C. T. Chapman, W. Liang, and X. Li, J Chem Phys **134**, (2011).

[9] W. Liang, C. M. Isborn, and X. Li, J. Phys. Chem. A **113**, 3463 (2009).

[10] T. Wen, W. Liang, and K. M. Krishnan, J. Appl. Phys. **107**, 09B501 (2010).

[11] J. Hung, W. Liang, J. Luo, Z. Shi, A. K. Y. Jen, and X. Li, J. Phys. Chem. C **114**, 22284 (2010).

[12] W. Liang, C. M. Isborn, A. Lindsay, X. Li, S. M. Smith, and R. J. Levis, J. Phys. Chem. A **114**, 6201 (2010).

[13] Z. Shi, W. Liang, J. Luo, S. Huang, B. M. Polishak, X. Li, T. R. Younkin, B. A. Block, and A. K. Y. Jen, Chem. Mater. **22**, 5601 (2010).

[14] D. H. Bale, B. E. Eichinger, W. Liang, X. Li, L. R. Dalton, B. H. Robinson, and P. J. Reid, J. Phys. Chem. B **115**, 3505 (2011).

[15] W. Liang, X. Li, L. R. Dalton, B. H. Robinson, and B. E. Eichinger, J. Phys. Chem. B **115**, 12566 (2011).

[16] W. Liang, C. T. Chapman, F. Ding, and X. Li, J. Phys. Chem. A **116**, 1884 (2012).

[17] A. Banerjee, N. Adams, J. Simons, and R. Shepard, J. Phys. Chem. **89**, 52 (1985).

[18] J. Simons and J. Nichols, Int. J. Quantum Chem. **24**, 263 (1990).

[19] W. Murray and M. H. Wright, *Practical Optimization* (Academic, New York, 1981).

[20] M. J. D. Powell, *Nonlinear Programing* (Academic, New York, 1970).

[21] J. E. Dennis and R. B. Schnabel, *Numerical Methods for Unconstrained Optimization and Non-linear Equations* (Prentice Hall, New Jersey, 1983).

[22] L. E. Scales, *Introduction to Non-linear Optimization* (Macmillam, Basingstoke, 1985).

[23] R. A. Fletcher and G. Pilcher, Trans. Faraday Soc. **66**, 794 (1970).

[24] D. F. Shanno, Math. Comput. **24**, 647 (1970).

[25] B. A. Murtagh and R. W. H. Sargent, Comp. J. **13**, 185 (1970).

[26] M. J. D. Powell, Math. Program. **1**, 26 (1971).

[27] O. Farkas and H. B. Schlegel, J. Chem. Phys. **111**, 10806 (1999).

[28] J. Baker, J. Comput. Chem. **14**, 1085 (1993).

[29] C. Y. Peng, P. Y. Ayala, H. B. Schlegel, and M. J. Frisch, J. Comput. Chem. **17**, 49 (1996).

[30] P. Pulay and G. Fogarasi, J. Chem. Phys. **96**, 2856 (1992).

[31] C. A. White and M. Head-Gordon, J. Chem. Phys. **101**, 6593 (1994).

[32] C. A. White, B. G. Johnson, P. M. W. Gill, and M. Head-Gordon, Chem. Phys. Lett. **253**, 268 (1996).

[33] E. Schwegler and M. Challacombe, J. Chem. Phys. **105**, 2726 (1996).

[34] J. C. Burant, G. E. Scuseria, and M. J. Frisch, J. Chem. Phys. **105**, 8969 (1996).

[35] A. F. Izmaylov, E. N. Brothers, and G. E. Scuseria, J. Chem. Phys. **125**, 224105 (2006).

[36] X. Li, J. M. Millam, G. E. Scuseria, M. J. Frisch, and H. B. Schlegel, J. Chem. Phys. **119**, 7651 (2003).

[37] J. M. Millam and G. E. Scuseria, J. Chem. Phys. **106**, 5569 (1997).

[38] R. Car and M. Parrinello, Phys. Rev. Lett. **55**, 2471 (1985).

[39] H. B. Schlegel, J. M. Millam, S. S. Iyengar, G. A. Voth, A. D. Daniels, G. E. Scuseria, and M. J. Frisch, J. Chem. Phys. **114**, 9758 (2001).

[40] E. S. Kryachko, Int. J. Quantum Chem. **48**, 109 (1993).

[41] E. Kryachko, J. Phys.: Condens. Matter **5**, 4429 (1993).

[42] E. S. Kryachko, Phys. Rev. B **47**, 15935 (1993).

[43] D. Marx and J. Hutter, in *Modern Methods and Algorithms of Quantum Chemistry*, edited by J. Grotendorst (John von Neumann Institute for Computing, Julich, 2000), Vol. 1.

[44] C. M. Isborn and X. Li, J. Chem. Phys. **129**, 204107 (2008).

[45] B. Bagchi, Annu. Rev. Phys. Chem. **40**, 115 (1989).

[46] P. J. Rossky and J. D. Simon, Nature **370**, 263 (1994).

[47] J. M. Bofill, J. Comput. Chem. **15**, 1 (1994).

[48] O. Farkas and H. B. Schlegel, Phys. Chem. Chem. Phys. **4**, 11 (2002).

[49] X. Li and M. J. Frisch, J. Chem. Theory Comput. **2**, 835 (2006).

[50] L. N. Trefethen, D. Bau III, and G. Hulbert, Appl. Mech. Rev. **51**, B1 (1998).

[51] J. Wilson, E. B., J. C. Decius, and P. C. Corss, *Molecular Vibrations* (McGraw-Hill, New York, 1955).

[52] M. J. Frisch, G. W. Trucks, H. B. Schlegel, G. E. Scuseria, M. A. Robb, J. R. Cheeseman, G. Scalmani, V. Barone, B. Mennucci, G. A. Petersson, H. Nakatsuji, M. Caricato, X. Li, H. P. Hratchian, A. F. Izmaylov, J. Bloino, G. Zheng, J. L. Sonnenberg, W. Liang, M. Hada, M. Ehara, K. Toyota, R. Fukuda, J. Hasegawa, M. Ishida, T. Nakajima, Y. Honda, O. Kitao, H. Nakai, T. Vreven,

J. J. A. Montgomery, J. E. Peralta, F. Ogliaro, M. Bearpark, J. J. Heyd, E. Brothers, K. N. Kudin, V. N. Staroverov, T. Keith, R. Kobayashi, J. Normand, K. Raghavachari, A. Rendell, J. C. Burant, S. S. Iyengar, J. Tomasi, M. Cossi, N. Rega, J. M. Millam, M. Klene, J. E. Knox, J. B. Cross, V. Bakken, C. Adamo, J. Jaramillo, R. Gomperts, R. E. Stratmann, O. Yazyev, A. J. Austin, R. Cammi, C. Pomelli, J. W. Ochterski, R. L. Martin, K. Morokuma, V. G. Zakrzewski, G. A. Voth, P. Salvador, J. J. Dannenberg, S. Dapprich, P. V. Parandekar, N. J. Mayhall, A. D. Daniels, O. Farkas, J. B. Foresman, J. V. Ortiz, J. Cioslowski, and D. J. Fox, Gaussian Development Version H.12+, 2011, computer Program.

[53] C. L. Moss and X. Li, J. Chem. Phys. **129**, 114102 (2008).

[54] P. O. Löwdin, Adv. Quantum Chem. **5**, 185 (1970).

[55] G. H. Golub and C. F. van Loan, *Matrix Computations* (Johns Hopkins University Press, Baltimore, 1996).

[56] S. S. Iyengar, H. B. Schlegel, J. M. Millam, G. A. Voth, G. E. Scuseria, and M. J. Frisch, J. Chem. Phys. **115**, 10291 (2001).

[57] X. P. Li, W. Nunes, and D. Vanderbilt, Phys. Rev. B **47**, 10891 (1993).

[58] H. B. Schlegel, S. S. Iyengar, X. S. Li, J. M. Millam, G. A. Voth, G. E. Scuseria, and M. J. Frisch, J. Chem. Phys. **117**, 8694 (2002).

[59] S. S. Iyengar, J. Chem. Phys. **123**, 084310 (2005).

[60] S. S. Iyengar and M. J. Frisch, J. Chem. Phys. **121**, 5061 (2004).

[61] S. S. Iyengar, H. B. Schlegel, G. A. Voth, J. M. Millam, G. E. Scuseria, and M. J. Frisch, Isr. J. Chem. **42**, 191 (2002).

[62] R. McWeeny, Rev. Mod. Phys. **32**, 335 (1960).

[63] K. N. Kudin, G. E. Scuseria, and E. CancÃĺs, J. Chem. Phys. **116**, 8255 (2002).

[64] E. Badaeva, Y. Feng, D. R. Gamelin, and X. Li, New J. Phys. **10**, 055013 (2008).

[65] J. Heyd, G. E. Scuseria, and M. Ernzerhof, J. Chem. Phys. **118**, 8207 (2003).

[66] J. Heyd and G. E. Scuseria, J. Chem. Phys. **120**, 7274 (2004).

[67] J. Heyd and G. E. Scuseria, J. Chem. Phys. **121**, 1187 (2004).

[68] S. Rice and M. Zhao, *Optical control of molecular dynamics* (Wiley Interscience, ADDRESS, 2000).

[69] M. Shapiro and P. Brumer, *Principles of the Quantum Control of Molecular Processes* (Wiley Interscience, ADDRESS, 2003).

[70] S. Chelkowski and A. D. Bandrauk, J. Chem. Phys. **99**, 4279 (1993).

[71] A. Talebpour, A. D. Bandrauk, K. Vijayalakshmi, and S. L. Chin, Journal of Physics B-Atomic Molecular and Optical Physics **33**, 4615 (2000).

[72] M. Padgett and L. Allen, Phys. World **10**, 35 (1997).

[73] R. J. Levis, G. M. Menkir, and H. Rabitz, Science **292**, 709 (2001).

[74] C. J. Bardeen, V. V. Yakovlev, K. R. Wilson, S. D. Carpenter, P. M. Weber, and W. S. Warren, Chem. Phys. Lett. **280**, 151 (1997).

[75] X. Li, J. C. Tully, H. B. Schlegel, and M. J. Frisch, J. Chem. Phys. **123**, 084106 (2005).

[76] C. M. Isborn, X. Li, and J. C. Tully, J. Chem. Phys. **126**, 134307 (2007).

[77] T. Kinugawa, P. Lablanquie, F. Penent, J. Palaudoux, and J. H. D. Eland, J. Electron Spectrosc. Relat. Phenom. **141**, 143 (2004).

[78] A. Hishikawa, A. Matsuda, M. Fushitani, and E. J. Takahashi, Phys. Rev. Lett. **99**, (2007).

[79] T. Osipov, C. L. Cocke, M. H. Prior, A. Landers, T. Weber, O. Jagutzki, L. Schmidt, H. Schmidt-Bocking, and R. Dorner, Phys. Rev. Lett. **90**, 233002 (2003).

[80] J. A. Pople, M. J. Frisch, K. Raghavachari, and P. V. Schleyer, J. Comput. Chem. **3**, 468 (1982).

[81] D. Duflot, J. M. Robbe, and J. P. Flament, J. Chem. Phys. **102**, 355 (1995).

[82] R. Thissen, J. Delwiche, J. M. Robbe, D. Duflot, J. P. Flament, and J. H. D. Eland, J. Chem. Phys. **99**, 6590 (1993).

[83] H. B. Li, Xiaosong; Schlegel, J. Phys. Chem. A **108**, 468 (2004).

[84] P. Erman, A. Karawajczyk, E. Rachlew-Kaellne, and C. Stroemholm, J. Chem. Phys. **102**, 3064 (1995).

[85] T. B. Settersten, B. D. Patterson, and J. A. Gray, J. Chem. Phys. **124**, 234308 (2006).

[86] R. Polak and J. Fiser, Chem. Phys. **303**, 73 (2004).

[87] Z. P. Zhong, W. H. Zhang, and J.-M. Li, J. Chem. Phys. **113**, 136 (2000).

[88] Y. Hikosaka, T. Aoto, K. Ito, Y. Terasaka, R. Hirayama, and E. Miyoshi, J. Chem. Phys. **128**, 044320 (2008).

[89] L. Verlet, Phys. Rev. **159**, 98 (1967).

[90] X. S. Li, S. M. Smith, A. N. Markevitch, D. A. Romanov, R. J. Levis, and H. B. Schlegel, Phys. Chem. Chem. Phys. **7**, 233 (2005).

[91] W. L. Hase, in *Encyclopedia of Computational Chemistry*, edited by P. v. R. Schleyer, N. L. Allinger, T. Clark, J. Gasteiger, P. A. Kollman, H. F. Schaefer III, and P. R. Schreiner (Wiley, New York, 1998).

[92] M. E. Casida, in *Recent Developments and Applications of Modern Density Functional Theory, Theoretical and Computational Chemistry*, edited by J. M. Seminario (Elsevier, Amsterdam, 1996), Vol. 4.

[93] R. E. Stratmann, G. E. Scuseria, and M. J. Frisch, J. Chem. Phys. **109**, 8218 (1998).

[94] B. Friedrich and D. Herschbach, Phys. Rev. Lett. **74**, 4623 (1995).

[95] W. Kim and P. M. Felker, J. Chem. Phys. **104**, 1147 (1996).

[96] T. Seideman, J. Chem. Phys. **103**, 7887 (1995).

[97] H. Sakai, C. P. Safvan, J. J. Larsen, K. M. Hilligsoe, K. Hald, and H. Stapelfeldt, J. Chem. Phys. **110**, 10235 (1999).

[98] L. V. Keldysh, Soviet Physics JETP **20**, 1307 (1965).

[99] J. Neugebauer, E. J. Baerends, and M. Nooijen, J. Chem. Phys. **121**, 6155 (2004).

[100] N. T. Maitra, F. Zhang, R. J. Cave, and K. Burke, J. Chem. Phys. **120**, 5932 (2004).

[101] A. Dreuw and M. Head-Gordon, Chem. Rev. **105**, 4009 (2005).

[102] B. G. Levine, C. Ko, J. Quenneville, and T. J. Martinez, Mol. Phys. **104**, 1039 (2006).

[103] B. S. Hudson and B. E. Kohler, J. Chem. Phys. **59**, 4984 (1973).

[104] B. Hudson and B. Kohler, Annu. Rev. Phys. Chem. **25**, 437 (1974).

[105] K. Schulten, I. Ohmine, and M. Karplus, J. Chem. Phys. **64**, 4422 (1976).

[106] R. J. Cave and E. R. Davidson, J. Phys. Chem. **92**, 614 (1988).

[107] C.-P. Hsu, S. Hirata, and M. Head-Gordon, J. Phys. Chem. A **105**, 451 (2001).

[108] J. H. Starcke, M. Wormit, J. Schirmer, and A. Dreuw, Chem. Phys. **329**, 39 (2006).

[109] R. L. Christensen, M. G. I. Galinato, E. F. Chu, J. N. Howard, R. D. Broene, and H. A. Frank, J. Phys. Chem. A **112**, 12629 (2008).

[110] J. D. Watts, S. R. Gwaltney, and R. J. Bartlett, J. Chem. Phys. **105**, 6979 (1996).

[111] T. Polivka and V. Sundstroem, Chem. Rev. **104**, 2021 (2004).

[112] S. Tretiak and V. Chernyak, J. Chem. Phys. **119**, 8809 (2003).

[113] R. J. Cave, F. Zhang, N. T. Maitra, and K. Burke, Chem. Phys. Lett. **389**, 39 (2004).

[114] G. Mazur and R. Wlodarczyk, J. Comput. Chem. **30**, 811 (2009).

[115] H. Nakatsuji, Chem. Phys. Lett. **177**, 331 (1991).

[116] B. Saha, M. Ehara, and H. Nakatsuji, J. Chem. Phys. **125**, 014316 (2006).

[117] C. M. Isborn, S. V. Kilina, X. Li, and O. V. Prezhdo, J. Phys. Chem. C **112**, 18291 (2008).

[118] J. D. Simon, Acc. Chem. Res. **21**, 128 (1988).

[119] R. M. Stratt and M. Maroncelli, J. Phys. Chem. **100**, 12981 (1996).

[120] P. Bandyopadhyay and M. S. Gordon, J. Chem. Phys. **113**, 1104 (2000).

[121] Q. Cui, J. Chem. Phys. **117**, 4720 (2002).

[122] H. Li, C. S. Pomelli, and J. H. Jensen, Theor. Chem. Acc. **109**, 71 (2003).

[123] B. Mennucci, R. Cammi, and J. Tomasi, J. Chem. Phys. **109**, 2798 (1998).

[124] R. Cammi and B. Mennucci, J. Chem. Phys. **110**, 9877 (1999).

[125] R. Cammi, B. Mennucci, and J. Tomasi, J. Phys. Chem. A **104**, 5631 (2000).

[126] G. Scalmani, M. J. Frisch, B. Mennucci, J. Tomasi, R. Cammi, and V. Barone, J. Chem. Phys. **124**, 094107 (2006).

[127] P. G. Wolynes, J. Chem. Phys. **86**, 5133 (1987).

[128] M. D. Newton and H. L. Friedman, J. Chem. Phys. **88**, 4460 (1988).

[129] C. Hsu, X. Song, and R. A. Marcus, J. Phys. Chem. B **101**, 2546 (1997).

[130] M. V. Basilevsky, D. F. Parsons, and M. V. Vener, J. Chem. Phys. **108**, 1103 (1998).

[131] M. Orozco and F. J. Luque, Chem. Rev. (Washington, D. C.) **100**, 4187 (2000).

[132] J. Tomasi, B. Mennucci, and R. Cammi, Chem. Rev. (Washington, DC, U. S.) **105**, 2999 (2005).

[133] W. Liang, C. M. Isborn, and X. Li, J. Phys. Chem. A **113**, 3463 (2009).

[134] C. L. Moss, C. M. Isborn, and X. Li, Phys. Rev. A **80**, 024503 (2009).

[135] C. T. Chapman, W. Liang, and X. Li, J. Phys. Chem. Lett. **2**, 1189 (2011).

[136] W. Hackbusch, *Integral Equations: Theory and Numerical Treatment* (Birkhauser Verlag, Boston, 1995).

[137] E. Cances, B. Mennucci, and J. Tomasi, J. Chem. Phys. **107**, 3032 (1997).

[138] B. Mennucci, E. Cances, and J. Tomasi, J. Phys. Chem. B **101**, 10506 (1997).

[139] E. Cances and B. Mennucci, J. Math. Chem. **23**, 309 (1998).

[140] G. Scalmani and M. J. Frisch, J. Chem. Phys. **132**, 114110 (2010).

[141] F. Lipparini, G. Scalmani, B. Mennucci, E. Cances, M. Caricato, and M. J. Frisch, J. Chem. Phys. **133**, 014106 (2010).

[142] F. Lipparini, G. Scalmani, B. Mennucci, and M. J. Frisch, J. Chem. Theory Comput. **7**, 610 (2011).

[143] P. N. Butcher and D. Cotter, *The Elements of Nonlinear Optics* (Cambridge University Press, Cambridge; New York, 1990).

[144] A. Tsolakidis, D. Sanchez-Portal, and R. M. Martin, Phys. Rev. B: Condens. Matter Mater. Phys. **66**, 235416 (2002).

[145] B. F. Levine, Chem. Phys. Lett. **37**, 516 (1976).

[146] A. M. Moran and A. M. Kelley, J. Chem. Phys. **115**, 912 (2001).

[147] E. R. Davidson, B. E. Eichinger, and B. H. Robinson, Opt. Mater. **29**, 360 (2006).

[148] C. Lee, W. Yang, and R. D. Parr, Phys. Rev. B **37**, 785 (1988).

[149] A. Becke, J. Chem. Phys. **98**, 5648 (1993).

[150] S. Hirata, M. Head-Gordon, and R. J. Bartlett, J. Chem. Phys. **111**, 10774 (1999).

[151] R. Koeppe and N. Sariciftci, Photochem. Photobiol. Sci. **5**, 1122 (2006).

[152] C. Deibel and V. Dyakonov, Rep. Prog. Phys. **73**, (2010).

[153] N. C. Cates, R. Gysel, Z. Beiley, C. E. Miller, M. F. Toney, M. Heeney, I. McCulloch, and M. D. McGehee, Nano Lett. **9**, 4153 (2009).

[154] Y. Liang, Z. Xu, J. Xia, S.-T. Tsai, Y. Wu, G. Li, C. Ray, and L. Yu, Adv. Mater. (Weinheim, Ger.) **22**, E135 (2010).

[155] R. M. Williams, J. M. Zwier, and J. W. Verhoeven, J. Am. Chem. Soc. **117**, 4093 (1995).

[156] R. M. Williams, M. Koeberg, J. M. Lawson, Y.-Z. An, Y. Rubin, M. N. Paddon-Row, and J. W. Verhoeven, J. Org. Chem. **61**, 5055 (1996).

[157] S. Spallanzani, C. A. Rozzi, D. Varsano, T. Baruah, M. R. Pederson, F. Manghi, and A. Rubio, J. Phys. Chem. B **113**, (2009).

[158] T. Baruah and M. R. Pederson, J. Chem. Phys. **125**, (2006).

[159] T. Baruah and M. R. Pederson, J. Chem. Theory Comput. **5**, 834 (2009).

[160] M. E. Casida, *Time-dependent density functional response theory for molecules.* (World Scientific, ADDRESS, 1995), No. Recent Advances in Density Functional Methods, Pt. 1, pp. 155–192.

[161] S. Hirata and M. Head-Gordon, Chem. Phys. Lett. **302**, 375 (1999).

[162] P. Dirac, Math. Proc. Cambridge **26**, 376 (1930).

[163] P. Dirac, *The principles of quantum mechanics* (Clarendon Press, Oxford, 1947), Vol. 1, see in particular Chapter V31-32.

[164] A. Messiah, *Quantum Mechanics, Vol.1* (North-Holland, Amsterdam, 1961), see in particular Chapter VI.I.4 in Volume I.

[165] J. J. Sakurai and S. F. Tuan, *Modern quantum mechanics* (Benjamin/Cummings, Menlo Park, Calif., 1985), see in particular Chapter 2.4.

[166] F. Grossmann, Comments At. Mol. Phys. **34**, 141 (1999).

[167] F. Scheck, *Mechanics : from Newton's Laws to Deterministic Chaos* (Berlín, Alemania : Springer, New York, 1988), see in particular Chapter 2.35.

[168] P. Ehrenfest, Z. Phys. **45**, 455 (1927).

Appendix A

DERIVING CLASSICAL AND EHRENFEST MOLECULAR DYNAMICS

Most of this appendix follows closely from Ref [43].

Continuing the discussion in section 1.2 of the introductory chapter, as we insert the product ansatz in eq 1.7 into eq 1.6, and multiply from the left by $\langle\Psi_e|$ and $\langle\Psi_n|$ while imposing energy conservation $d\langle H\rangle/dt \equiv 0$, we can reach the following relations

$$i\hbar\frac{\partial\Psi_e}{\partial t} = -\sum_i \frac{\hbar^2}{2m_e}\nabla_i^2\Psi_e + \langle\Psi_n(\mathbf{R},t)|\,\hat{V}_{ee} + \hat{V}_{ne} + \hat{V}_{nn}\,|\Psi_n(\mathbf{R},t)\rangle\,\Psi_e \tag{A.1}$$

$$i\hbar\frac{\partial\Psi_n}{\partial t} = -\sum_I \frac{\hbar^2}{2M_I}\nabla_I^2\Psi_n + \langle\Psi_n(\mathbf{R},t)|\,\hat{H}_e\,|\Psi_n(\mathbf{R},t)\rangle\,\Psi_n \tag{A.2}$$

This set of coupled equations defines the basis of the time-dependent self-consistent field (TDSCF) method introduced as early as 1930 by Dirac.[162] Both electrons and nuclei move quantum-mechanically in time-dependent effective potentials obtained from appropriate expectation averages over the other class of freedom. Thus, the relations of eq A.1 and A.2 gives rise to a mean-field description of the coupled nuclear-electronic quantum dynamics, which is also the simplest possible separation of electronic and nuclear variables.

To derive the classical molecular dynamics, the next step is to approximate the nuclei as classical point particles. An effective scheme to extract classical mechanics from quantum mechanics starts with reinterpreting the QM nuclear wavefunction using an amplitude factor A and a phase S that both are real with $A > 0$, see

refs[163–165] for instance.

$$\Psi_n(\mathbf{R},t) = A(\mathbf{R},t)exp\left[\frac{i}{\hbar}S(\mathbf{R},t)\right] \tag{A.3}$$

Then transform the nuclear wavefunction in eq A.2 with the new variables and separate the real and imaginary parts, one can arrive the so-called "quantum fluid dynamical representation" of the TDSCF equation for the nuclei.

$$i\hbar\frac{\partial\Psi_n}{\partial t} = -\sum_I \frac{\hbar^2}{2M_I}\nabla_I^2\Psi_n + \langle\Psi_e(\mathbf{R},t)|\,\hat{H}_e\,|\Psi_e(\mathbf{R},t)\rangle\,\Psi_n \tag{A.4}$$

$$i\hbar\frac{\partial\Psi_e}{\partial t} = -\sum_i \frac{\hbar^2}{2m_e}\nabla_i^2\Psi_e + \langle\Psi_n(\mathbf{R},t)|\,\hat{V}_{ee}+\hat{V}_{ne}+\hat{V}_{nn}\,|\Psi_n(\mathbf{R},t)\rangle\,\Psi_e \tag{A.5}$$

Note that equations A.4 and A.5 can also be applied to solve the time-dependent Schrödinger equation. The relation for A, eq A.4, can be further expressed as a continuity equation[163–165] using the nuclear density $|\Psi_n|^2 \equiv A^2$ from the new definition eq A.3. In this continuity equation, $\hbar$ vanishes and the particle probability $|\chi|^2$ associated to the nuclei in the presence of a flux is locally conserved.

On the other hand, the relation for S (eq A.5) provides more useful information for the present purpose. The term on the right hand side of this equation depends on $\hbar$, and it is solely negligible considering the classical limit as $\hbar \to 0$,

$$\frac{\partial S}{\partial t} + \sum_I \frac{1}{2M_I}(\nabla_I S)^2 + \langle\Psi_e|\,\hat{H}_e\,|\Psi_e\rangle = 0 \tag{A.6}$$

Expansion on $\hbar$ in eq A.5 can lead to a hierarchy of semiclassical methods.[164, 166] The resulting equation shares the similar form to equations of motion in the Hamilton-Jacobi formulation[167] of classic mechanics

$$\frac{\partial S}{\partial t} + \mathcal{H}(\{\mathbf{R}_I\},\{\nabla_I S\}) = 0 \tag{A.7}$$

with the classical Hamilton function

$$\mathcal{H}(\{\mathbf{R}_I\},\{\mathbf{P}_I\}) = T(\{\mathbf{P}_I\}) + V(\{\mathbf{R}_I\}) \tag{A.8}$$

where $\mathcal{H}$ is defined in terms of generalized coordinates $\mathbf{R}_I$ and their conjugate momenta $\mathbf{P}_I$. With the connecting transformation $\mathbf{P}_I \equiv \nabla_I S$, the Newtonian equation of motion corresponding to eq A.6 becomes

$$\frac{d\mathbf{P}_I}{dt} = -\nabla_I V_e^E(\{\mathbf{R}_I(t)\}) \quad or$$
$$M_I \ddot{\mathbf{R}}_I = -\nabla_I \langle \Psi_e | \hat{H}_e | \Psi_e \rangle \tag{A.9}$$

Thereby, the nuclei motion is determined by classical mechanics that all of them move in an effective potential V_e^E given by the electrons. Such potential depends only on the nuclear positions at time t and the averaging H_e over the electronic degrees of freedom, i.e. the quantum expectation value $\langle \Psi | \hat{H}_e | \Psi \rangle$, with nuclear positions fixed at their instantaneous values. Such classical interpretation also leads to a time-dependent electronic wave equation

$$i\hbar \frac{\partial \Psi_e}{\partial t} = \langle \Psi_e(\mathbf{R}, t) | \hat{H}_e | \Psi_e(\mathbf{R}, t) \rangle \tag{A.10}$$

which evolves self-consistently as the classical nuclei are propagated following eq A.9.

In time-dependent molecular system modeling, solving eq A.9 together with eq A.10 is often referred as the "Ehrenfest molecular dynamics" approach, in honor of Ehrenfest who was the first to relate Newtonian classical dynamics to Schrödinger's wave equation.[168] In a brief sense, this hybrid or mixed approach force the nuclei to behave like classical particles, while treat the electrons as quantum objects.

Although being a mean-field theory, the TDSCF approach underlying Ehrenfest molecular dynamics rigorously includes all transitions between different electronic states, so it is capable of capturing the nonadiabatic effect. This can be seen by expanding the electronic wavefunction Ψ_e in terms of many electronic states or determinants ψ_k with complex coefficients $\{c_k(t)\}$

$$\Psi_e(\mathbf{r}, \mathbf{R}; t) = \sum_{k=0}^{\infty} c_k(t) \psi_k(\mathbf{r}, \mathbf{R}) \tag{A.11}$$

The squre norm of the coefficients $\{|c_k(t)|^2\}$ thus shows explicitly the time evolution of the populations (occupations) of the different states $\{k\}$ whereas interferences are included through the $\{c_k^* c_{l\neq k}\}$ contributions. One good choice for the basis ψ_k is the adiabatic state obtained from solving the time-independent electronic Schrödinger equation

$$\hat{H}_e(\mathbf{r}, \mathbf{R})\psi_k = E_k(\mathbf{R})\psi_k(\mathbf{r}, \mathbf{R}) \tag{A.12}$$

where $\mathbf{R}$ are the instantaneous nuclear positions at time t according to eq A.9.